

AD-A251 636



92-14515



MASSACHUSETTS INSTITUTE OF TECHNOLOGY
Laboratory for Advanced Solid State Laser Materials
Center for Materials Science and Engineering
Cambridge, Massachusetts 02139

CHROMIUM IONS IN TETRAHEDRAL SITES

by

VEI-HAN CHAN



Accession For	
NTIS 68441	<input checked="" type="checkbox"/>
DTIC 148	<input type="checkbox"/>
Unclassified	<input type="checkbox"/>
Justification	
By	
Distribution/	
Availability Codes	
Dist	Avail and/or Special
A-1	

Technical Report No. 2

September 1991

- * The research covered by this Report was sponsored by the Office of Naval Research under Grant#N00014-90-J-4073. The views and conclusions in this document are those of the authors and should not be interpreted as necessarily representing the official policies, either expressed or implied, of the Office of Naval Research or the U. S. Government. There are no limitations as to the distribution of the information contained in this Report.

CHROMIUM IONS IN TETRAHEDRAL SITES

by

VEI-HAN CHAN

Submitted to the Department of
Electrical Engineering and Computer Science
on May 24, 1991 in Partial Fulfillment of the Requirements
for the Degree of Master of Science in
Electrical Engineering

ABSTRACT

Chromium doped åkermanite crystals were investigated by optical spectroscopy and electron paramagnetic resonance spectroscopy. The results were compared to chromium doped forsterite to study the roles of tetrahedrally coordinated chromium ions in the near-infrared laser transition.

Åkermanite crystals were successfully grown by Czochralski methods. The growth processes and characteristics of various furnaces were explored to yield good optical quality crystals.

The energy levels of chromium ions in tetrahedral sites can be explained by crystal field theory. The ground state energy level splitting under an external magnetic field is well described by spin-hamiltonian matrices.

From electron paramagnetic resonance measurements of the chromium doped åkermanite and forsterite crystals and the similarity of their optical absorption spectra, tetravalent chromium ions were believed to occupy tetrahedral sites in all the samples. However, there exist considerable differences in zero-phonon line transitions and emission spectra. Therefore, it has not been completely proved that the mechanism responsible for near-infrared laser transition in chromium doped forsterite is solely due to chromium ions in tetrahedral sites.

Thesis Supervisor: Dr. Hans P. Jenssen

Title: Principal Research Associate and Lecturer, Dept. of EECS

ABOUT THE AUTHOR

Vei-Han Chan was born on 28th of November, 1964 in Taipei, Taiwan, Republic of China. He earned his Bachelor of Science degree from the Department of Electrical Engineering at National Taiwan University in 1986. After graduation, he joined the ROC Navy for two years. During that period, he served as an ensign in Chinese Naval Weapon School in Kaohsiung, Taiwan to work on ship-based fire control systems. Before coming to M.I.T., he studied at Univ. of California, Los Angeles for one year.

His research interest is in solid-state applications, especially on optics and electronics. Right now, he is a Ph.D. candidate in Department of Electrical Engineering and Computer Science at M.I.T..

He has received numerous dean's list of distinguished students awards and received several scholarships including Chiang Kai-Shek Memorial Scholarships, Sampo Electric Inc. Scholarships, etc. in his undergraduate study. He is a member of Chinese Institute of Engineers.

ACKNOWLEDGEMENTS

I would like to express my thanks to Dr. Hans P. Jenssen, my advisor, who made this work possible and helped me during different stages of this work.

Also, I am indebted to Dr. Mark Garrett who helped me construct the furnaces and grow the crystals used in this study. Thanks go also to Gary Allen for his kind help in building the furnaces.

I am also grateful to David Knowles who showed me how to perform optical spectroscopy and discussed various problems which I encountered during this work.

I also would like to thank Dr. David Gabbe and Peter Kloumann for their useful opinions about various aspects of crystal growth.

The author appreciate the efforts of reviewing the manuscript by Ken Dinndorf and Dr. Arlete Cassanho.

Finally, thanks my wife Caroline's constant support and encouragement during my study in M.I.T..

TABLE OF CONTENTS

List of Figures, Tables	7
Chapter One: Introduction	11
1.1 Motivation	11
1.2 Identification of the Chromium Centers	13
1.3 Crystal Growth Facility	14
1.4 Contents and Organization of the Thesis	15
References	16
Chapter Two: Crystal Preparation	18
2.1 Crystal Structure	18
2.1.1 Forsterite (Mg_2SiO_4)	18
2.1.2 Åkermanite ($\text{Ca}_2\text{MgSi}_2\text{O}_7$ and $\text{Ba}_2\text{MgGe}_2\text{O}_7$)	20
2.2 Crystal Growth	24
2.2.1 Introduction	24
2.2.2 Crystal Growth by a RF Induction Heated Furnace	28
2.2.3 Crystal Growth by a Two-Zone Resistance Heated Furnace	32
2.2.4 Crystal Growth by a Single Zone Resistance Heated Furnace	37
2.2.5 Conclusion	40
References	41
Chapter Three: Theory of Chromium Ions in Tetrahedral Sites	43
3.1 Environment Consideration	43
3.2 d^2 and d^3 in Cubic Environments	49
3.3 Spin-Orbit Interaction and Low Symmetry Fields	52
3.3.1 Energy Level Splitting of Ground State	53
References	59

Chapter Four: Spectroscopy and Analysis	60
4.1 Experiment Procedure	60
4.1.1 Optical Spectroscopy	60
4.1.2 Electron Paramagnetic Resonance Spectroscopy	62
4.2 Results and Analysis of Optical Spectroscopy	63
4.2.1 Cr:Forsterite	63
4.2.2 Cr:Ca ₂ MgSi ₂ O ₇	73
4.2.3 Cr:Ba ₂ MgGe ₂ O ₇	77
4.2.4 Comparison	81
4.3 Results and Analysis of EPR Spectroscopy	84
4.3.1 Cr:Åkermanite(Ba ₂ MgGe ₂ O ₇)	84
4.3.2 Cr:Forsterite	88
4.3.3 Comparison	88
References	90
Chapter Five: Final Discussions	92
5.1 Summary	92
5.2 Survey of d ² Configuration in Tetrahedral Sites	93
5.3 Future Research	95
References	96
Appendix: Matrix Elements and Eigenenergies of d ² and d ³ Configurations	98

List of Figures, Tables

Fig. 2.1	Unit cell of forsterite, Mg_2SiO_4 .	19
Fig. 2.2	Åkermanite structure projected on (001) plane showing the location of $\text{A}_2\text{BC}_2\text{O}_7$.	21
Fig. 2.3	Åkermanite structure along c axis.	21
Fig. 2.4	Interatomic distances and site symmetry of the silicon site in Mg_2SiO_4 and $\text{Ca}_2\text{MgSi}_2\text{O}_7$.	23
Fig. 2.5	Phase diagram of system $\text{CaO}\cdot\text{SiO}_2$ - $2\text{CaO}\cdot\text{MgO}\cdot 2\text{SiO}_2$.	25
Fig. 2.6	Photo of Czochralski-grown $\text{Cr}:\text{Ca}_2\text{MgSi}_2\text{O}_7$ and $\text{Cr}:\text{Ba}_2\text{MgGe}_2\text{O}_7$ and $\text{Cr}:\text{Mg}_2\text{SiO}_4$ used in this study.	28
Fig. 2.7	Schematic of the rf induction heated Czochralski furnace.	29
Fig. 2.8	Temperature profile of the rf furnace.	31
Fig. 2.9	Power control loop of the rf furnace.	31
Fig. 2.10	Measured power and temperature fluctuation in the temperature control mode.	33
Fig. 2.11	Measured power and temperature fluctuation in the power control mode.	33

Fig. 2.12	Schematic of the two-zone resistance heated furnace.	34
Fig. 2.13	Photo of undoped $\text{Ca}_2\text{MgSi}_2\text{O}_7$ grown from a platinum wire.	36
Fig. 2.14	Temperature profile along furnace axis without a crucible.	36
Fig. 2.15	Temperature profile along furnace axis with a crucible.	37
Fig. 2.16	Schematic of the single-zone resistance heated furnace.	38
Fig. 2.17	Photo of crystal grown by using air blowing and crystal dipping techniques.	39
Fig. 3.1	Symmetry operations of tetrahedral sites.	46
Fig. 3.2	Energy level diagram for a d^2 ions in a tetrahedral field.	51
Fig. 3.3	${}^3A_1/{}^3A_2$ level splitting as a function of H.	58
Fig. 4.1	Experimental set-up for emission measurements.	61
Fig. 4.2	Experimental set-up for life-time measurements.	61
Fig. 4.3	Room temperature absorption spectra of $\text{Cr:Mg}_2\text{SiO}_4$.	64

Fig. 4.4	Symmetry descending and associated selection rules.	65
Fig. 4.5	(a) Calculated and predicted energy levels of Cr^{4+} ions in forsterite. (b) Tanabe-Sugano diagram for Cr^{4+} in a tetrahedral coordination with $C=4.4B$.	67
Fig. 4.6	10 K absorption spectrum of $\text{Cr:Mg}_2\text{SiO}_4$ for $E//b$.	69
Fig. 4.7	Room temperature polarized emission spectra of $\text{Cr:Mg}_2\text{SiO}_4$.	70
Fig. 4.8	$\text{Cr:Mg}_2\text{SiO}_4$ room temperature fluorescence decay at 1200nm.	71
Fig. 4.9	Near infrared $E//b$ absorption and emission of Cr:forsterite at liquid helium temperature.	72
Fig. 4.10	Room temperature polarized absorption spectra of $\text{Cr:Ca}_2\text{MgSi}_2\text{O}_7$.	74
Fig. 4.11	10K polarized absorption spectra of $\text{Cr:Ca}_2\text{MgSi}_2\text{O}_7$.	75
Fig. 4.12	Calculated and observed energy levels of Cr^{4+} ions in $\text{Ca}_2\text{MgSi}_2\text{O}_7$.	76
Fig. 4.13	Room temperature polarized absorption spectra of $\text{Cr:Ba}_2\text{MgGe}_2\text{O}_7$.	78
Fig. 4.14	10K polarized absorption spectra of $\text{Cr:Ba}_2\text{MgGe}_2\text{O}_7$.	79

Fig. 4.15	Calculated and observed energy levels of Cr^{4+} ions in $\text{Ba}_2\text{MgGe}_2\text{O}_7$.	81
Fig. 4.16	(a) Configuration-coordinate diagram showing the zero-phonon line transition. (b) Configuration-coordinate diagram for non-radiative processes.	85
Fig. 4.17	$\text{Ba}_2\text{MgGe}_2\text{O}_7$ $\text{P}\bar{4}2_1\text{m}$ space group symmetry.	85
Fig. 4.18	Angular dependence of resonant EPR field in Cr-doped $\text{Ba}_2\text{MgGe}_2\text{O}_7$.	87
Fig. 4.19	Angular dependence of resonant EPR field in Cr-doped forsterite.	89
Table 2.1	Crystallographic data of forsterite.	19
Table 2.2	Crystallographic data of $\text{Ca}_2\text{MgSi}_2\text{O}_7$.	22
Table 2.3	Some properties of åkermanite and forsterite.	22
Table 2.4	Interatomic distances of silicon tetrahedra.	23
Table 3.1	Character table for T_d symmetry and the corresponding $\ell=2$ full rotation state.	46
Table 4.1	Absorption peaks of three Cr-doped crystals.	82

Chapter 1

Introduction

1.1 Motivation

Trivalent chromium ions are the most widely used dopant for tunable laser crystals such as the chromium(Cr) doped alexandrite laser.¹ A chromium activated crystal, forsterite ($\text{Cr}^{3+}:\text{Mg}_2\text{SiO}_4$), was recently reported to lase at 1250nm.² Rager and Weiser³ assigned the main feature of the absorption spectra in forsterite to Cr^{3+} ions in octahedral sites. Cr^{3+} ions have been found by electron paramagnetic resonance methods to substitute for the two nonequivalent magnesium octahedral sites-the inversion site and the mirror site.⁴

After energy level calculations were performed, it was found that chromium ions in octahedral sites do not have the near-infrared absorption 1-1.2 μm which was observed in $\text{Cr}:\text{Mg}_2\text{SiO}_4$. Additionally, the large absorption bands observed in the visible frequency regions do not resemble the known absorption bands of Cr^{3+} in other octahedral environments. Therefore, it is unlikely that Cr^{3+} ions in octahedral sites are the lasing centers in $\text{Cr}:\text{forsterite}$. Although other impurity centers such as Fe^{3+} , Fe^{2+} and Cr^{2+} or lattice defects such as Mg^{2+} vacancies have been considered to be the lasing centers, they have been ruled out by Verdun.⁵

It was noted that the near-infrared absorption strength scales with the chromium concentration and growth atmospheres. This scaling indicates that chromium is responsible for the laser transition; however, it is most likely some valence states other than Cr^{3+} . According to studies by Petricevic⁶ and Verdun⁷, crystals grown under oxygen atmospheres have absorption characteristics which can be explained by Cr^{4+} substituting for silicon's tetrahedral sites in forsterite. Time-resolved spectroscopy indicated the existence of three different kinds of emitting centers; which can be attributed to Cr^{3+} and Cr^{4+} .⁸ All experimental evidence points to the conclusion that Cr^{4+} ion in tetrahedral site is the lasing center.

A similar situation can be found for chromium doped garnet crystals with the general formula $\text{A}_3\text{B}_2\text{C}_3\text{O}_{12}$ which has several substitution sites for chromium. The trivalent ion A^{3+} is in the dodecahedral site with coordination eight, while B^{3+} is in the octahedral site with coordination six, and C^{4+} is in the tetrahedral site with coordination four. Garnet crystals activated with rare earth ions such as Nd^{3+} doped $\text{Y}_3\text{Al}_5\text{O}_{12}$ (YAG) are important solid state laser materials. The absorption spectra of rare earth ions resembles atomic spectra, with many narrow lines which absorb little flash-lamp pumping energy. In order to increase the efficiency of the Nd^{3+} laser pumping, chromium ions, with their broad absorption bands, are co-doped into garnets. Chromium normally enters the garnets as Cr^{3+} in the octahedral B site with an absorption bands from 600 to 800nm. But it was noted that there is also an additional absorption band around 1-1.5 μm which could not be attributed to Cr^{3+} . This absorption, which overlaps the lasing range of Nd^{3+} , reduces the Nd^{3+} laser's performance. This absorption was initially attributed to other impurity centers, but was finally attributed to Cr^{4+} in the C site by several authors.^{9,10} As a matter of fact, this impurity center has already emerged as a lasing center of its own.¹¹

Due to the presence of Cr in several valence states as well as other possible types of charge compensation centers in the crystals, there will be overlapping absorption bands from different sites. This coupled with the complex structures of garnet crystals and forsterite, makes it very difficult to directly identify the impurity center responsible for the near infrared absorption and emission. Although the center has been assumed to be Cr^{4+} in tetrahedral sites in both garnets and forsterite, there has been no clear and direct evidence of Cr^{4+} ions in tetrahedral sites.

The purpose of this study was to establish the existence of chromium ions in tetrahedral sites and to characterize these centers.

1.2 Identification of the Chromium Centers

As stated in the last section, the presence of octahedral sites facilitates the existence of Cr^{3+} ions in forsterite. This will complicate the identification processes. In order to isolate the effects solely due to Cr^{4+} in tetrahedral sites, another kind of crystal, åkermanite ($\text{Ca}_2\text{MgSi}_2\text{O}_7$), was used. Åkermanite is a naturally formed mineral, as is forsterite. However, it is different from forsterite in that there are no octahedral sites in åkermanite. The chromium dopant can only enter into tetrahedral sites. This characteristic makes åkermanite an excellent choice to study the properties of chromium ions in tetrahedral sites.

Even with åkermanite, optical methods are not sufficient to identify the impurity center due to the broad absorption bands of the chromium ions. Therefore electron paramagnetic resonance (also called electron spin resonance) measurements are used to assist identification of the center. Electron paramagnetic resonance(EPR) can directly measure the ground state splitting of the dopant ions, which can yield information about the site

symmetry and the valence state of the ion. Based on the data from åkermanite, chromium doped forsterite can be analyzed more easily and the centers can be readily identified by the same methods.

1.3 Crystal Growth Facility

In order to grow $\text{Ca}_2\text{MgSi}_2\text{O}_7$, a radio frequency(rf) induction heated furnace was constructed. The alternating current(AC) supplied by the power supply produces a time-varying magnetic field which in turn induces an AC current in the platinum crucible wall. According to Ohm's law, the crucible will be heated up.

Owing to the direct coupling between the crucible and the rf coil, the furnace has a large temperature gradient and is suitable for the Czochralski growth method. Before growing $\text{Ca}_2\text{MgSi}_2\text{O}_7$, its isomorphous germanate, $\text{Ba}_2\text{MgGe}_2\text{O}_7$, was grown due to its lower growth temperature and melt viscosity. $\text{Ba}_2\text{MgGe}_2\text{O}_7$ was first grown in our lab back in the 1960's, but at that time it was used as a laser host for rare earth ions.¹²

After $\text{Ba}_2\text{MgGe}_2\text{O}_7$ was successfully grown, $\text{Ca}_2\text{MgSi}_2\text{O}_7$ was also grown. Due to some difficulties in the growth of $\text{Ca}_2\text{MgSi}_2\text{O}_7$ in the rf induction heated furnace, both a single and a two-zone resistance heated furnaces were also used to grow $\text{Ca}_2\text{MgSi}_2\text{O}_7$. These furnaces are different from the rf furnace in that they are heated up by thermal convective flow. These furnaces have a more uniform temperature distribution which is not suitable for Czochralski growth; however, temperature gradients can be obtained by adjusting the temperature of the upper/lower zones in two-zone furnace or by using an air-cooled seed rod in the single-zone furnace.

1.4 Contents and Organization of the Thesis

Chapter two will describe the crystal structure of both forsterite and åkermanite. Their structural similarities and differences will be clarified. Crystal growth processes will also be explained and the results will be analyzed. In this study, three kinds of furnaces- the radio frequency induction heated, the single-zone resistance heated, and the two-zone resistance heated furnaces were used. Their characteristics are explored and compared.

Chapter three establishes the theory of energy levels for chromium ions in tetrahedral sites. It is mainly based on crystal field theory which treats lattices as a classical distribution of point charges. The spin-hamiltonian matrices are used to explain the energy level splitting of the ground state, which is essential to interpret the electron paramagnetic resonance spectra. The spin-orbit interaction, which is less important for transition metal ions, is also generally described.

Chapter four lists the results of the optical spectroscopy and electron paramagnetic resonance spectroscopy. Absorption and emission spectra at both room temperature and liquid helium temperature are presented. The spectra can be explained by Tanabe-Sugano diagram. Also the EPR field for resonance spectra are shown and can be explained by spin-hamiltonian matrices and the space group symmetry of crystals.

Chapter five summarizes the works in this study and the comparisons of different d^2 configurations in different host materials. Finally, possible future study is suggested.

References

- 1 J. C. Walling, O. G. Peterson, H. P. Jenssen, R. C. Morris and E. W. O'Dell, "Tunable Alexandrite Lasers," IEEE J. Quantum Electron., QE-16, p1302, 1980.
- 2 V. Petricevic, S. K. Gayen and R. R. Alfano, "Laser Action in Chromium-activated Forsterite for Near-infrared Excitation: Is Cr^{4+} the lasing ions?," Appl. Phys. Lett., V53(26), p2590, 1988.
- 3 H. Rager and G. Weiser, "Polarized Absorption Spectra of Trivalent Chromium in Forsterite, Mg_2SiO_4 ," Bull. Mineral, V104, p603, 1981.
- 4 H. Rager, "Electron Spin Resonance of Trivalent Chromium in Forsterite Mg_2SiO_4 ," Phys. and Chem. Minerals, V1, p371, 1977.
- 5 H. R. Verdun, L. M. Thomas, D. M. Andrauskas and T. McCollum, "Chromium-doped Forsterite Laser Pumped with $1.06\mu\text{m}$ Radiation," Appl. Phys. Lett., V53(26), p2593, 1988.
- 6 V. Petricevic, S. K. Gayen and R. R. Alfano, "Chromium-activated Forsterite Laser," OSA Proceedings on Tunable Solid State Laser Conference, V5, p77, 1989.
- 7 H. R. Verdun, L. M. Thomas, D. M. Andrauskas and A. Pinto, "Laser Performance of Chromium-Aluminum-Doped Forsterite," OSA Proceedings on Tunable Solid State Laser Conference, V5, p85, 1989.
- 8 R. Moncorge, D.J. Simkin, G. Cormier and J.A. Capobianco, "Spectroscopic Properties and Fluorescence Dynamics in Chromium Doped Forsterite," OSA Proceedings on Tunable Solid State Laser Conference, V5, p93, 1989.
- 9 L. I. Krutova, N. A. Kulagin, V. A. Sandulenko, and A. V. Sandulenko, "Electronic State and Positions of Chromium Ions in Garnet Crystals," Sov. Phys. Solid State, 31(7), p1193, 1989.

- 10 N. A. Kulagin and V. A. Sandulenko, "Ab Initio Theory of Electronic Spectra of Doped Crystals: Chromium Ions in Oxides," Sov. Phys Solid State, 31(1), p133, 1989.
- 11 S. Kuch, K. Petermann, G. Huber, "Spectroscopic Investigation of the Cr^{4+} Center in YAG," Technical Digest of Advanced Solid State Laser Conference, MA4, p11, 1991.
- 12 M. Alam, K. H. Goen, B. D. Barlolo, A. Linz, E. Sharp, L. Gillespie and G. Jannery, "Optical Spectra and Laser Action of Neodymium in a Crystal $\text{Ba}_2\text{MgGe}_2\text{O}_7$," J. Appl. Phys., V39, p4728, 1968.

Chapter 2

Crystal Preparation

2.1 Crystal Structure

2.1.1 Forsterite (Mg_2SiO_4)

Forsterite belongs to the olivine group with orthorhombic symmetry Pbnm. The unit cell contains four formula units. The unit cell's dimensions are $a=4.7534\text{\AA}$, $b=10.1902\text{\AA}$ and $c=5.9783\text{\AA}$.¹ The structure contains individual $[\text{SiO}_4]^{-4}$ tetrahedra linked by magnesium(Mg) atoms with coordination six. The same structure with different divalent atoms linking the individual tetrahedra constitute a series of compounds (e.g. fayalite(Fe_2SiO_4), tephroite(Mn_2SiO_4)) which are important rock forming minerals of the earth.

The divalent Mg atoms occupy two nonequivalent octahedral sites in forsterite. Half of the Mg atoms are located at the inversion octahedral site with symmetry C_i , the other half at the mirror octahedral sites with symmetry C_s . Its structure projected on (100) plane is shown in Fig. 2.1. The crystallographic data are listed in Table 2.1.

As it can be seen from Table 2.1, the silicon tetrahedron is distorted such that it has only mirror symmetry.

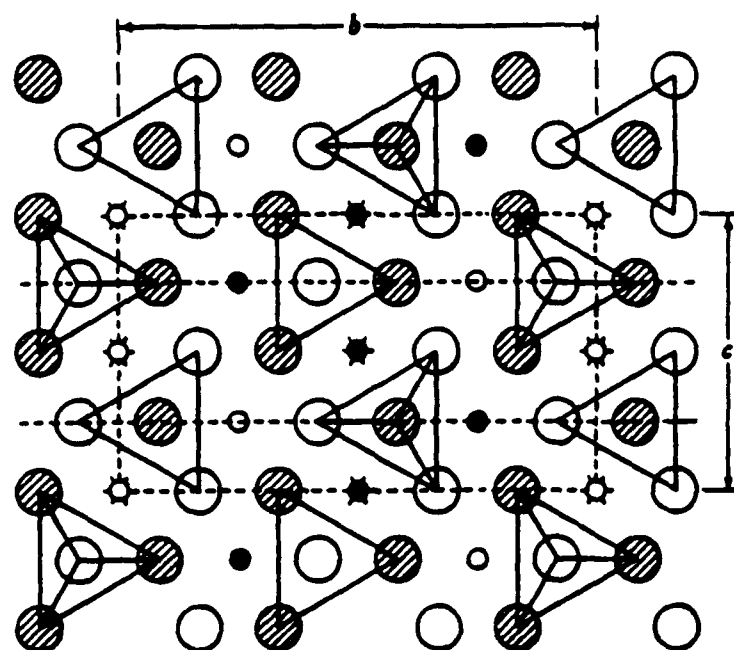


Fig. 2.1 Unit cell of forsterite, Mg_2SiO_4 . Small open and solid circles are Mg atoms, big circles are O atoms and silicon atoms (not shown) are at the centers of the tetrahedra. (After Ref. 2)

Table 2.1 Crystallographic data of forsterite. (After Ref.1)

$Z=4$, Symmetry $\text{Pbnm}(\#62)$

Ion	Site	Symm	Charge	x	y	z
Mg₁	4a	C_i	+2	0	0	0
Mg₂	4c	C_s	+2	0.99169	0.27739	0.25
Si	4c	C_s	+4	0.42645	0.09403	0.25
O₁	4c	C_s	-2	0.76549	0.09156	0.25
O₂	4c	C_s	-2	0.22164	0.44705	0.25
O₃	8d	C_1	-2	0.27751	0.16310	0.03304

The Cr:forsterite crystals used in this study were provided by Dr. R. Morris of Allied Signal Corporation. These crystals were doped with a sufficient amount of chromium to distinctly color the crystals olive green. When looking through the crystal's principal axes, it shows greenish, bluish and reddish color indicating strong dichroic effect.

2.1.2 Åkermanite ($\text{Ca}_2\text{MgSi}_2\text{O}_7$ and $\text{Ba}_2\text{MgGe}_2\text{O}_7$)^{3,4}

Åkermanite has the general formula $\text{A}_2\text{BC}_2\text{O}_7$ and belongs to the melilite group with tetragonal symmetry $P\bar{4}2_1m$. The A^{2+} ions have eight fold coordination, forming a distorted polyhedra with two different A-O distance. The B^{2+} ions occupy two tetrahedral sites (T1) located at the corners. C^{4+} ions occupy two adjacent equivalent tetrahedral sites (T2 and T3) to form $[\text{C}_2\text{O}_7]^{6-}$ double pyramid group. So the crystal structure consists of $[\text{BO}_4]^{6-}$ and $[\text{C}_2\text{O}_7]^{6-}$ parallel to the [001] direction linked by A-O bonds as shown in Fig. 2.2. The structure along the c axis is shown in Fig. 2.3.

All the tetrahedral sites are somewhat distorted, however. The individual symmetries and positions for Åkermanite ($\text{Ca}_2\text{MgSi}_2\text{O}_7$) are listed in Table 2.2.⁷ All the atoms are arranged in the unit cell according to the crystal symmetry $P\bar{4}2_1m$. Transition metal ions are suitable to substitute for the smaller B^{2+} or C^{4+} ions. The C^{4+} sites which we are interested in occupy the 4e sites in the notation of International Tables for X-ray Crystallography. Although the $[\text{CO}_4]^{-4}$ tetrahedra are distorted with symmetry C_s , the arrangements of the 4e sites make them optically equivalent in the a-a plane. But we can distinguish different contributions of these four tetrahedra in EPR spectroscopy by applying an external magnetic field.

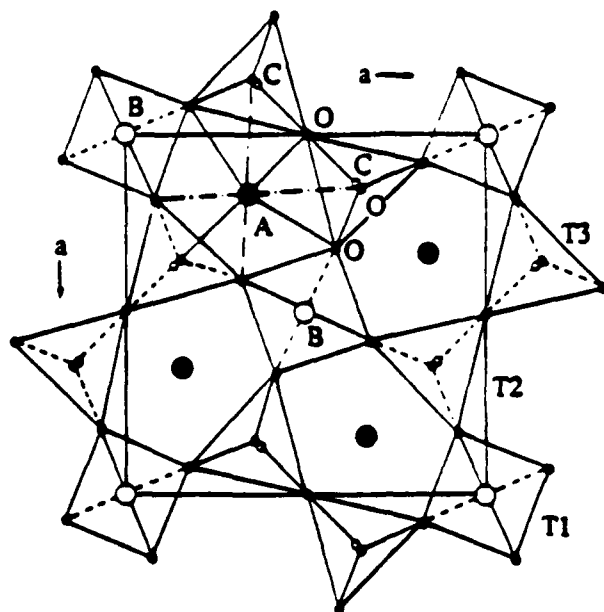


Fig. 2.2 Åkermanite structure projected on (001) plane showing the location of $A_2BC_2O_7$. (After Ref. 5)

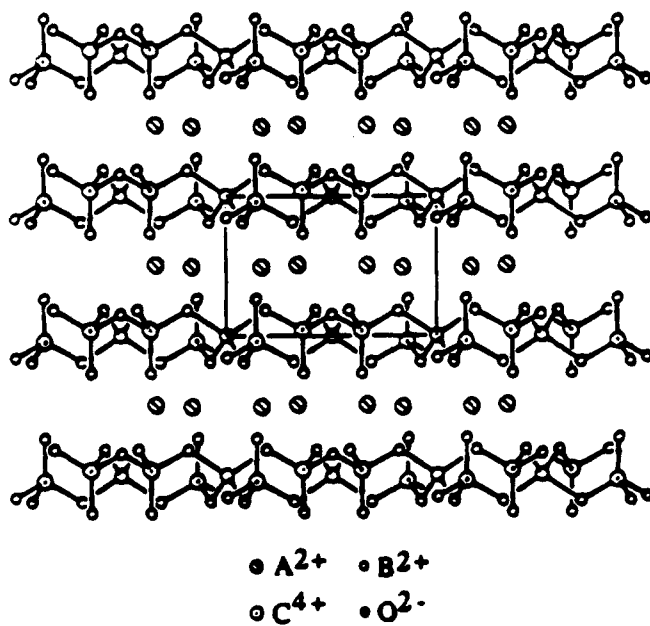


Fig. 2.3 Åkermanite structure along c axis. (After Ref. 6)

Table 2.2 Crystallographic data of $\text{Ca}_2\text{MgSi}_2\text{O}_7$. (After Ref. 7)

$Z=2$, Symmetry $P\bar{4}2_1m(\#113)$

Ion	Site	Symm	Charge	x	y	z
Ca	4e	C_3	+2	0.3355	0.5-x	0.5073
Mg	2a	S_4	+2	0	0	0
Si	4e	C_3	+4	0.1396	0.5-x	0.9412
O ₁	8f	C_1	-2	0.5	0.5-x	0.1804
O ₂	4e	C_3	-2	0.145	0.5-x	0.2583
O ₃	2c	C_{2v}	-2	0.082	0.182	0.7909

Åkermanite- $\text{Ca}_2\text{MgSi}_2\text{O}_7$ and its isomorphous germanate $\text{Ba}_2\text{MgSi}_2\text{O}_7$ were grown in this study. The tetrahedral coordinations of magnesium are unusual, since magnesium in most cases is found in coordination six such as in the case of forsterite.

Some physical properties of $\text{Ca}_2\text{MgSi}_2\text{O}_7$ and $\text{Ba}_2\text{MgGe}_2\text{O}_7$ along with forsterite are listed in Table 2.3.

Table 2.3 Some properties of Åkermanite($\text{Ca}_2\text{MgSi}_2\text{O}_7$ and $\text{Ba}_2\text{MgGe}_2\text{O}_7$) and forsterite.^{1,2,4,8,9}

composition	unit cell	refractive index	m.p.
	c/a/b(Å)	n(c)/n(a)/n(b)	
Mg_2SiO_4	5.978/4.753/10.19	1.670/1.635/1.651	1890°C
$\text{Ca}_2\text{MgSi}_2\text{O}_7$	5.010/7.843	1.640/1.632	1454°C
$\text{Ba}_2\text{MgGe}_2\text{O}_7$	5.56/8.36	1.834/1.843	~1403°C

The local symmetry and size of the silicon sites of forsterite and $\text{Ca}_2\text{MgSi}_2\text{O}_7$ are similar. The germanium site in $\text{Ba}_2\text{MgGe}_2\text{O}_7$ is

a little larger. The interatomic distances and site symmetries of these two compounds are shown in Fig. 2.4 and listed in Table 2.4.

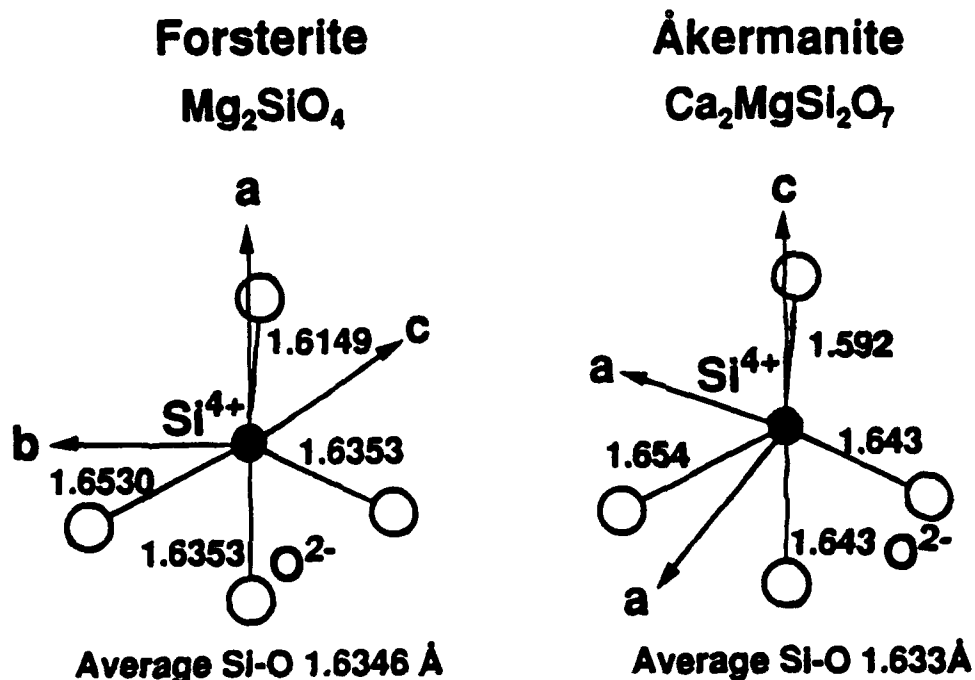


Fig. 2.4 Interatomic distances and site symmetry of the silicon site in Mg₂SiO₄ and Ca₂MgSi₂O₇.

Table 2.4 Interatomic distances of silicon tetrahedra.^{7,10}

Mg ₂ SiO ₄		Ca ₂ MgSi ₂ O ₇	
Si-O ₁	1.6149 Å	Si-O ₁	1.654 Å
Si-O ₂	1.6530 Å	Si-O ₂	1.592 Å
Si-O ₃	1.6353 Å (twice)	Si-O ₃	1.643 Å (twice)
O ₁ -O ₂	2.7434 Å	O ₁ -O ₂	2.720 Å
O ₁ -O ₃	2.7571 Å	O ₁ -O ₃	2.562 Å
O ₂ -O ₃	2.5527 Å	O ₂ -O ₃	2.749 Å
O ₃ -O' ₃	2.5941 Å	O ₃ -O' ₃	2.600 Å

Despite its similarity with forsterite, the distinctive feature of åkermanite is its lack of octahedral sites. This makes it an

excellent material to study the effect of tetrahedral coordination on chromium ions. Additionally, it is apparent that a chromium ion located in the nearly equivalent average Si-O interatomic separations (1.6346Å of forsterite vs 1.633Å of $\text{Ca}_2\text{MgSi}_2\text{O}_7$) should lead to nearly equivalent crystal-field strengths and thus transition energies.

2.2 Crystal Growth

2.2.1 Introduction

The phase relations of the CaO-MgO-SiO_2 ternary system have been intensively studied because numerous compounds are derived from this system (e.g. forsterite(Mg_2SiO_4), diopside($\text{CaMgSi}_2\text{O}_6$), merwinite($\text{Ca}_3\text{MgSi}_2\text{O}_8$) and etc.). According to the phase diagram shown in Fig. 2.5, $\text{Ca}_2\text{MgSi}_2\text{O}_7$ is congruently melting, so that it can be grown from a charge of stoichiometric composition. This makes it a good candidate for Czochralski growth. Its corresponding germanate ($\text{Ba}_2\text{MgGe}_2\text{O}_7$) was first grown in this laboratory in the 1960's by Czochralski growth method.⁸ This crystal also congruently melts at around 1403°C.

Compared to $\text{Ba}_2\text{MgGe}_2\text{O}_7$, $\text{Ca}_2\text{MgSi}_2\text{O}_7$ is more difficult to grow due to its higher melting point; in addition, molten silicates have high viscosity and tend to solidify as glass. In considering these reasons, I first tried to grow $\text{Ba}_2\text{MgGe}_2\text{O}_7$, then $\text{Ca}_2\text{MgSi}_2\text{O}_7$.

300 gram charges of powdered BaCO_3 (Baker Analyzed Reagent grade), MgO (Johnson Matthey Chemical) and GeO_2 (Eagle-Picher Industrial) were mixed together according to their molar proportion 2:1:2. 4% extra germanium oxide was added in order to compensate for its evaporation during the growth process. Chromium doping was provided by adding Cr_2O_3 to the charge.

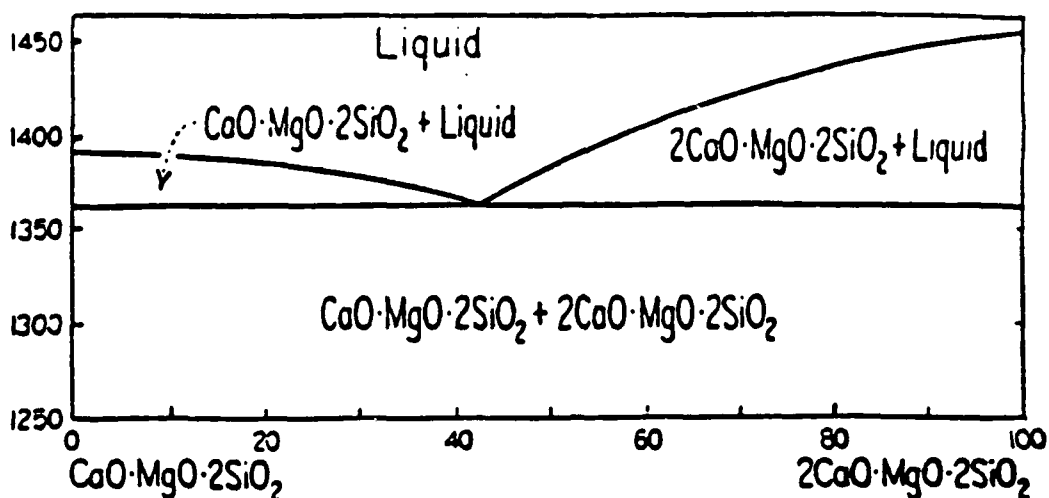


Fig. 2.5 Phase diagram of system $\text{CaO} \cdot \text{SiO}_2 - 2\text{CaO} \cdot \text{MgO} \cdot 2\text{SiO}_2$. (After Ref. 11)

Feed materials were pre-heated at 200°C for 24 hours to eliminate the water adsorbed by these materials. Materials were loaded and melted into a 250ml platinum crucible repeatedly until the whole 300 gram charge could fit in. The pre-melting sequence was

20°C	->	365°C	3 hrs
365°C	->	965°C	12 hrs
965°C	->	1000°C	1 hrs
1000°C	->	1200°C	20 hrs
1200°C	->	1420°C	11 hrs
1420° C	->	20°C	10 hrs

Since BaCO_3 reacts violently to release CO_2 in the temperature range of 1000°C to 1200°C, the step must be very slow in this range.

Both a induction furnace and a resistance furnace were used to grow $\text{Ba}_2\text{MgGe}_2\text{O}_7$. The characteristics of different furnaces will be discussed in the following sections.

The basic routine for a Czochralski growth run is¹²

- (1) raise the temperature a few degrees higher than the melting temperature.
- (2) rotate the seed rod with attached seed at a speed of 15-60 rpm and bring slowly into contact with melt. Then adjust the temperature such that neither growth or melting of the seed occur.
- (3) after 3-5 mins, start the pulling process at a typical rate 1-3 mm/hrs.
- (4) slowly lower temperature to achieve a desired diameter.
- (5) keep adjusting the power or temperature to maintain a constant diameter.

Using the above processes, undoped and 0.01, 0.1 and 0.5 mole percent chromium (with respect to Ge) doped $\text{Ba}_2\text{MgGe}_2\text{O}_7$ crystal were successfully grown with diameter 1.5cm and length 2-3 cm. The samples were confirmed to be single crystals by observing the birefringence of the crystals under polarizers. The crystal show an aqua-blue color and have a weak dichroic effect. The growth direction was [001]. The crystal grown by using the resistance heated furnace shows (100) and (110) facet planes. On the other hand, crystal grown by the rf induction heated furnace has no facets, which is probably due to the larger radial gradient in the rf furnace. After X-ray orientation, the boules were cut along the c and a axes to obtain samples for optical measurements. To facilitate crystal rotation for EPR experiments, crystals were

cut into right triangular prisms along the two a-axes and the c crystal axis.

After growth, the crucible can be cleaned by boiling in HCl.

The feed materials for $\text{Ca}_2\text{MgSi}_2\text{O}_7$ are CaCO_3 , MgO and SiO_2 . They are mixed also according to the molar proportion 2:1:2. The steps of preparation of $\text{Ca}_2\text{MgSi}_2\text{O}_7$ samples are very similar to the steps of $\text{Ba}_2\text{MgGe}_2\text{O}_7$ except minor modifications below:

- (1) No violent chemical action when CaCO_3 releases CO_2 , so the 100-1200°C heating step can be quicker.
- (2) No seed was available at the beginning of growth for $\text{Ca}_2\text{MgSi}_2\text{O}_7$. Seeds were obtained from material nucleated on a platinum wire. This process can be done by quickly immersing the wire in the melt; otherwise, instead of nucleation, the melt will supercool even down to 1390°C.
- (3) Since silicates do not react with HCl, the best way to clean the crucible is to dump material out of the crucible by heating the upside down crucible to the melting point of the residue.

By using this standard procedure, undoped and doped 0.1 and 0.25 mole percent chromium (respective to silicon) $\text{Ca}_2\text{MgSi}_2\text{O}_7$ were successfully grown by either a two-zone or a single zone resistance heated furnaces. $\text{Cr}:\text{Ca}_2\text{MgSi}_2\text{O}_7$ crystal shows deep blue color and has strong dichroic effect. There is a strong (001) cleavage plane which makes seed preparation along [001] direction difficult. So most of growth runs were performed along either [100] or [110] direction. The resulting crystals shows strong (100), (110) and (001) facet planes and are very unsymmetrical.

All the crystals were grown in ambient atmosphere in order to oxidize Cr^{3+} to Cr^{4+} . Typical pulling rates range from 0.5 to 2mm/hrs and the rotation rate between 15-60rpm.

The resulting crystals used in this study are shown in Fig. 2.6.

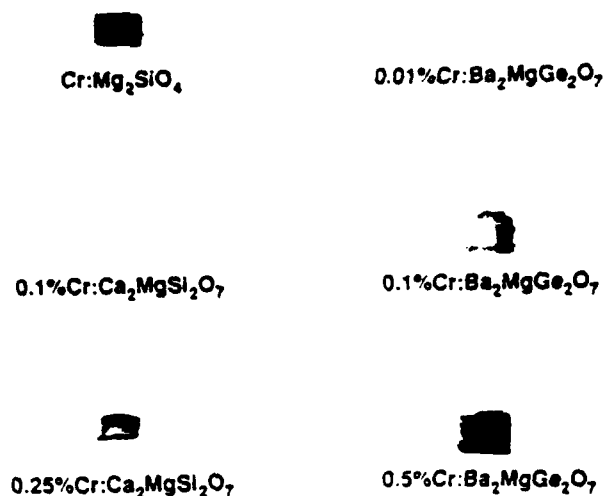


Fig. 2.6 Photo of Czochralski-grown $\text{Cr:Ca}_2\text{MgSi}_2\text{O}_7$, $\text{Cr:Ba}_2\text{MgGe}_2\text{O}_7$ and $\text{Cr:Mg}_2\text{SiO}_4$ used in this study.

2.2.2 Crystal Growth by a RF Induction Heated Furnace

The entire system includes a Pillar Mark-6 10KHz 30KW rf power supply, a Neslab System II heat exchanger for cooling, a PC-AT compatible computer with appropriate peripherals for control of power/temperature, pulling and rotation speed. The furnace is shown in Fig. 2.7.

A. Melt
 B. Seed and Crystal
 C. Platinum Crucible
 D. Alumina Crucible
 E. Alumina Muffle
 F. Alumina Cap

G. RF Coil
 H. Thermocouple
 I. Viewing Window
 J. Zircar Insulation
 K. Alumina Cup

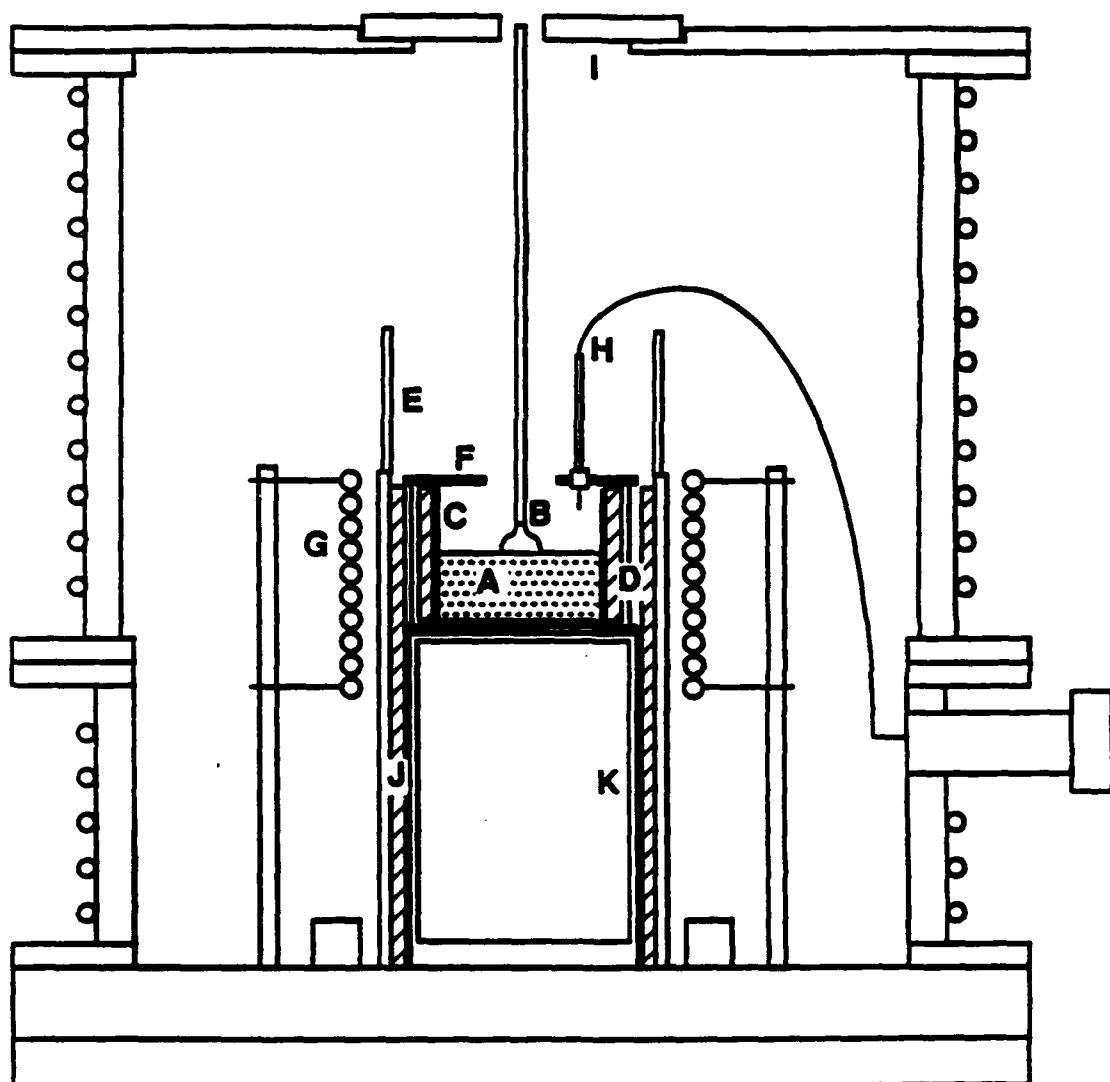


Fig. 2.7 Schematic of the rf induction heated Czochralski furnace.

The typical axial thermal profile of this rf furnace is shown in Fig. 2.8. There existed a large thermal gradient of about 25°C/cm above the melt surface. The radial gradient was also large. Initially, feedback control was performed through readings of a thermocouple near the melt surface; however large temperature variations of 4-5°C during the crystal growth run were observed. This was due to thermally driven convective flow inside the furnace, which was readily seen from the viewing window. These fluctuations were fed back to the controller which in turn tried to correct temperature (by correcting the power); which caused more oscillations in the temperature. Instead of temperature control, a power control loop was used while an optical pyrometer was used to measure the melt temperature.

The power control loop is shown in Fig. 2.9.¹³ Power can be set by the power count (ranging from 0 to 4095). Via a digital/analog converter and an optical isolator, the power count (PC) is converted to current to drive the power supply. Output voltage of a power measuring bulb (which is directly proportional to the output power) is read and digitized for the computer. This measurement is used to correct the power count to get the a constant power output.

The algorithm for correcting the power count is shown as followed.

$$(PC)_{next} = (PC)_{last} * (1 + P_g * (1 - power_{measured} / power_{setpoint})) \quad (2.1)$$

The parameter P_g (power gain) was chosen with respect to the measurement response time and the given sampling interval. The sampling interval is 1 sec in this system. Although this is not a linear control system, it works like a PI controller with steady state error equal to zero. After several tries, $P_g = 0.2-0.3$ gave satisfactory results with power regulation to within 0.1%. The

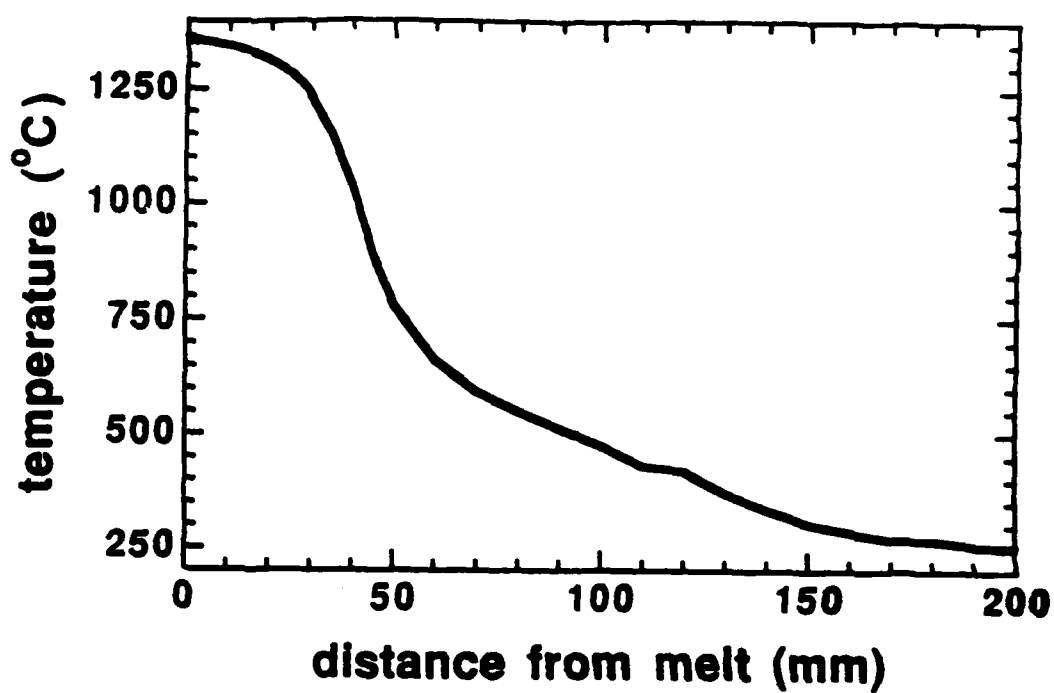


Fig. 2.8 Temperature profile of the rf furnace.

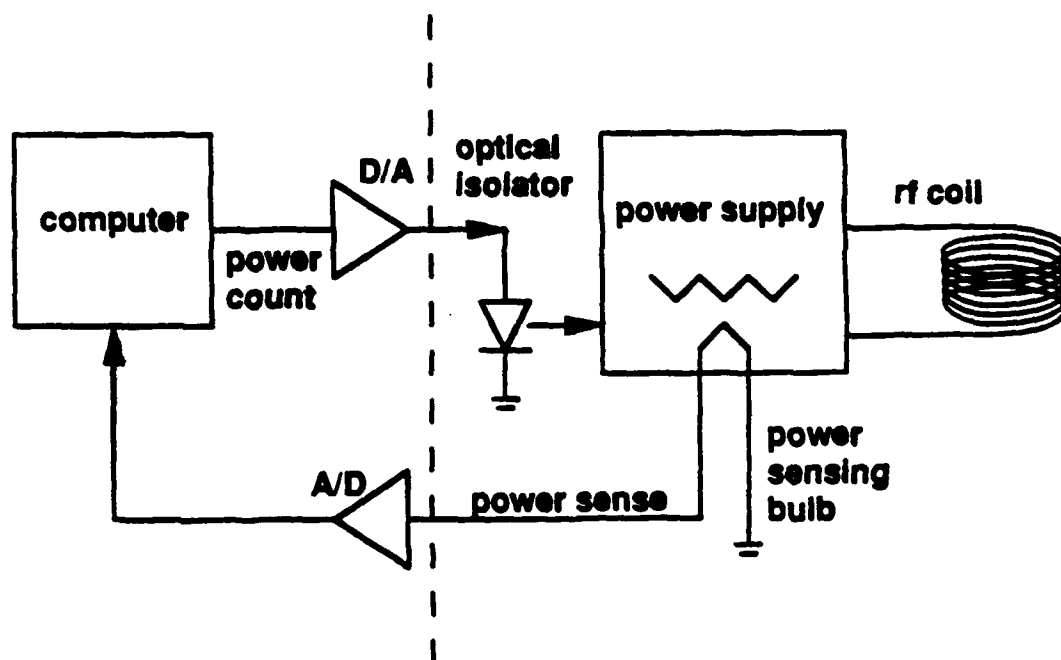


Fig. 2.9 Power control loop of the rf furnace.

temperature reading on top of the melt continued to fluctuate about 2-3 degrees. The fluctuation is believed to result from the thermally driven air flow. Fig. 2.10 and Fig. 2.11 show the corresponding power and temperature fluctuations for the temperature control and the power control mode. The advantage of using power control rather than temperature control can easily be seen.

By using the control methods described above, several 0.01%Cr:Ba₂MgGe₂O₇ crystal boules were pulled. During growth, it was observed that it was very difficult to manually control the diameter of the crystal. When expansion of the crystal diameter was visually noticed during the temperature cooling and pulling was started, the crystal emerging from the melt already had a large diameter. It appears that the crystal had started growing inside the melt. Additionally, most crystals grown showed ring shaped bubble inclusions along the boules in the regions between the center and the edge. This behavior can be explained by a non-flat growth interface. It is well known that a proper balance of forced convection (due to seed rod rotation) and natural convection (due to temperature gradient of the melt) are crucial to produce the desired growth interface, and good optical quality crystals. Further work on the flow pattern of the melt needs to be done to achieve good crystal quality.

2.2.3 Crystal Growth by a Two-Zone Resistance Heated Furnace

Due to the difficulty of controlling a rf furnace with the previous setup, a resistance heated furnace seemed to be an attractive alternative. Thus, a two-zone furnace shown in Fig. 2.12 was used to grow undoped and chromium doped Ca₂MgSi₂O₇. The control system is very similar to that of the rf furnace; except that the control thermocouple is located at the center of the lower

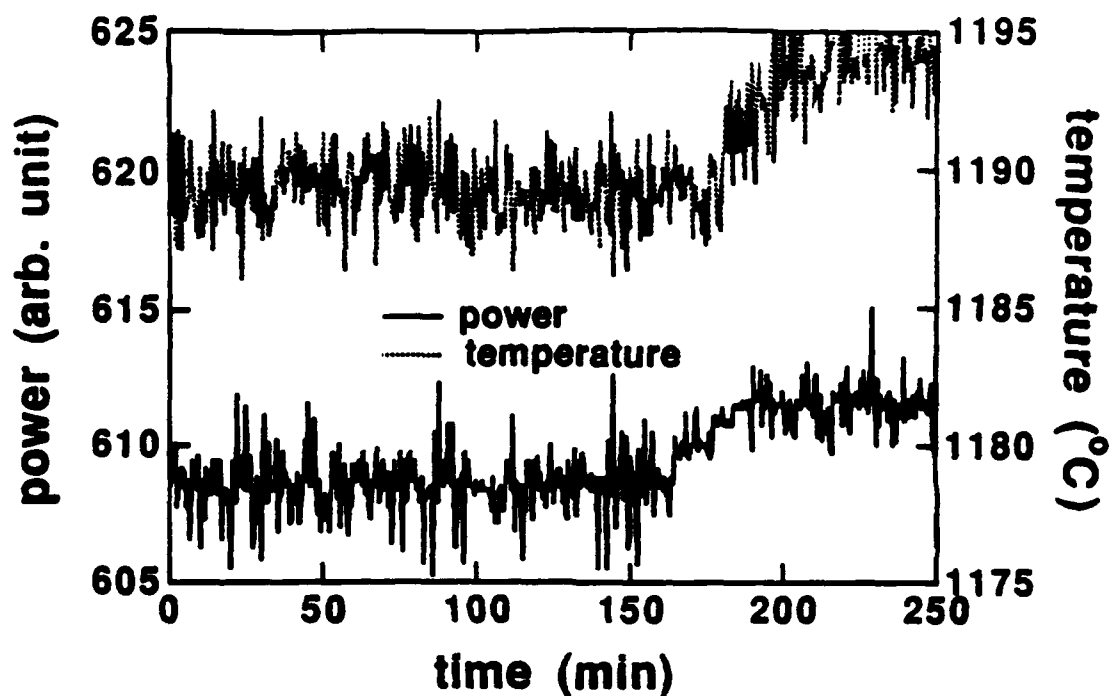


Fig. 2.10 Measured power and temperature fluctuation in the temperature control mode.

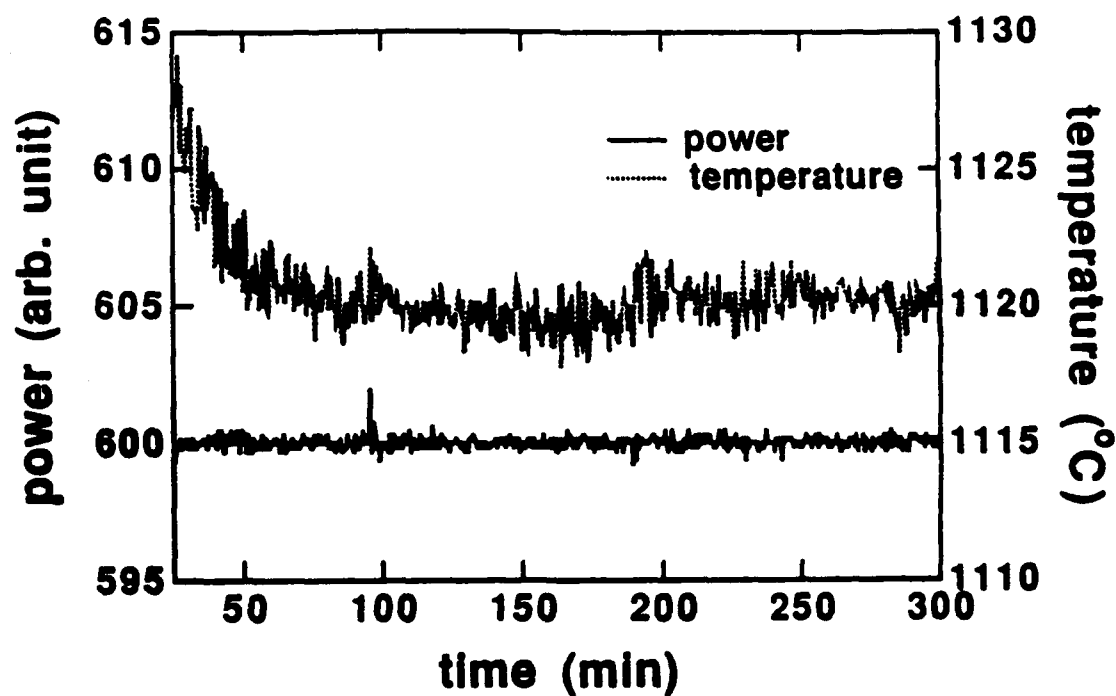


Fig. 2.11 Measured power and temperature fluctuation in the power control mode.

- A. Melt
- B. Seed Holder and Seed
- C. Platinum Crucible
- D. Alumina Crucible
- E. Alumina Liner
- F. Alumina Seed Rod
- G. Quartz View Port
- H. Kanthal Muffle Upper Heating Zone
- I. Kanthal Muffle Lower Heating Zone
- J. Double Wall Stainless Steel Enclosure
- K. Thermocouples

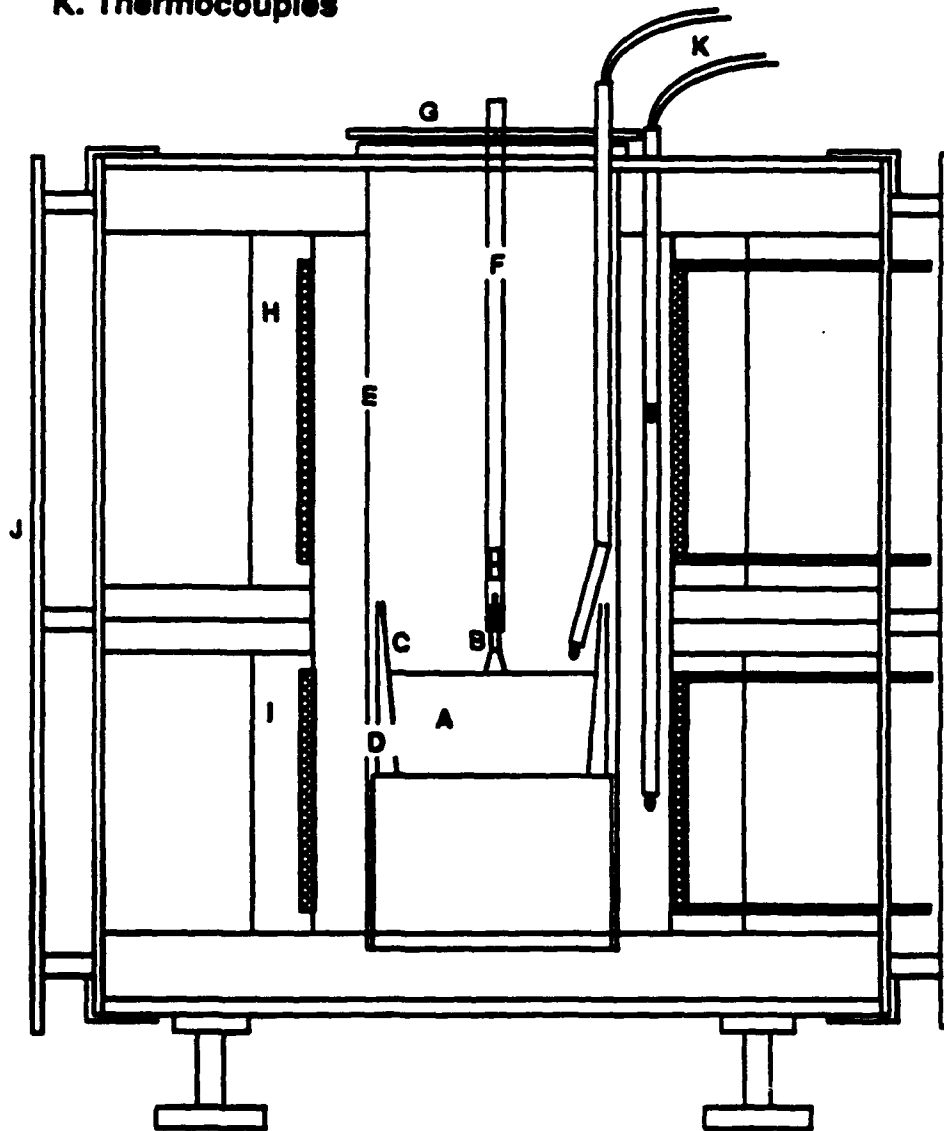


Fig. 2.12 Schematic of the two-zone resistance heated furnace.

heating element. The thermal gradient can be set by adjusting the relative power input to the upper and lower heating elements.

By controlling the temperature of the lower heater thermocouple(LHT), a temperature variation of $\pm 0.01^{\circ}\text{C}$ can be obtained. The same 0.01°C variation was observed on both the upper heater thermocouple and a thermocouple located above the melt; which illustrates the more steady thermal environment in this kind of furnace.

By using the technique described in section 2.2.1, undoped seed material (shown in Fig. 2.13) was nucleated on a platinum wire. Several similar foot-shaped crystals were pulled later. But generally speaking, the growth was not very successful. These crystals either grew rampantly or melted all the way, showing that the temperature near the growth interface was either too high or too low. This unusual behavior puzzled me for quite a while. Originally, I thought that seed was reacting with the alumina(Al_2O_3) seed rod. But when I put a platinum button between the seed and the seed rod, the same phenomenon occurred. Therefore, this is not the case. A detailed axial temperature measurement was performed by setting $\text{LHT}=1596^{\circ}\text{C}$ both with and without a crucible to determine possible causes. The results are shown in Fig. 2.14 and Fig. 2.15. Although the temperature measurement contained a lot of noise, it can give us a general trend of the temperature variations along the axis.

When the crucible was not in the furnace, the temperature decreased monotonously from the bottom to the top. However, when the crucible was put in, there existed an inverted temperature gradient in the first 1cm above the melt surface. Also in the latter case, the furnace needed less power input to achieve the same LHT temperature. The facts stated above show that with the crucible in place, the outside wall of the crucible can reflect heat back to the heating elements and somehow heat

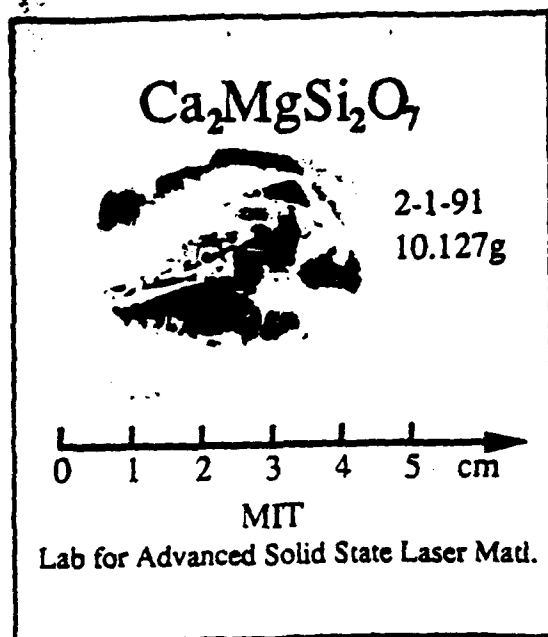


Fig. 2.13 Photo of undoped $\text{Ca}_2\text{MgSi}_2\text{O}_7$ grown from a platinum wire.

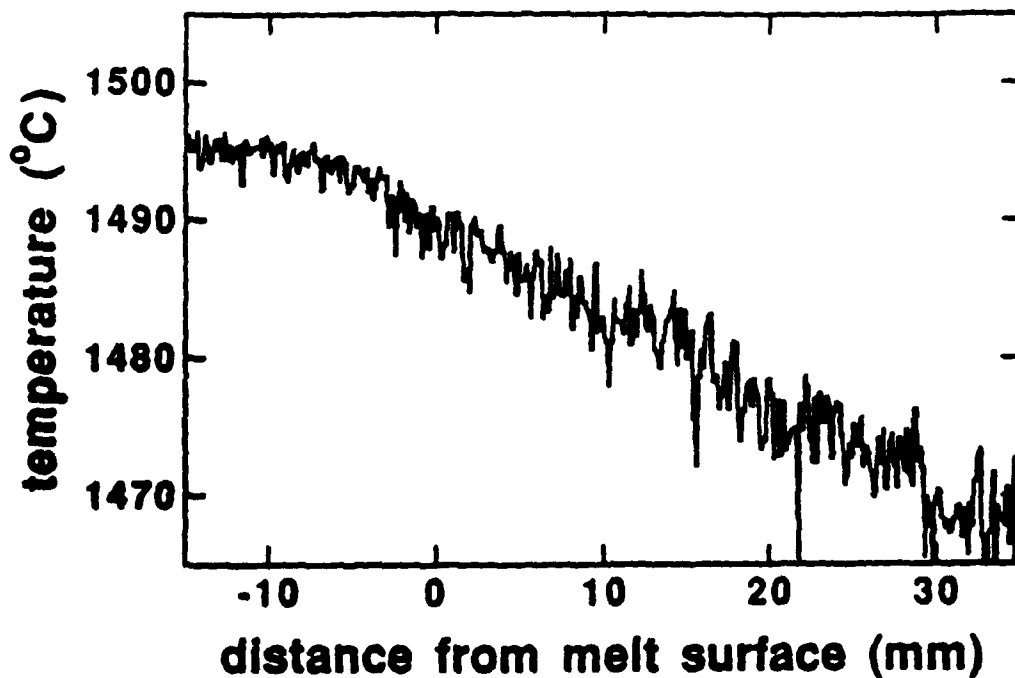


Fig. 2.14 Temperature profile along furnace axis without a crucible.

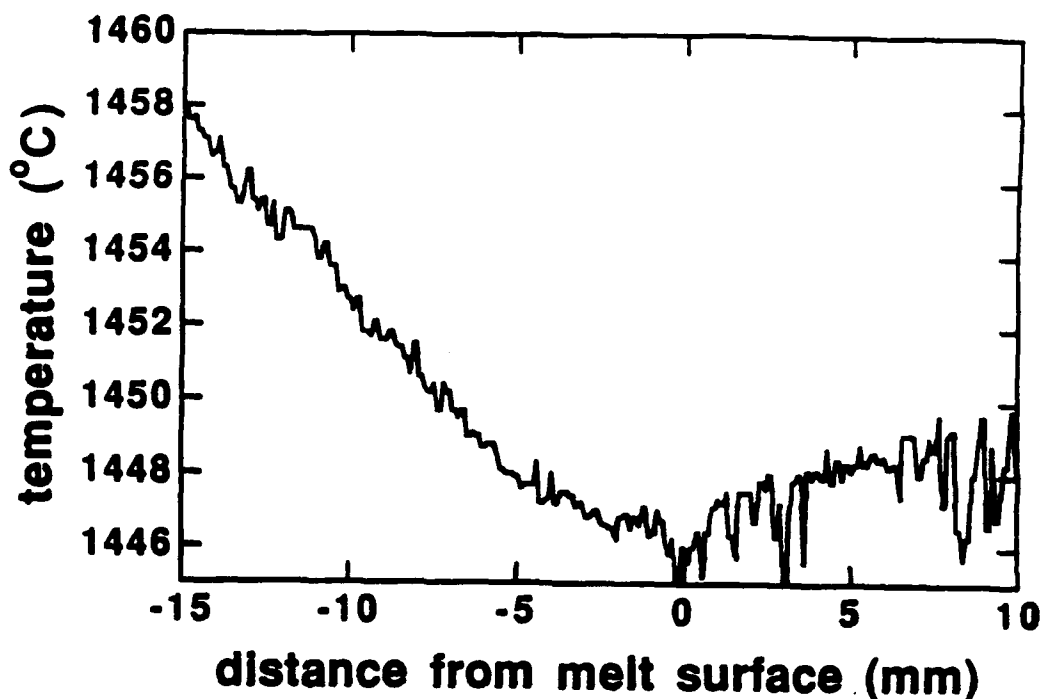


Fig. 2.15 Temperature profile along furnace axis with a crucible.

can transfer from the seed rod to the seed. Under these conditions, a good seeding temperature was obviously difficult to achieve.

2.2.4 Crystal Growth by a Single-Zone Resistance Heated Furnace

A single zone resistance heated furnace (shown in Fig. 2.16) contrary to that of a rf induction heated furnace has a rather uniform temperature distribution inside the furnace. In fact, due to the heat conduction path through the bottom, temperature decreased from the melt surface to the bottom of the crucible. A small inverted temperature gradient also existed above the melt surface, most likely for the same reason as in the two-zone furnace.

- A. Melt
- B. Seed Holder and Seed
- C. Platinum Crucible
- D. Alumina Crucible
- E. Alumina Muffle
- F. View Port
- G. Furnace Insulation Plug
- H. Alumina Seed Rod
- I. Molydisilicide Heating Element
- J. Zircar Insulation
- K. Thermocouple

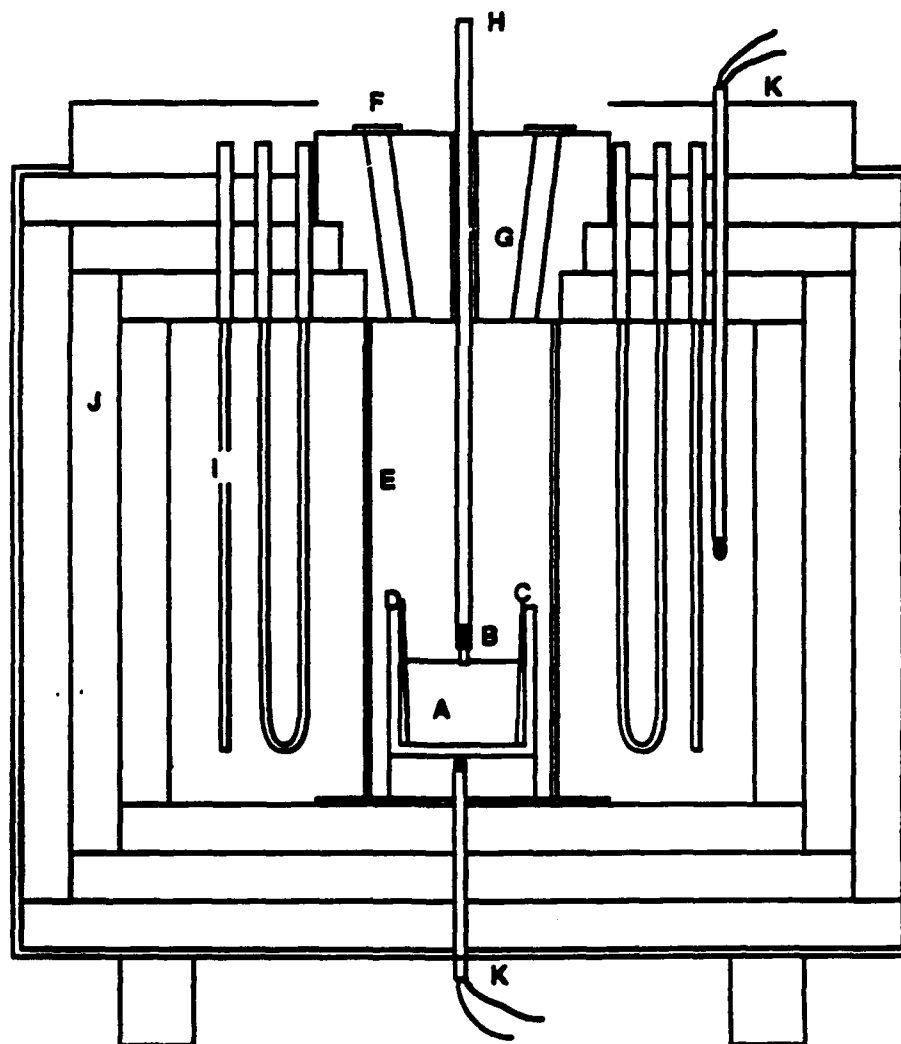


Fig. 2.16 Schematic of the single-zone resistance heated furnace.

This isothermal condition is not suitable for Czochralski growth. In order to produce a temperature gradient above the melt surface, an air-cooled seed rod was used to force a desired gradient. After air cooling was provided, controlled growth was achieved.

From one of the samples grown, a possible vapor etching of the seed was observed. In order to solve this problem, two tricks were used:

- (1) before growing, use the cooling rod to blow air above melt surface for 1-3 mins.
- (2) prior to pulling, dip the seed into the melt to fix the broken regions inside the grooves which are used to attach the seed to the platinum seed holder.

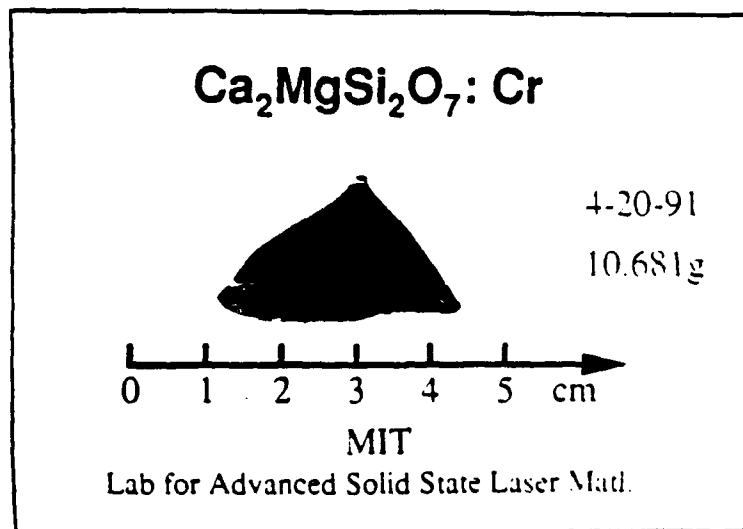


Fig. 2.17 Photo of the crystal grown by using air blowing and crystal dipping techniques.

After these two tricks were performed, crystal growth proceeded rather smoothly and yielded the crystal shown in Fig. 2.17. This crystal was grown rather slowly at about 0.8mm/hrs compared to 2mm/hrs in the rf furnace's. Some defects were incorporated in the middle region and unsymmetrical growth was observed indicating that the crucible was not properly centered. Seed orientation along [100] or [110] induced faceted growth.

2.2.5 Conclusion

- (1) The characteristics of three different kinds of furnaces were explored. The rf induction heated furnace has a greater thermal gradient and is best controlled by power input. The resistance heated furnace need external cooling to force a temperature gradient near the growth interface.
- (2) All the crystals were grown from a crucible less than half-full of melt. This low height of melt, which inhibits both natural and forced convective flows, will produce an undesired growth interface and thus poor optical quality crystals.
- (3) Growing along [001] and a properly centered crucible are needed to attain symmetric growth.
- (4) Defect inclusions made crystals unacceptable. Some growth parameters need to be changed such as rotation rates, temperature lowering rates, etc..

References

- 1 K. Fujino, S. Sasaki, Y. Takeuchi and R. Sadanaga, "X-ray Determination of Electron Distributions in Forsterite, Fayalite and Tephroite," *Acta Cryst.*, B37, p513, 1981.
- 2 W. A. Deer, R. A. Howie, J. Zussman, "Rock Forming Minerals," V1, P2-33, John Wiley and Sons Inc., New York, 1962.
- 3 J. V. Smith, "Reexamination of the Crystal Structure of Melilite," *American Mineralogist*, V39, p643, 1953.
- 4 W. A. Deer, R. A. Howie, J. Zussman, "Rock Forming Minerals," V1, P236-255, John Wiley and Sons Inc., New York, 1962.
- 5 S. F. Bartram, "Crystal Structure of $\text{Y}_2\text{SiBe}_2\text{O}_7$," *Acta Cryst.*, B25, p791, 1969.
- 6 T. H. Allik, M. J. Ferry, R. J. Reeves, R. C. Powell, W. W. Hovis, D. P. Caffey, R. A. Utano, L. Merkle and C. F. Campana, "Crystallography, Spectroscopic Analysis, and Lasing Properties of $\text{Nd}^{3+}:\text{Ba}_2\text{ZnGe}_2\text{O}_7$," *J. Opt. Soc. Am.*, B7(7), p 1190, 1990.
- 7 Structure Reports, V17, p574, 1953.
- 8 M. Alam, K. H. Goen, B. D. Barlolo, A. Linz, E. Sharp, L. Gillespie and G. Jannery, "Optical Spectra and Laser Action of Neodymium in a Crystal $\text{Ba}_2\text{MgGe}_2\text{O}_7$," *J. Appl. Phys.*, V39, p4728, 1968.
- 9 N. A. Sirazhiddinov, N. N. Mirababaeva, R. G. Grebenshchikov, and E. V. Strganov, "Isomorphism of Barium Germanosilicates in the Ba_2SiO_4 , Ba_2GeO_4 || MSiO_3 , MGeO_4 Quaternary Reciprocal System," *Russian Journal of Inorganic Chemistry*, V19(6), p817, 1974.
- 10 J. R. Smith, R. M. Hazen, "The Crystal Structures of Forsterite and Hortonolite at Several Temperatures Up to 900°C ," *Amer. Mineral.*, V58, p588, 1973.

- 11 J. B. Ferguson and H. E. Merwin, "The Ternary System CaO-MgO-SiO₂," Amer. Journ. Sci., 4th ser., V48, p109, 1919.
- 12 J. C. Brice, "Crystal Growth Processes", Chapter 4, Blackie & Son Ltd., Bishopbriggs, 1986.
- 13 Peter H. Kloumann, "Operations Manual for PC Based Crystal Growth System," Crystal Physics Lab., 1991.

Chapter 3

Theory of Chromium Ions in Tetrahedral Sites

3.1 Environment Consideration

When a small amount of chromium metal ions are introduced into solids, we can assume that the chromium ions only interact with the local environment (in this case, oxygen ions). The main hamiltonian for the impurity ion is

$$\mathcal{H} = \sum_{k=1}^n \left\{ \frac{1}{2m} \mathbf{p}_k^2 - \frac{Ze^2}{r_k} + \xi(r_k) \mathbf{l}_k \cdot \mathbf{s}_k + \sum_{k < \lambda}^n \frac{e^2}{r_{k\lambda}} + V(r_k) \right\} \quad (3.1)$$

The first term is the electron kinetic energy and the second term represents the Coulomb interaction due to electrons and the central nucleus; the third, forth and fifth terms respectively are the spin-orbit interaction, electron-electron interaction and interaction due to electrons and local environments. The first four terms have the same form as for the free ion, but the last term is solely due to the interaction of the ion with the rest of solid. In order to write down the explicit form of the fifth term, we must make several assumptions.

First, we can model the environment as a classical distribution of charge. Second, the ionic crystal model which assumes that the electrons are solely bounded to metal ions or the cations can be used. Thus we can write down

$$V_{\text{crystal}}(r_k) = \sum_i \frac{Ze^2}{r_{ki}} \quad (3.2)$$

which we call the crystal field.

The relative magnitudes of the five terms in Eqs 3.1 are important for calculating the energy levels, especially the spin-orbit interaction and the crystal field interactions. According to their relative strengths, they can be classified the following two ways.

(1) weak field scheme: The crystal field is smaller than the spin-orbit interaction. We therefore solve for the free ions' energy levels first and then treat the crystal field as a first order perturbation. Rare earth or actinide ions are usually in this class, because 4f and 5f electrons are well shielded from the crystal field by other electrons.

(2) strong field scheme: The crystal field is stronger than the spin-orbit interaction. So we must consider the crystal field first and then treat spin-orbit interaction as a first order perturbation. Transition metal ions in oxide crystals are usually in this class. The d electron orbitals extend to the exterior of the atoms and have strong interaction with the crystal field.

We would expect that chromium ions in oxides' tetrahedral sites should belong to the latter case. From now on only the strong field scheme will be considered.

In the strong field scheme, we first solve the crystal potential component and then the Coulomb repulsion between the electrons (if the metal ion has more than one electron which is the case for divalent, trivalent and the tetravalent chromium). Finally, spin-orbit coupling and low symmetry components of the crystal field are treated as perturbations.

The crystal potential possess (and also the electron-electron interaction and kinetic energy) all the symmetry elements of the group of the site. For a tetrahedral site, the appropriate group is T_d . Before chromium ions are put into the solid, the free ion has full rotational symmetry. The characters of the angular momentum state ℓ under rotation α degrees about the z axis and rotation α plus inversion are¹

$$\begin{aligned}\chi^{(\ell)}(\alpha) &= \frac{\sin(\ell + 1/2)\alpha}{\sin(1/2)\alpha} \\ \chi^{(\ell)}(i\alpha) &= (-1)^\ell \frac{\sin(\ell + 1/2)\alpha}{\sin(1/2)\alpha}\end{aligned}\tag{3.3}$$

After the ions are put into tetrahedral sites (shown in Fig. 3.1), the full rotation symmetry of free ions is reduced to the symmetry of T_d , whose operations consist of:

- identity E
- 8 C_3 about 4 body diagonals corresponding to rotation $\pm 2\pi/3$
- 3 C_2 about x, y, z directions
- 6 S_4 about x, y, z corresponding to rotation of $\pm\pi/2$
- 6 σ_d planes that are diagonal reflection planes

The character table for T_d symmetry is shown in Table 3.1.

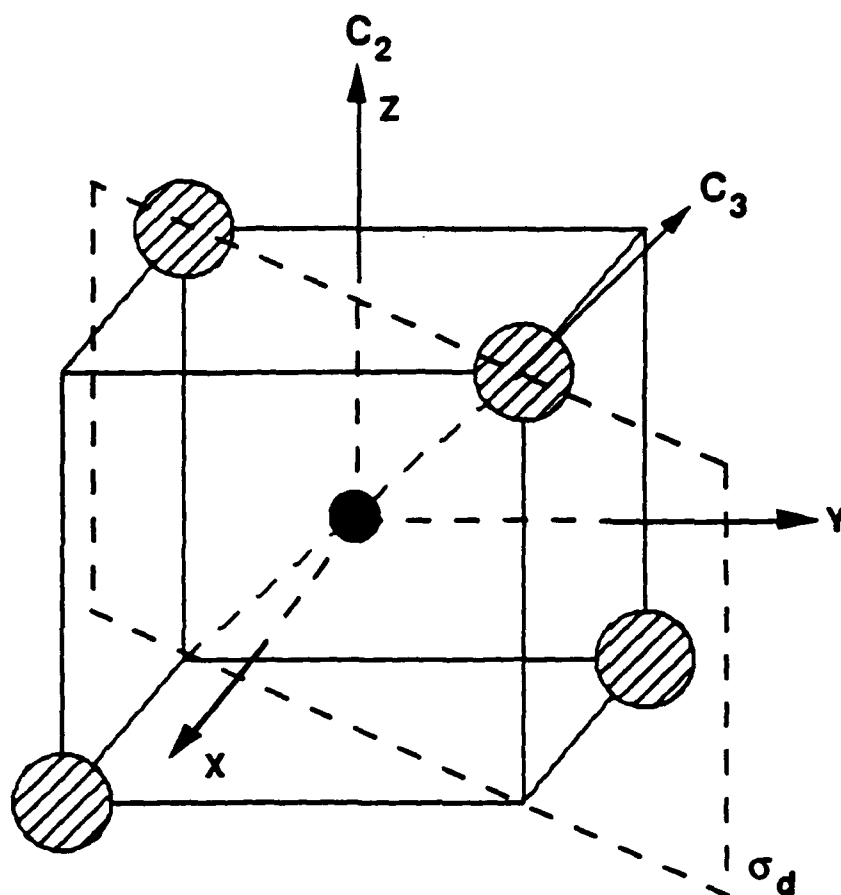


Fig. 3.1 Symmetry operations of tetrahedral sites.

Table 3.1 Character table for T_d symmetry and the corresponding $l=2$ full rotation state.

$T_d(43m)$	E	$8C_3$	$3C_2$	$6\sigma_d$	$6S_4$
A_1	1	1	1	1	1
A_2	1	1	1	-1	-1
E	2	-1	2	0	0
T_1	3	0	-1	-1	1
T_2	3	0	-1	1	-1

Full ROT for $l=2$	5	-1	1	1	-1
-----------------------	---	----	---	---	----

We can also use Eqs. 3.3 to calculate the corresponding characters for the free orbit angular momentum state $\ell=2$ (d state) under the operations of T_d symmetry. The results are shown in Table 3.1.

According to the reduction theorem of reducible representations, the characters of reducible representation $\chi(C_k)$ (full rotation in tetrahedral sites) is a linear combination of characters for the irreducible representation of group T_d .

Comparing the characters of full rotation in a tetrahedral site with the characters of T_d group, we get

$$\chi(\ell=2) = E + T_2$$

In T_d symmetry, the five fold degenerate d functions will therefore split into two sets with irreducible representation E and T_2 . And the corresponding eigenfunctions for the \mathcal{H} crystal-field are

$$\begin{array}{ll} E & d_{x^2-y^2} = (1/\sqrt{2})(d_2+d_{-2}) = (\sqrt{3}/2)(x^2-y^2) \\ & d_{z^2} = d_0 = 1/2(3z^2-r^2) = 1/2(2z^2-x^2-y^2) \\ \\ T_2 & d_{xy} = (1/\sqrt{2})(d_2-d_{-2}) = \sqrt{3}xy \\ & d_{xz} = (1/\sqrt{2})(d_1-d_{-1}) = \sqrt{3}xz \\ & d_{yz} = (1/\sqrt{2})(d_1+d_{-1}) = \sqrt{3}yz \end{array} \quad (3.4)$$

Although group theory describes the degeneracy and splitting, it does not tell us the magnitude and the orderings of the splitting. These quantities can be calculated from the eigenfunctions and crystal fields. The potential of identical

nearest neighbors for various arrangements of d^n configurations are²

$$V_{bcc} = 8\gamma_{00} - 4 \frac{\sqrt{7}}{9} \gamma_{40} r^4 (\sqrt{7}z_{40} + \sqrt{5}z_{44}^c)$$

for 8 ligands in the vertices of a cube and the ion sitting in the body center

$$V_{tet} = 4\gamma_{00} - 2 \frac{\sqrt{7}}{9} \gamma_{40} r^4 (\sqrt{7}z_{40} + \sqrt{5}z_{44}^c)$$

for 4 ligands in the vertices of a regular tetrahedron

$$V_{oct} = 6\gamma_{00} + \frac{\sqrt{7}}{2} \gamma_{40} r^4 (\sqrt{7}z_{40} + \sqrt{5}z_{44}^c)$$

for 6 ligands in the vertices of a regular octahedron (3.5)

where $z_{\ell 0} = y_{\ell 0}$

$$z_{\ell m}^c = (1/2) (\alpha_{\ell-m} + y_{\ell-m}^*)$$

$$\gamma_{k\alpha} = -\frac{4\pi e}{2k+1} \int \frac{\rho(R) z_{k\alpha}(\theta, \phi)}{R^{k+1}} d\vec{r}$$

$\rho(R)$ is the spatial charge distribution

After calculating the hamiltonian matrices associated with the basis functions E and T_2 using the tetrahedral potential, we get the following results:

$$\begin{aligned} \langle T_2 | V_{tet} | T_2 \rangle &= 1/\sqrt{4\pi} (4\gamma_{00} + (8/9)\gamma_{40} r^4) \\ \langle E | V_{tet} | E \rangle &= 1/\sqrt{4\pi} (4\gamma_{00} - (4/3)\gamma_{40} r^4) \\ \langle T_2 | V_{tet} | E \rangle &= 0 \end{aligned} \quad (3.6)$$

which confirm the energy splitting results derived from the group theory.

The difference of energy between the two representations is

$$E(T_2) - E(E) = 20/(9 \cdot \sqrt{4\pi}) \gamma_4 \overline{r^4} = 10Dq \quad (3.7)$$

Dq is an important parameter in the crystal field theory which describe the magnitude of the cubic crystal field. And from Eqs. 3.5, it is very easy to get the following relations between different cubic environments assuming that the charge distributions around the ions and the distances between the ions are the same.

$$(Dq)_{bcc} = 2(Dq)_{tet} = -2(4/9)(Dq)_{oct} \quad (3.8)$$

3.2 d^2 and d^3 in Cubic Environments

If there exists more than one d electron in the atom, we must consider the Coulomb interaction between d electrons. But first, we can use the direct product of groups to get the irreducible representations of many-electron wavefunctions. For example, Cr^{4+} have two d electrons. If both electrons are in the E level, Coulomb interaction will split it into A_1 , A_2 and E levels by the following formulas.

$$E \times E = A_1 + A_2 + E$$

By the same reason,

$$\begin{aligned} T_2 \times T_2 &= A_1 + E + T_1 + T_2 \\ E \times T_2 &= T_1 + T_2 \end{aligned}$$

For spin part,

$$(S=1/2) \times (S=1/2) = S=0 \text{ or } 1 \quad (3.9)$$

then we can apply the well-known formula to construct the wavefunctions:

$$\Theta(SM) = \sum_{m_1, m_2} \Theta(s_1 m_1) \Theta(s_2 m_2) \langle s_1 m_1 s_2 m_2 | SM \rangle \quad (3.10)$$

$\langle s_1 m_1 s_2 m_2 | SM \rangle$ are Wigner coefficients (or Clebsch-Gordan coefficients) which are tabulated in standard group theory books. After applying Eqs. 3.10, some of the combinations vanish and only the following terms survive.

$^1A_1(T_2^2)$, $^1A_1(E^2)$, $^1E(T_2^2)$, $^1E(E^2)$, $^1T_2(T_2^2)$, $^1T_2(T_2E)$, $^3T_1(T_2^2)$, $^3T_1(T_2E)$, $^1T_1(T_2E)$, $^3T_2(T_2E)$ and $^3A_2(E^2)$

The number in the upper left hand corner represents the spin degeneracy $2S+1$, while the representation inside the bracket is the original electron configurations without Coulomb interactions.

Since the Coulomb interaction shown in Eqs 3.1 also has the full symmetry of the crystal, energy levels with the same symmetry will mix together. Of all the possible cross terms between levels, we only need to consider terms having the same symmetry. The appropriate matrix elements have been compiled by Tanabe and Sugano.³ These matrix elements and eigenenergies are listed in the Appendix. According to the eigenenergies calculated from the formula in the Appendix, we can construct the Tanabe-Sugano (T-S) diagrams that represent the energy ratio E/B as a function of Dq/B (the definition of B is in Appendix). The Tanabe-Sugano diagrams which have achieved great success in interpreting the spectra of transition-metal ions in cubic environments will be used in conjunction with the absorption spectra in Chapter 3. A typical energy levels ordering for Cr^{4+} ions in tetrahedral sites are shown in Fig. 3.2.

For d^3 configuration, we can follow exactly the same procedure by using the direct product method. The resulting symmetry, matrix elements and eigenenergies are also listed in Appendix.

It is interesting compare the d^n with d^{10-n} configuration. A d^{10-n} configuration forms a full shell in conjunction with a d^n configuration. As a matter of fact, the states $t_2^{6-n}(S_1\Gamma_1)e^{4-m}(S_2\Gamma_2)S\Gamma-Mr$ are complementary states to the $t_2^n(S_1\Gamma_1)e^m(S_2\Gamma_2)S\Gamma-Mr$. Under the approximation that all E and T_2 functions are d-functions, the matrix elements in $N=6,7,8,9$ can be obtained from $N=1,2,3,4$ by replacing $t_2^n(S_1\Gamma_1)e^m(S_2\Gamma_2)S\Gamma-Mr$ with $t_2^{6-n}(S_1\Gamma_1)e^{4-m}(S_2\Gamma_2)S\Gamma-Mr$. So in the d^8 configuration, we can still use the matrix elements and eigenenergies of the d^2 configuration.

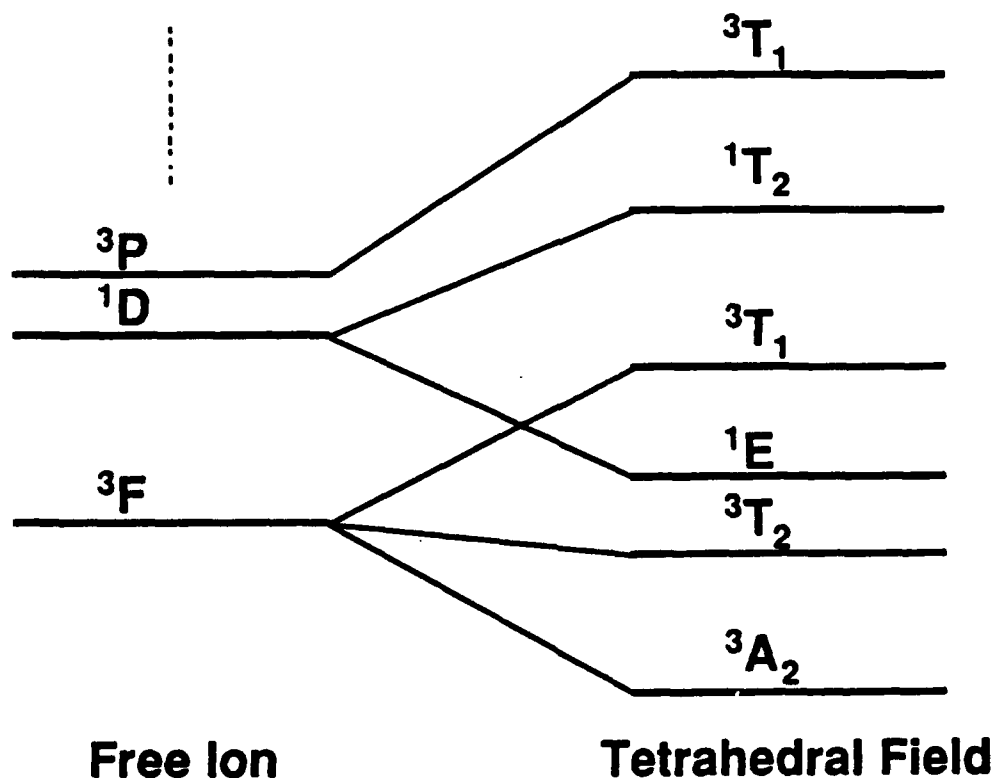


Fig. 3.2 Energy level diagram for a d^2 ions in a tetrahedral field.

3.3 Spin-Orbit Interaction and Low Symmetry Fields

The energy splittings due to the spin-orbit interaction and the low symmetry fields in transition metal ions are usually one order of magnitude smaller than the electronic Coulomb interaction. Therefore, we can treat the spin-orbit interaction and the low symmetry field as perturbations.

The hamiltonian associated with the spin-orbit interaction can be written as⁴

$$\mathcal{H} = \sum_i \xi(r_i) \mathbf{l}_i \cdot \mathbf{s}_i \quad (3.11)$$

which after some arithmetic manipulations can be rewritten by using tensor operator equivalence as³

$$\mathcal{H}_{so} = 1/\sqrt{2} [-V_{+1}\alpha(^1T_1) + iV_{+1}\beta(^1T_1)] + 1/\sqrt{2} [-V_{-1}\alpha(^1T_1) + iV_{-1}\beta(^1T_1)] + V_0\gamma(^1T_1) \quad (3.12)$$

where $V_{\pm 1}\alpha = \sum_i s_i s_{i\pm 1} t_{i\alpha}$, $V_{\pm 1}\beta = \sum_i s_i s_{i\pm 1} t_{i\beta}$, $V_{\pm 0}\gamma = \sum_i s_i s_{i0} t_{i\gamma}$
 $s_{i\pm 1} = \mp 1/\sqrt{2} (s_{ix} \pm i s_{iy})$, $s_{i0} = s_{iz}$
 $t_{i\alpha} = \xi(r_i) l_{ix}$, $t_{i\beta} = \xi(r_i) l_{iy}$, $t_{i\gamma} = \xi(r_i) l_{iz}$

One way to look at the Eqs. 3.12 is that the orbital angular momentum states, l_{ix} , l_{iy} , l_{iz} , transform as the T_1 irreducible representation in cubic symmetry. Therefore, we can use the basis functions of T_1 to evaluate the hamiltonian.

In real crystals, there is always some distortion to perfect cubic environments, so we often get a low symmetry component of the crystal field. For a low symmetry crystal field, we can also write down the corresponding tensor operators based on the form of potential.³ For example, in D_{4h} symmetry, the potential can be expressed as $V_u(E_g)$, and the D_{3d} symmetry as $\{V_\xi(T_{2g}) + V_\eta(T_{2g}) + V_\zeta(T_{2g})\}$

Thus we can calculate the matrix elements between different terms as $\langle \alpha S \Gamma | \mathcal{H}_{SO} + \mathcal{H}_{\text{low-symmetry}} | \alpha' S' \Gamma' \rangle$. Then, standard perturbation procedure can be used to get the new energy levels.

Sometimes, the low symmetry field will have larger strength than the Coulomb interaction; in these cases the perturbation procedure cannot be used. Under these circumstances, we must first calculate the energy splitting due to the whole crystal field, then calculate the Coulomb energy, and lastly treat spin-orbit interactions as perturbations. The whole procedure is very similar to the procedure stated in section 3.1, but the lower symmetry is, the more complex the procedure is. Otsuka has worked out the case of tetragonal fields.⁵

3.3.1 Energy Level Splitting of Ground State

The method stated in the last section, although straightforward, is still very complicated, especially when the spin-orbit interaction and low symmetry field parameters are included in the calculations. So instead of solving the real hamiltonian, we can approach this problem phenomenologically by constructing an effective hamiltonian.

In this section, I will use the spin hamiltonian matrices to account for the effects of all the low order interactions, which include the spin-orbit interaction and spin-spin interaction⁸ on the d^2 ground state energy of chromium ions in tetrahedral sites. (this calculation will be used in electron spin resonance experiments in Chapter 4). For Cr^{4+} ions in forsterite and åkermanite, the ground state is 3A_2 (see the Appendix).

Due to the presence of the low symmetry field, the ground state is usually an orbital singlet with representation $2s+1A_1$ or

$2s+1A_2$. The ground state wavefunctions will be split further by the spin-orbit interaction, spin-spin interaction, etc.. The general form of the ground state hamiltonian for $s=1/2$ is

$$\mathcal{H}_{\text{so+low symm}} = \begin{pmatrix} a & c-id \\ c+id & b \end{pmatrix}$$

which can be rewritten by using the well-known spin matrices $\Theta(1/2, \pm 1/2)$ (notice, $\mathcal{H}=\mathcal{H}^*$).

$$\mathcal{H}_{\text{so+low symm}} = 1/2(a+b)1 + (a-b)S_z + 2cS_x + 2dS_y \quad (3.13)$$

$$\text{where } 1 = \begin{pmatrix} 1 & 0 \\ 0 & 1 \end{pmatrix} S_x = \begin{pmatrix} 0 & 1 \\ 1 & 0 \end{pmatrix} S_y = \begin{pmatrix} 0 & -i \\ i & 0 \end{pmatrix} S_z = \begin{pmatrix} 1 & 0 \\ 0 & -1 \end{pmatrix}$$

In the same manner, we can express the $S=1$ system by linear combinations of $1, S_x, S_y, S_z, S_yS_z + S_zS_y, S_zS_x + S_xS_z, S_xS_y + S_yS_x, S_z^2, S_x^2 - S_y^2$. Initially, it might seem that we do not get any advantage as we still have a lot of linear coefficients to determine. But by noticing the following facts: (1) the orbit singlet ground state, $\Psi(2S+1A_{1,2}M_{1,2})$ has the same transformation properties as $\Theta(SM)f(A_1 \text{ or } A_2)$; (2) the orbital part transforms as the symmetry of the wavefunctions (A_1 or A_2); (3) then the base functions of the spin matrix $\Theta(SM)$ must transform as A_1 (the identity irreducible representation), in order for the whole wavefunctions to have the symmetry A_1 or A_2 ; (4) the hamiltonian has time-reversal symmetry³, we can greatly simplify the effective hamiltonian.

For example, for a spin-triplet state in D_2 symmetry environment, we can use $\Theta(1M)$ ($1, S_x, S_y, S_z, S_yS_z + S_zS_y, S_zS_x + S_xS_z, S_xS_y + S_yS_x, S_z^2, S_x^2 - S_y^2$) as the bases. The time reversal operator is defined as $K_s\Theta(1/2, m) = (1/2)^{-m}\Theta(1/2, -m)$. By

applying the time reversal symmetry to $\Theta(1M)$, the S_x, S_y, S_z linear terms which change sign are required by symmetry to have zero coefficients. Also by applying the 2-fold rotational symmetry along x, y, z axes, the terms $S_y S_z + S_z S_y, S_z S_x + S_x S_z, S_x S_y + S_y S_x$ which change sign should also have zero coefficients. Then the effective hamiltonian can be simplified as

$$\mathcal{H} = D[S_z^2 - 1/3 S^2] + E(S_x^2 - S_y^2) \quad (3.14)$$

where D and E are the fine structure parameters which need to be determined experimentally. The constant term $-1/3 S^2$ is included so that the trace of the matrix is zero.

For states with symmetry Γ other than A_1 and A_2 , we must use the bases $\phi(\Gamma' \gamma)$ which transform like the direct product of $\Gamma \times \Gamma$. For example, the hamiltonian of excited state 3T_2 can be written as⁶

$$\mathcal{H} = -\Delta(L_z^2 - 2/3) - \Gamma(L_x^2 - L_y^2) + (\lambda_x S_x L_x + \lambda_y S_y L_y + \lambda_z S_z L_z) \quad (3.15)$$

Let us go back to Eqs. 3.14. The whole hamiltonian is (where I neglect the common factor $S^2/3$)

$$\begin{pmatrix} D/3 & 0 & E \\ 0 & -2D/3 & 0 \\ E & 0 & D/3 \end{pmatrix}$$

After solving the above matrix, the eigenenergies are found to be

$$E_1 = D/3 + E, \quad E_2 = D/3 - E, \quad E_3 = -2D/3 \quad (3.16)$$

As can be seen, the ground state will split into triplet states with the energies given above.

Now, consider the case when an external magnetic field is applied to the crystal (this is the case in electron paramagnetic resonance experiments). According to quantum mechanics, the magnetic moments produced by the electron spin and orbital motion will precess around the magnetic field H with the energy

$$\Delta E = -\mu \cdot H = -\mu H \cos(\mu, H) \quad (3.17)$$

where μ is magnetic moments due to the spin and orbital magnetic moments

$$\mu = -(\mu_B/\hbar)(\sum_i L_i + 2\sum_i S_i) = -(\mu_B/\hbar)(L' + 2S') \quad (3.18)$$

where μ_B is Bohr magnetron, and L', S' , the total orbit and spin angular momentum.

But when the ground state is an orbital singlet state due the low symmetry field, its orbital angular momentum is zero. The reason is:

The wavefunction of nondegenerate ground state must have the form of Eqs. 3.4 to match the corresponding irreducible representation. (notice the wavefunctions of Eqs. 3.4 which transform as $xy, yz, zx, 3x^2-y^2, x^2-y^2$ are linear combinations of angular momentum eigenstates, d_{-2}, d_{-1}, d_0, d_1 and d_2). So the wavefunctions have real forms. But the operator L_z for the z component of the orbital angular momentum is a purely imaginary operator.

$$L_z = i\hbar(x\partial/\partial y - y\partial/\partial x) \quad (3.19)$$

L_z is also a hermitian operator whose eigenvalue is real. So the only possible solution of the eigenequation $L_z\Psi = \ell_z\Psi$ is $\ell_z=0$. In this case, the orbital angular momentum is quenched. So in the ground state, we can ignore the spin-orbit interaction and also let

$L'=0$ in Eqs. 3.17. So by combining Eqs. 3.17 and 3.14, we get the spin-hamiltonian for a ground state of 3A_1 or 3A_2 in an external magnetic field.

$$\mathcal{H} = \beta \mathbf{H} \cdot \mathbf{g} \cdot \mathbf{S} + D[S_z^2 - 1/3 S^2] + E(S_x^2 - S_y^2) \quad (3.20)$$

where $\beta = \mu_B/\hbar$ and the \mathbf{g} tensor is used instead of the isotropic g value of 2.

The energies of the three states as a function of the external magnetic field are plotted in Fig. 3.3. From the Fig. 3.3, we can notice that the magnitude and the ordering of the splitting will be different depending on the direction of the magnetic field. This special feature is extremely useful to identify the site symmetry of the dopant ions in the solid. Detail will be discussed in section 4.3.

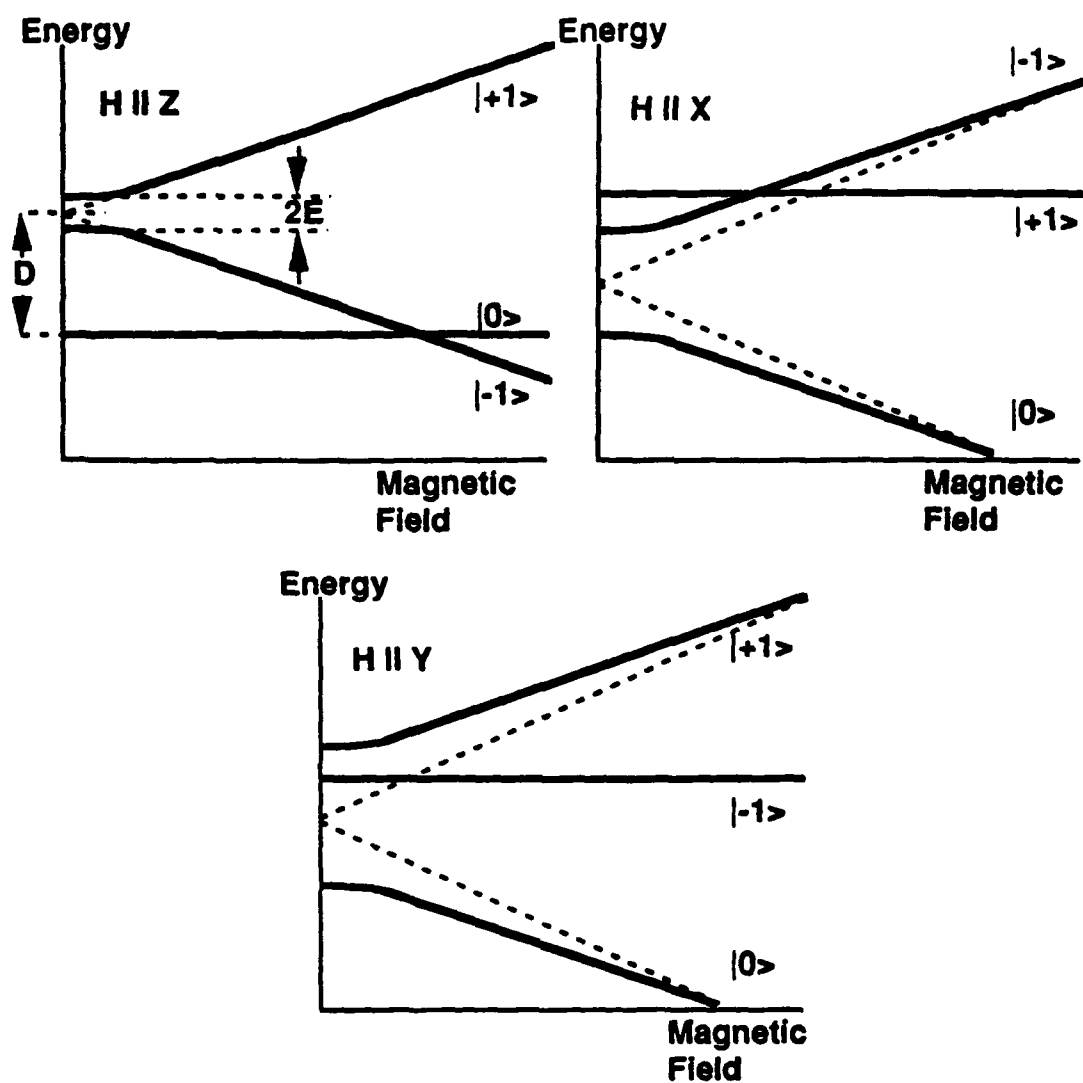


Fig. 3.3 ${}^3A_1/{}^3A_2$ level splitting as a function of H

References

- 1 class notes of 6.734J at M.I.T., "Applications of Group theory to the Physics of Solids," by Prof. M. Dresselhaus.
- 2 J. S. Griffith,, "The Theory of Transition-Metal Ions," Cambridge Univ. Press, London and New York, 1964.
- 3 S. Sugano, Y. Tanabe and H. Kamimura, "Multiplets of Transition-Metal Ions in Crystals," Academic Press, New York, 1970.
- 4 R. M. Eisberg, "Modern Physics," John Wiley and Sons, Inc., New York, 1961.
- 5 Jinya Otsuka, "Electrostatic Interaction of d^n Systems in Tetragonal Fields," J. of Phy. Soc. of Japan, V21(4), p596, 1966.
- 6 J. Ferguson, H. J. Guggenheim, H. Kamimura, and Y. Tanabe, "Electronic Structure of Ni^{2+} in MgF_2 and ZnF_2 ," J. of Chem. Phy., V42(2), p775, 1965.
- 7 J. E. Wertz, J.R. Bolton, "Electron Spin Resonance: Elementary Theory and Practical Applications," Chapman and Hall, New York, 1986.

Chapter 4

Spectroscopy and Analysis

4.1 Experiment Procedure

4.1.1 Optical Spectroscopy

Polarized absorption spectra can be obtained by using an available Perkin-Elmer Lambda 9 spectrophotometer in conjunction with polarizing prisms. Emission spectra are recorded by using a McPherson 218 Scanning Monochromator with 786A Digital Scanning Control and an EG&G 5301 Lock-In Amplifier. Excitation of the emission is by one of the following sources: (1) Spectra Physics 171 Argon Laser; (2) argon laser pumped Ti^{3+} :sapphire laser; (3) argon laser pumped dye laser; (4) Spectra Diode Lab SDL-2422 GaAlAs semiconductor laser. The excitation source is chosen depending on the absorption band pumped. The whole set up is shown in Fig. 4.1.

For fluorescence decay or lifetime measurements, (1) a Holobeam QG 500 pulsed frequency doubled Nd^{3+} :YAG laser; (2) a pulsed Nd:YAG pumped Ti:sapphire laser; (3) a pulsed Molelectron DL-II series nitrogen laser pumped dye laser (also depend on the absorption band pumped) were used for excitation. The decaying signal is recorded by an Analogic Data 6000 Universal Waveform Analyzer in conjunction with a Tektronix 7623 oscilloscope. The whole set up is shown in Fig 4.2.

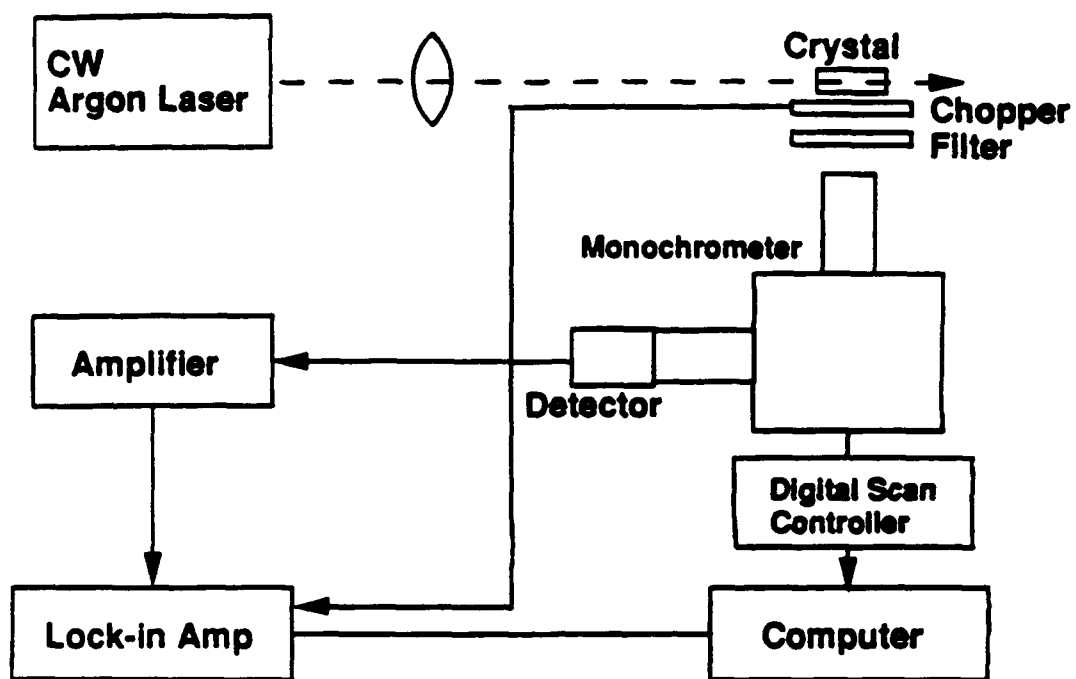


Fig. 4.1 Experimental set-up for emission measurements.

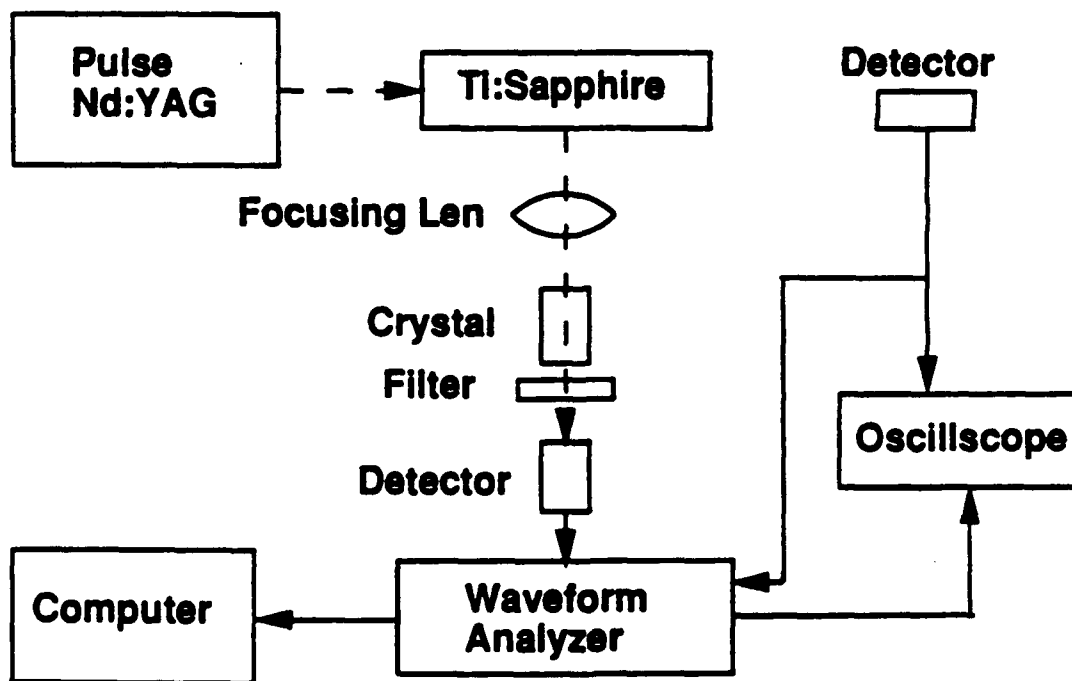


Fig. 4.2 Experimental set-up for life-time measurements.

Detectors ranging from IR/visible photomultipliers, Ge, Si, and InSb photodetectors are used depending on the sensitivity required and the spectral range of interest.

In order to resolve some fine structures, low temperature spectroscopy is needed. An Air Products and a Janis Cryogenic variable temperature cryostats are used in conjunction with the Perkin-Elmer Lambda 9 spectrophotometer and emission set-up to obtain liquid nitrogen or helium temperature spectra.

4.1.2 Electron Paramagnetic Resonance Spectroscopy

Due to the broad energy bands of transition metal ions in solids (which result from lattice interactions), it is difficult to use optical spectroscopy to identify the impurity center. On the other hand, the electron paramagnetic resonance (EPR) spectroscopy has the following advantages¹:

- (1) The microwave frequency used in EPR are 10^6 to 10^{11} Hz which correspond to 10^{-9} to 10^{-4} eV. Such a small energy enables us to investigate the small splitting due to the low symmetry field and the external magnetic field which is not accessible by optical methods.
- (2) By changing the direction of magnetic field, different splittings due to the local symmetry of the impurity center can be explored.
- (3) By changing the strength of magnetic field, different magnitude of energy splitting can be produced.
- (4) Due to different nuclear magnetic dipole moments of different atoms, sometimes we can identify the impurity by observing the characteristics of its hyper fine structure.

(5) By observing the temperature dependence of resonance and using the pulsed EPR method, spin-spin and spin-lattice relaxations of the impurity can be studied.

Because of the above advantages and also the lack of an effective way to identify the impurity center by optical methods, EPR spectroscopy of Cr:forsterite and Cr:åkermanite crystals were performed to assist the identification. (this part of the experimental work was undertaken by graduate student M. H. Whitmore and Prof. D. J. Singel, Chemistry Department, Harvard University).²

The procedure of EPR experiments can be found in any standard magnetic resonance textbooks.^{3,4}

4.2 Results and Analysis of Optical Spectroscopy

4.2.1 Cr:Forsterite

The room temperature polarized absorption spectra of Cr:Mg₂SiO₄ (grown under an oxidizing atmosphere) are shown in Fig. 4.3. The three distinct absorption peaks at 571, 662, and 742nm are found and also weaker absorption bands in the near-infrared region and at 400nm. Since all these bands have considerable overlap, the interpretation of these spectra is difficult. By observing the absorption strength vs. growth atmospheres, Petricevic⁵ and Verdun⁶, Baryshevski⁷ et al, have assigned the various bands to Cr³⁺ in octahedral sites and Cr⁴⁺ in tetrahedral sites.

In my sample (grown under an oxidizing atmosphere), the main features correspond to those identified for Cr⁴⁺ ions in silicon sites. Before looking into the spectra, it is worthwhile to understand the local environment of the Si site in forsterite. The

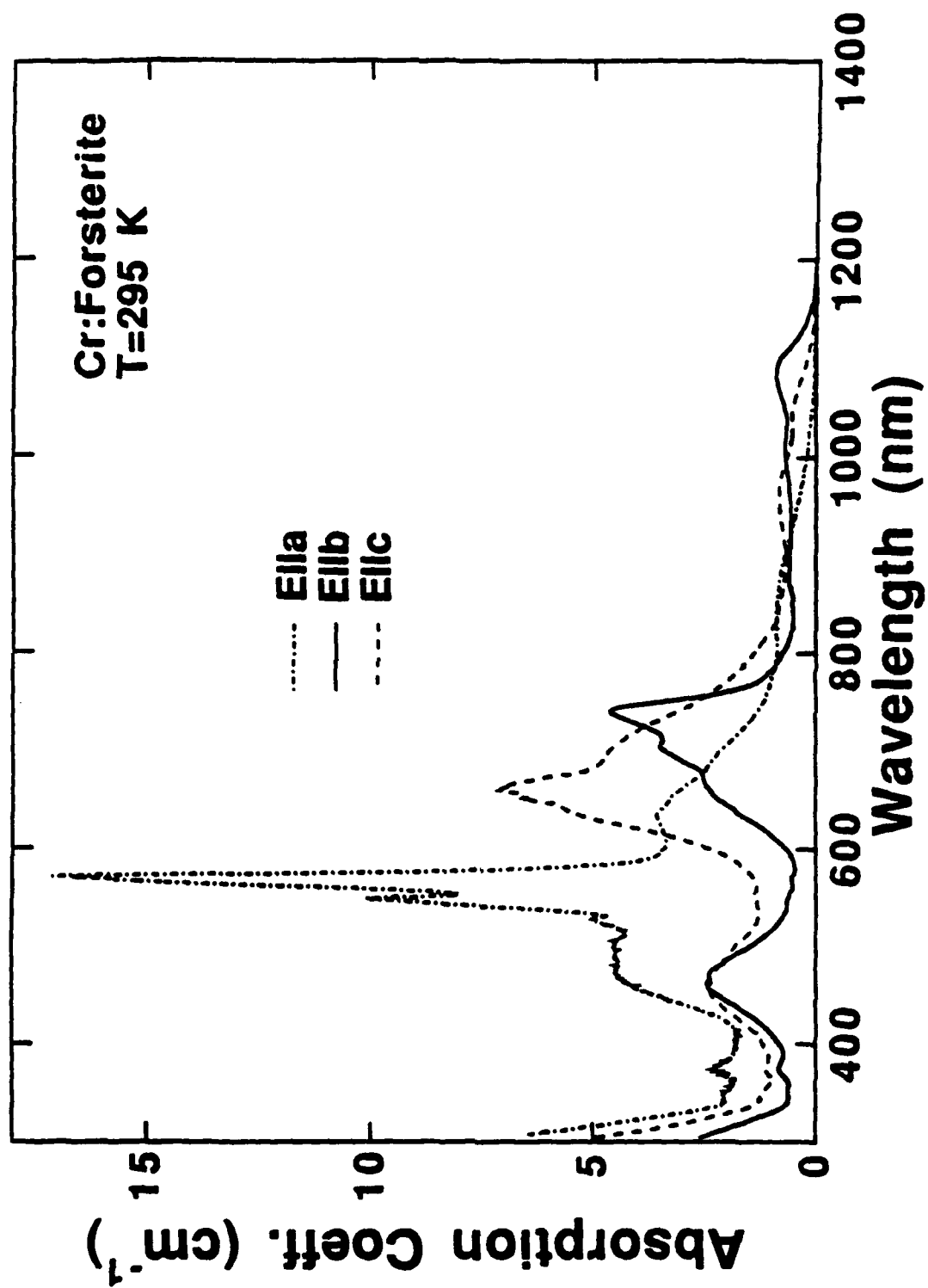


Fig. 4.3 Room temperature absorption spectra of Cr:Mg₂SiO₄.

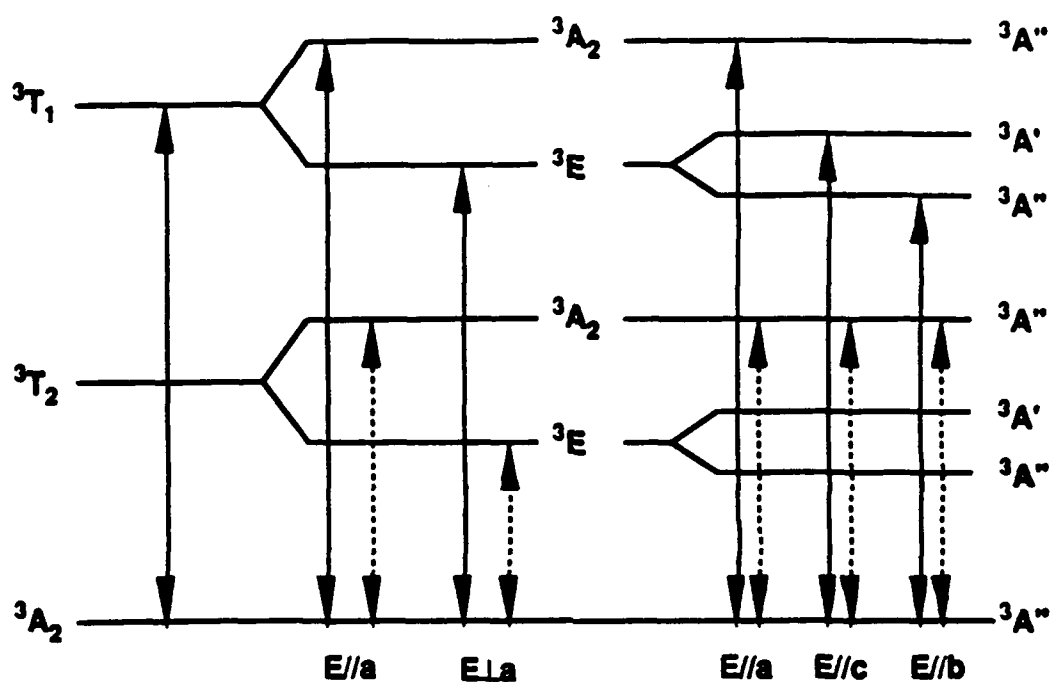


Fig. 4.4 Symmetry descending and associated selection rules.

Si site as shown in Table 2.1 has symmetry C_s lowered from the T_d symmetry of a regular tetrahedron. The distorted tetrahedron was shown in Fig. 2.4. As a first order approximation, we can treat the tetrahedron having strain along a axis which lower the symmetry to C_{3v} . The progression of descending symmetry ($T_d \rightarrow C_{3v} \rightarrow C_s$) and selection rules for electric dipole transitions can be derived from group theory⁶ and are shown in Fig. 4.4. From the figure, we notice that ${}^3A_2 \rightarrow {}^3T_1$ is the only allowed transition in the T_d symmetry. Therefore, we can expect that this ${}^3A_2 \rightarrow {}^3T_1$ transition will be the strongest for Cr^{4+} . The three large peaks in the visible region should therefore belong to the ${}^3A_2 \rightarrow {}^3T_1$ transition. The much weaker near-infrared absorption is due to ${}^3A_2 \rightarrow {}^3T_2$, as can be seen from the energy diagram. By using the mean value of the three peaks and the cubic field approximation (see the Appendix), the crystal field parameters are determined to be $Dq = -1010.8 \text{ cm}^{-1}$, $B = 569.7 \text{ cm}^{-1}$. The parameter C is set to be $4.4B$ as in the free ion case due to the lack of reliable transition assignments to the E states. By using these values for Dq , B , C , and

also the eigenenergy formula in the Appendix, the energy levels of Cr^{4+} in forsterite were calculated. The corresponding energy diagram and Tanabe-Sugano diagram are shown in Fig. 4.5.

Let us compare the result with the data published by Petricevic⁵, Verdun⁶ and Moncorge⁸. The Dq 's values are very similar. However, there exist considerable differences for the B and C values. This is due to the different assignments of the centers of absorption bands to their associated irreducible representations. Even at low temperature, absorption bands still overlap such that the assignments of absorption bands are extremely difficult. But by noticing that the electric-dipole selection rule for S is $\Delta S=0$, we expect that the dominant transitions should be ${}^3A_2 \rightarrow {}^3T_2$ and 3T_1 . From the known $\text{Ni}^{2+}:\text{MgF}_2$ spectra (which is a d^8 configuration in octahedral sites; and the energy structure of d^8 in octahedral sites should be very similar to that of d^2 in tetrahedral sites⁹), the absorption around 350nm, 374nm and 444nm should result from transition from 3A_2 to the second 3T_1 . Even so the more precise calculation is very difficult for the following reasons: (1) the lack of reliable data from 3A_2 to a spin-singlet state; (2) the large low-symmetry field (can be seen from the large splitting of 3T_1 and 3T_2 states); (3) absorption bands overlapping with Cr^{3+} absorption bands; and (4) low local symmetry C_s of the silicon site. Better energy level calculations have been obtained either by the tetragonal field approximation^{7,10} or by treating low symmetry fields as perturbations.¹¹ But neither method has considered the following internal limitations of the crystal field theory:

(1) in a non inversion symmetry environment, the configuration mixing with p states and even f states may be large enough that we can not ignore it.

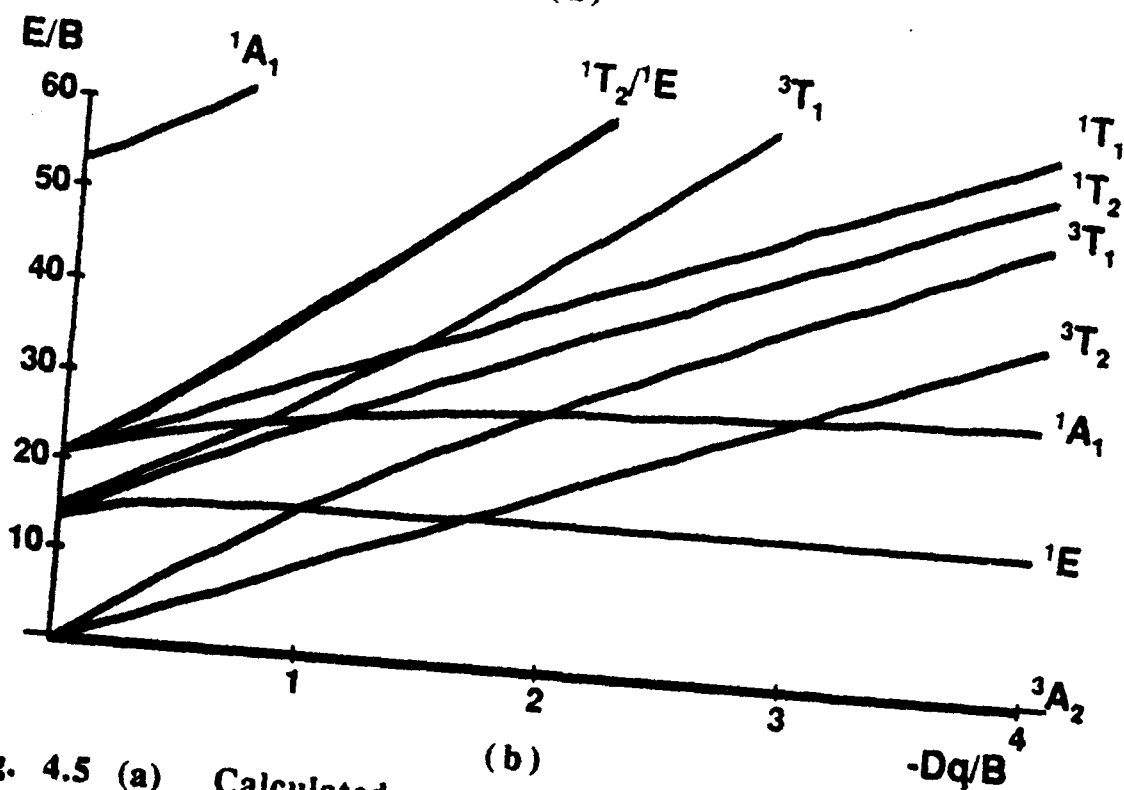
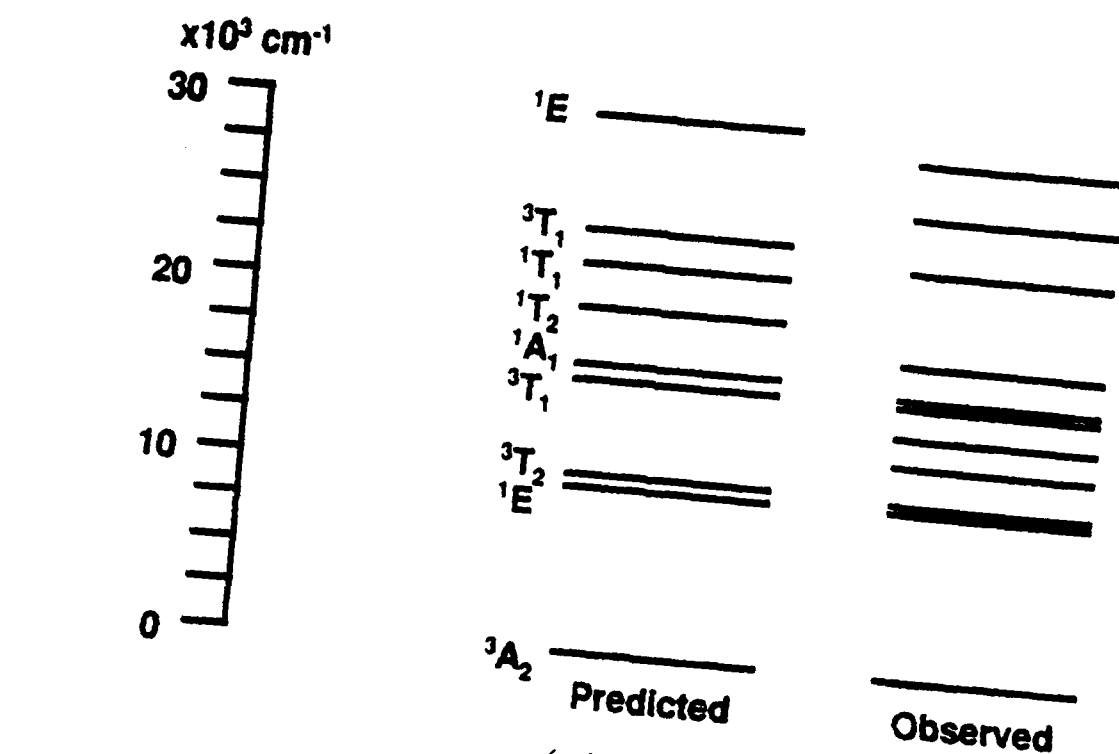


Fig. 4.5 (a) Calculated and predicted energy levels of Cr^{4+} ions in forsterite. (b) Tanabe-Sugano diagram for Cr^{4+} in a tetrahedral coordination with $C=4.4B$.

(2) in such a high valence state, we would expect that some part of the bonding between Cr-O will be covalent. This contradicts the basic ionic crystal approximation of the crystal field theory. In fact, silicon atoms in forsterite have electronic charges +2.1 determined from effective distribution radii¹² instead of the formal charge 4+.

For the illustrative purpose, the cubic field approximation is good enough to explain the general characteristics.

For E//a, we can clearly observe the zero-phonon line and the corresponding phonon sidebands at 17521cm^{-1} (570nm), 18244cm^{-1} (548nm) and 18980cm^{-1} (527nm). The average phonon energy for this structure is 730cm^{-1} . In order to observe the fine structure of other polarizations or frequency regions, liquid-helium temperature absorption experiments were performed. The 10K absorption spectrum for E//b (the same axis as for the dominant emission) is shown in Fig. 4.6. Again, three peaks at 13474cm^{-1} (742nm), 14217cm^{-1} (704nm) and 14935cm^{-1} (668nm) are observed. The average phonon energy is 730cm^{-1} and is consistent with the E//a room temperature absorption spectrum. The zero phonon line for the ${}^3\text{A}_2 \rightarrow {}^3\text{T}_2$ transition is also easily identified at 1090nm with very clear vibronic structures. This result is very similar to $\text{Ni}^{2+}(\text{d}^8)$ in MgF_2 . Therefore, the assumption that Cr^{4+} ions are in silicon sites is consistent.

Forsterite has emission in the near-infrared region. The room temperature polarized emission spectra for the near-infrared region excited by 0.3W argon laser pumping at 488nm with k//c are shown in Fig. 4.7. The spectra were recorded using a McPherson 0.3 monochromator with a 1200 grooves/mm grating and a Ge detector. For E//a, the small emission signal may be due to the slight mis-alignment of the crystal. For the E//c spectrum, we notice that there is an emission region extending below 1000nm which is quite different from the E//b spectrum. For the

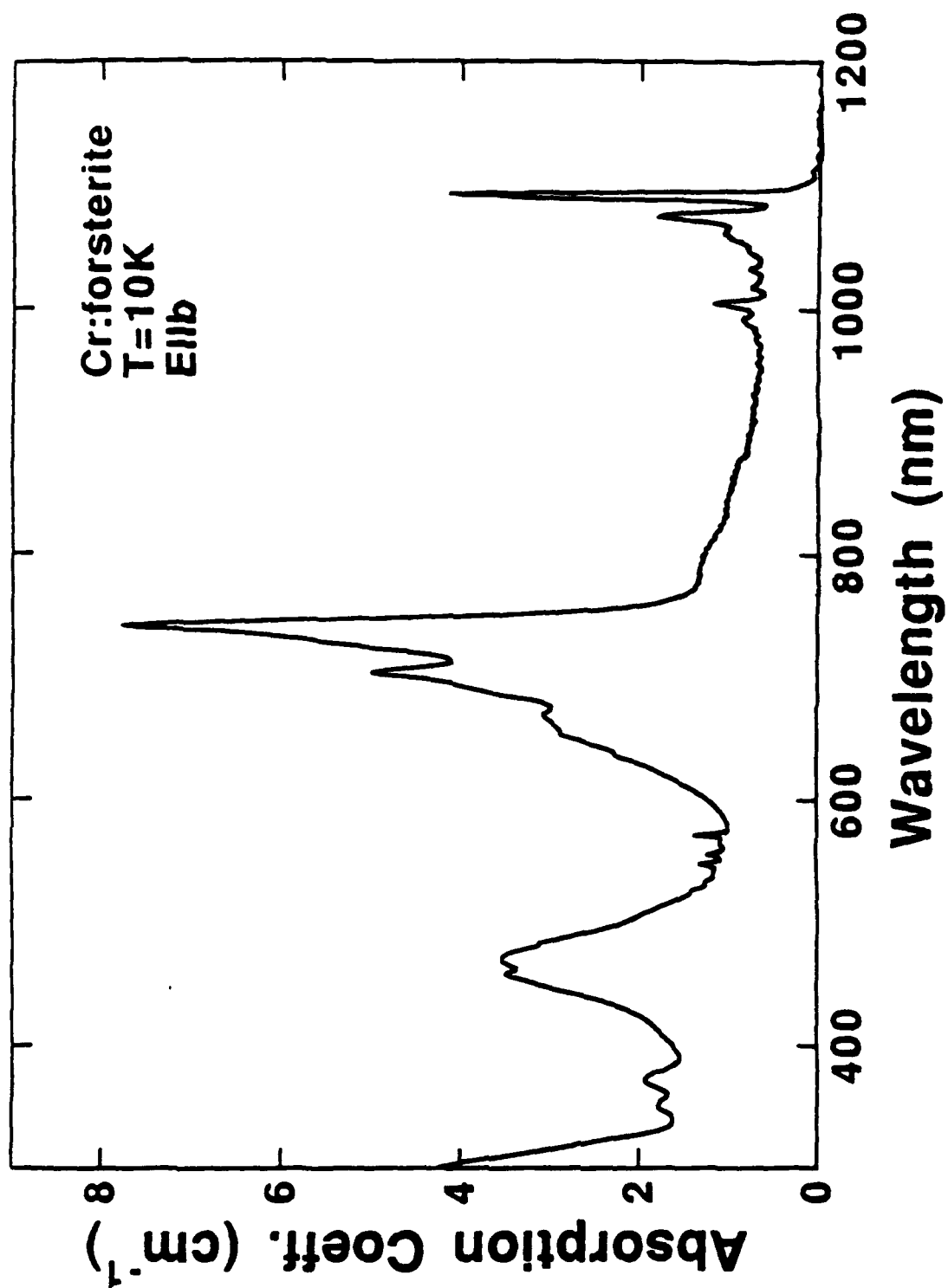


Fig. 4.6 10K absorption spectrum of Cr:Mg₂SiO₄ for E//b.

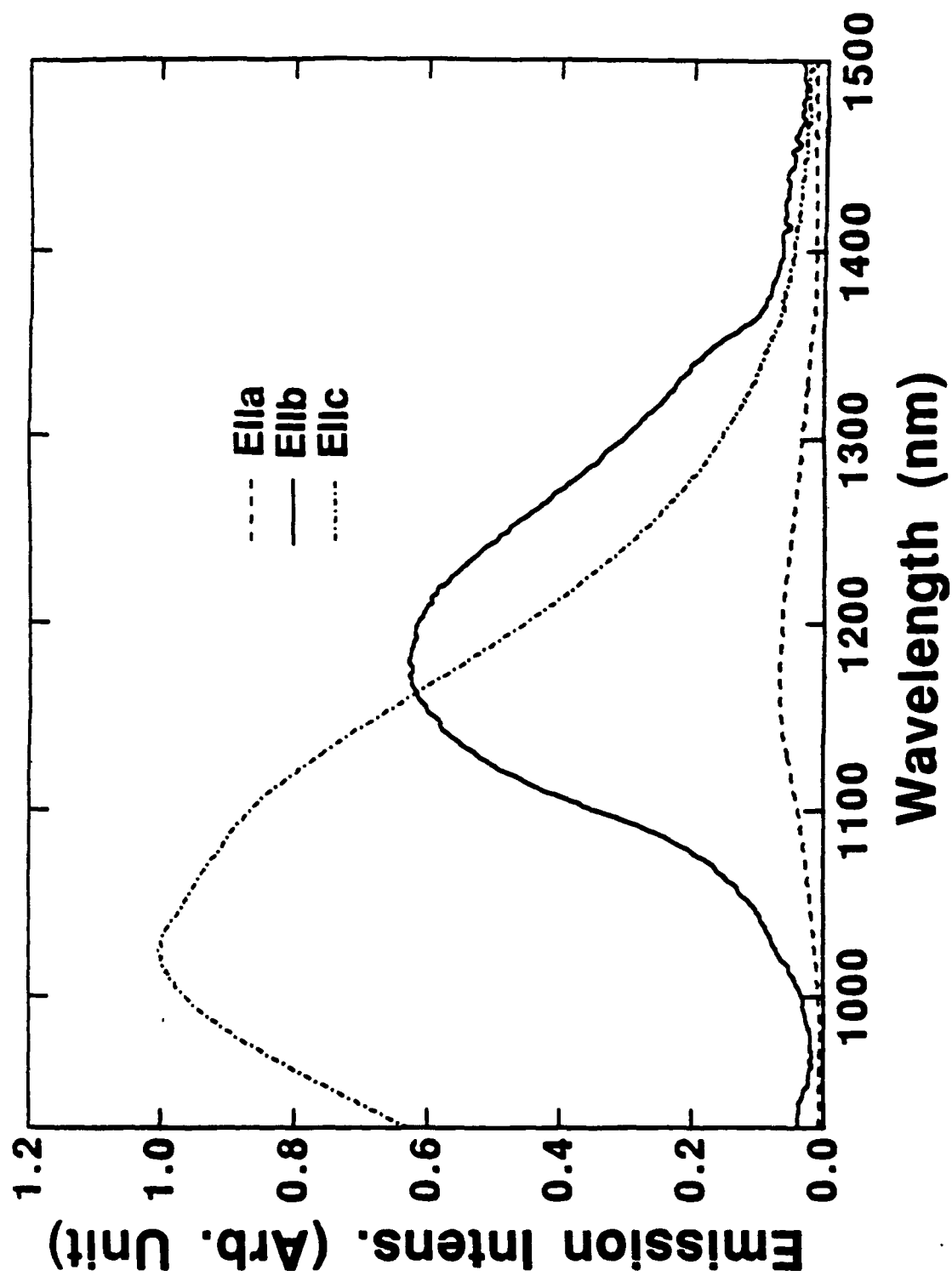


Fig. 4.7 Room temperature polarized emission spectra of Cr:Mg₂SiO₄.

emission longer than 1100nm, the fluorescence decay is exponential with a lifetime $2.7\mu\text{s}$ at room temperature. But for the emission below 1100nm, a double exponential decay was observed indicating that two kinds of emission centers exist. The additional emission center is attributed to Cr^{3+} in $\text{Mg}(\text{C}_5)$ site.⁷ The decay curve at 1200nm is shown in Fig. 4.8.

There is little doubt that the near-infrared emission with a lifetime $2.7\mu\text{s}$ and near-infrared absorption belong to the same electronic transition, especially after we compare the low temperature emission and absorption spectra in the NIR region. They show an almost perfect mirror image with the pure electronic transition located at 1090nm as shown in Fig. 4.9. The strong phonon assisted transition peaks in the emission spectra show that at least two different low frequency phonons with energy $\sim 150\text{ cm}^{-1}$ and 490 cm^{-1} are involved, although the exact assignment is not very clear.^{6,13}

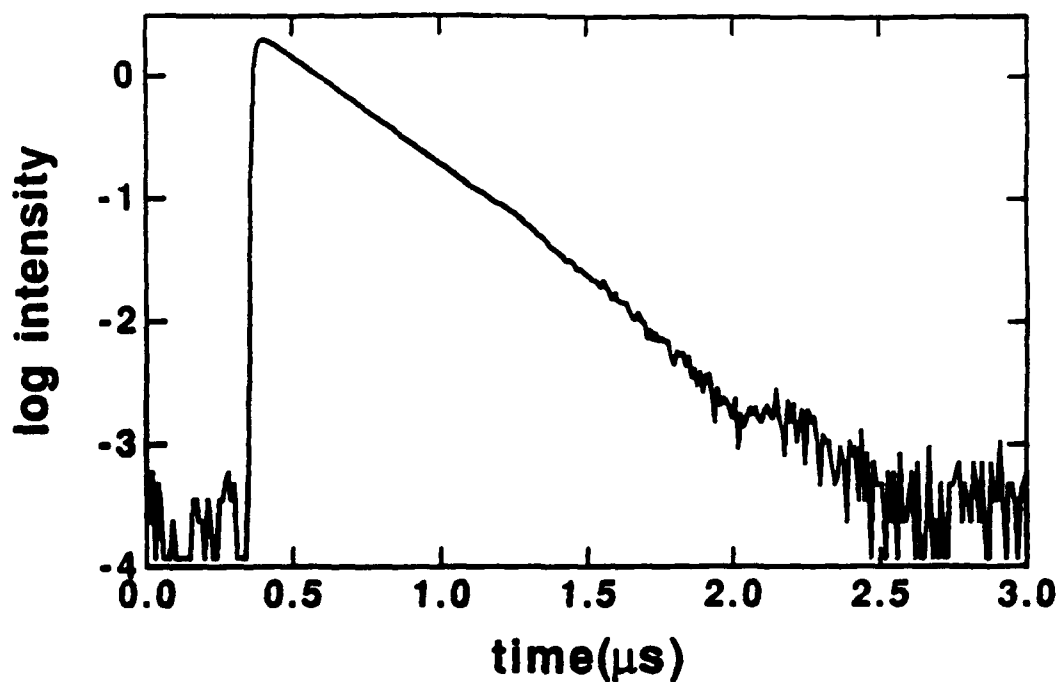


Fig. 4.8 $\text{Cr:Mg}_2\text{SiO}_4$ room temperature fluorescence decay at 1200nm.

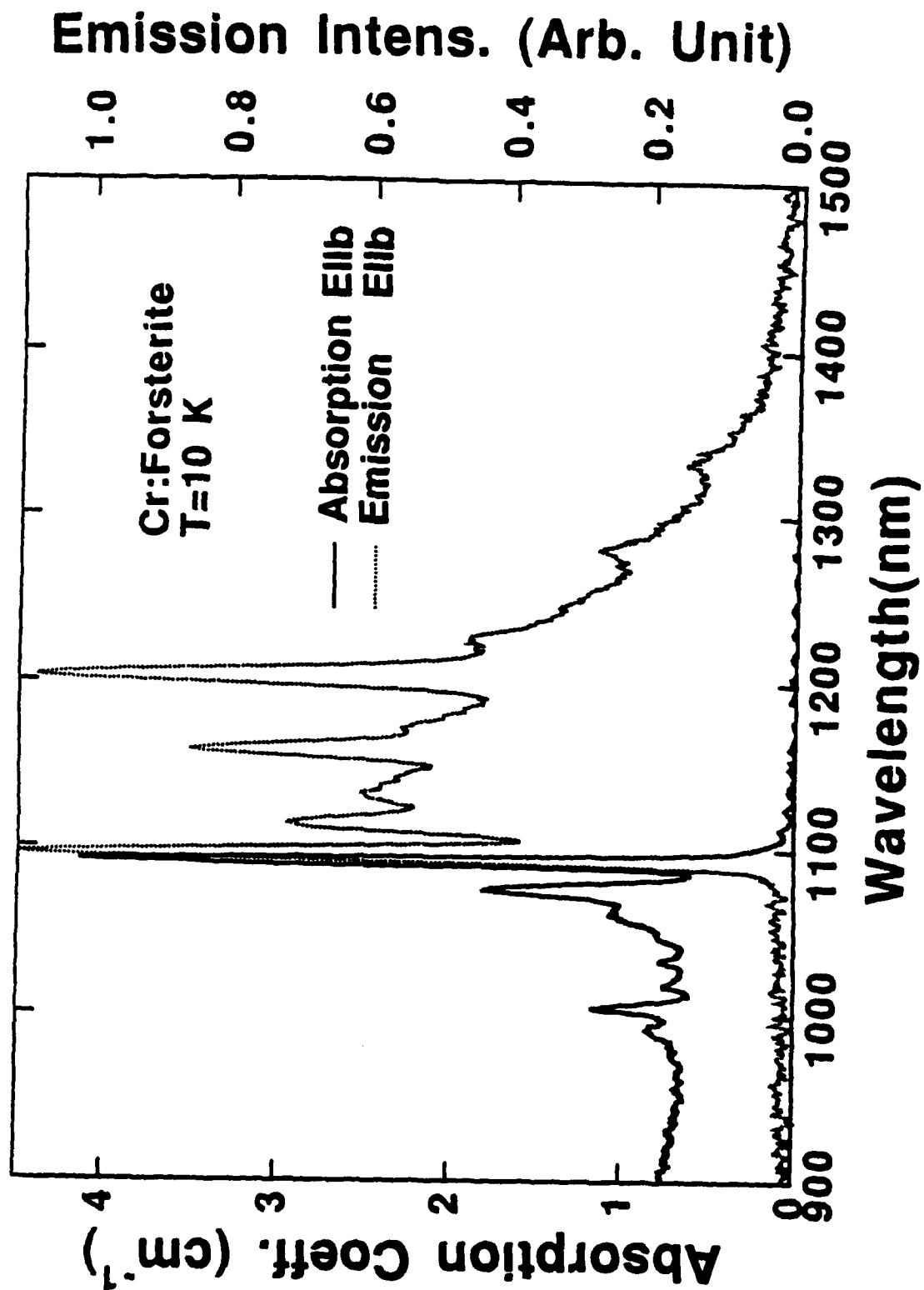


Fig. 4.9 Near infrared E//b absorption and emission of Cr:forsterite at liquid helium temperature.

4.2.2 Cr:Ca₂MgSi₂O₇

The room temperature polarized absorption of 0.25%Cr:Ca₂MgSi₂O₇ is shown in Fig. 4.10. Since Ca₂MgSi₂O₇ has tetragonal symmetry (compared to orthorhombic symmetry of forsterite), only the E//c and E⊥c spectra are distinct. When compared to the spectra of forsterite, we can immediately identify the similar absorption peaks at 579nm, 660 nm and 767nm and also the weaker absorption bands in the NIR region.

But the absorption bands around 440 and 660nm which we attribute to Cr³⁺ in octahedral sites are absent in Cr:Ca₂MgSi₂O₇ crystal. This result is consistent with the crystal structure of Ca₂MgSi₂O₇, because as stated in Section 2.1, Ca₂MgSi₂O₇ does not have any octahedral sites and also Cr⁴⁺ ions should enter the Si sites where is no need for any charge compensation.

The 10K absorption spectra are shown in Fig. 4.11. Based on the spectra and the same calculation procedure as in the last section, the cubic field parameters can be obtained by using the formula in Appendix to be $Dq = -996\text{cm}^{-1}$, $B = 546.5\text{cm}^{-1}$, and C was assigned to $4.4B$. The calculated and observed spectra are shown in Fig. 4.12. Although the detailed splitting can not be determined by this procedure, the energy diagrams reasonably describe the general characteristics of Cr⁴⁺ in the Si site of Ca₂MgSi₂O₇.

The low temperature absorption spectra do not show any structure at all either in the visible or NIR frequency region except an additional peak at 555nm(18050cm^{-1}). This should be a phonon replica for the peak at 579(17270cm^{-1}), showing the phonon energy 780cm^{-1} .

Two other samples with concentration 1 and 0.1 mole percent with respect to the Si were also examined. All samples have the same spectral characteristics.

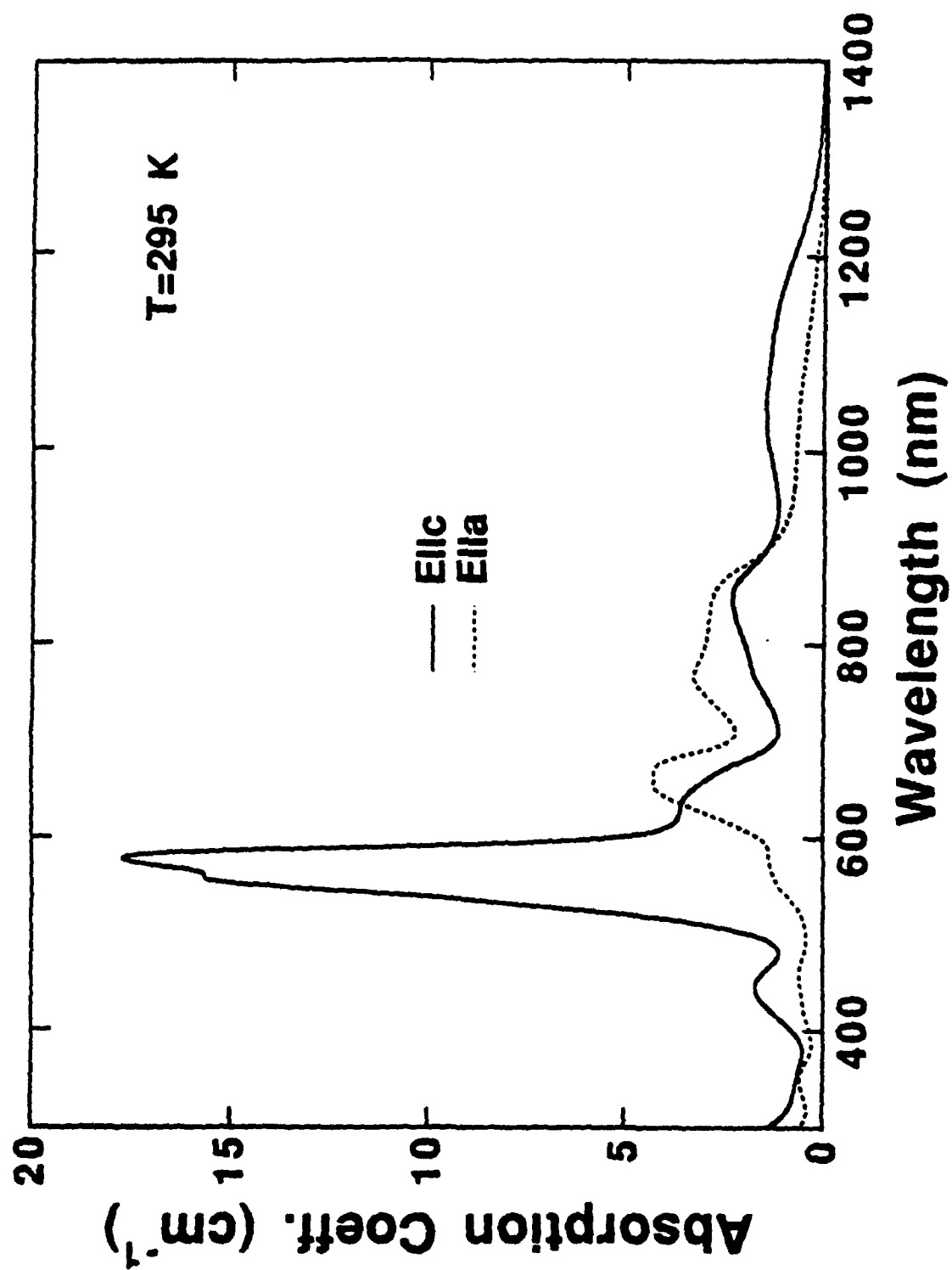


Fig. 4.10 Room temperature polarized absorption spectra of $\text{Cr:Ca}_2\text{MgSi}_2\text{O}_7$.

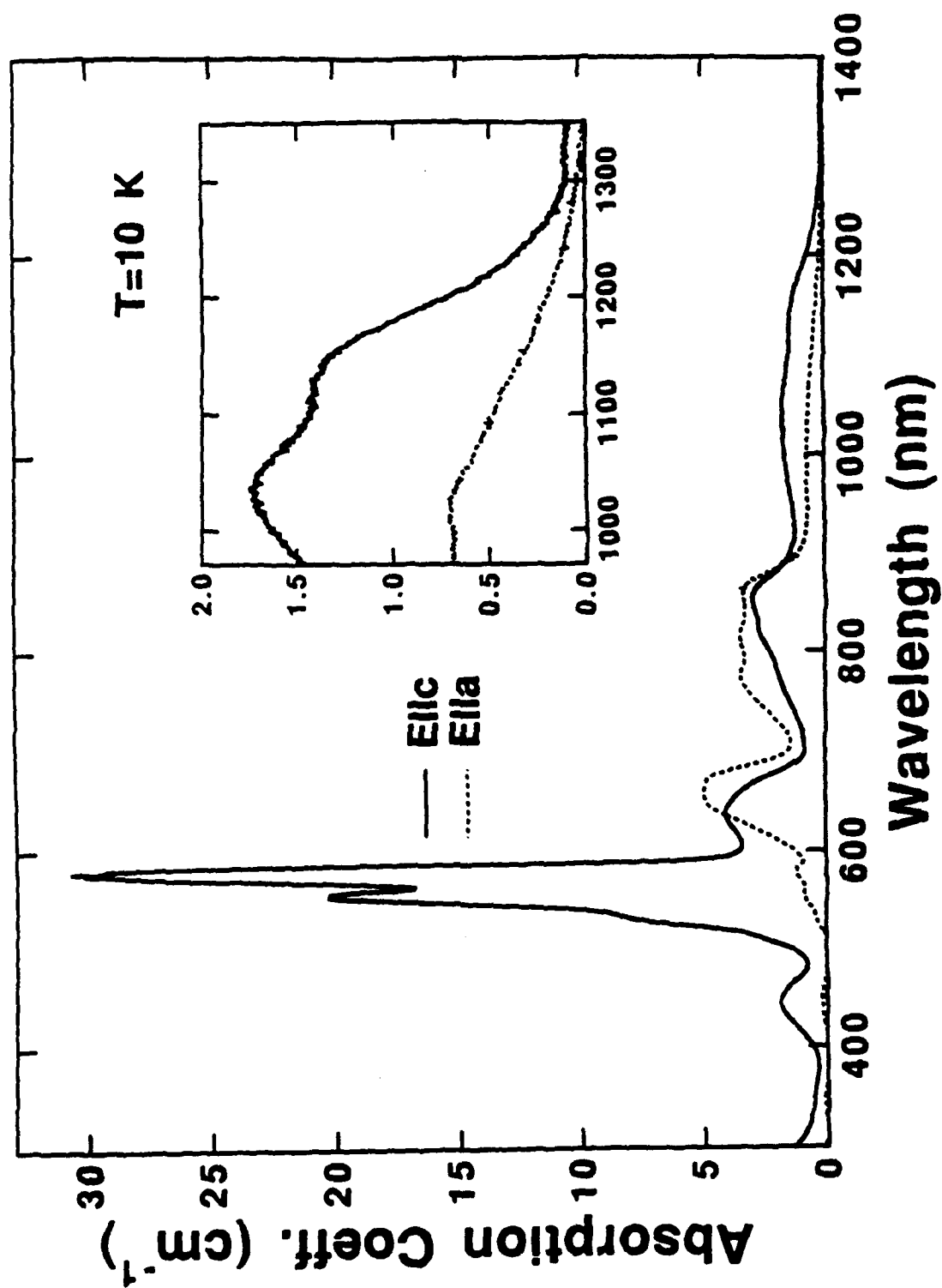


Fig. 4.11 10K polarized absorption spectra of Cr:Ca₂MgSi₂O₇.

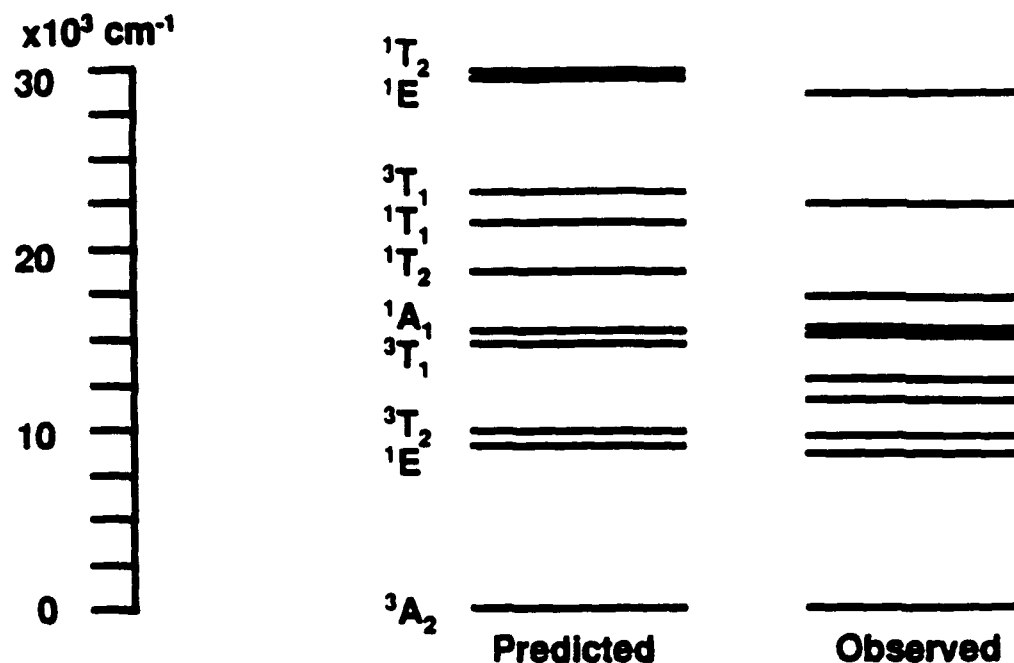


Fig. 4.12 Calculated and observed energy levels of Cr⁴⁺ ions in Ca₂MgSi₂O₇.

The effort of finding emission from Cr:Ca₂MgSi₂O₇ was unsuccessful. The crystal was pumped along the a axis with sample length 0.715cm by using an Ar⁺ laser at 488nm. Several other pumping sources such as a dye laser at 650nm (with Rhodamine 6G dye) and a Ti:Sapphire Laser ranging from 700-850nm were also used. Still no emission was detected. The measurement was attempted at liquid nitrogen/helium temperature but no signal was detected. Based on the sensitivity of the spectrometer, the Cr:Ca₂MgSi₂O₇ emission intensity must be at least a factor of 100 less than that of Cr:forsterite.

In order to check the possible influence of a valency change in the Ca₂MgSi₂O₇ crystals on the spectra, I attempted to reduce the crystals by annealing in an atmosphere with an oxygen partial pressure of 10⁻¹⁷ atm at 750°C for 36 Hours. The room

temperature absorption remained the same and emission was still absent (indicating low oxygen diffusion). Lower oxygen partial pressures were obtained with forming gas (95% N₂ and 5% H₂) and the samples were heated to 1000°C for 24 hours and then quenched. After reduction, the absorption of Cr:Ca₂MgSi₂O₇ was smaller by ~25% throughout the spectra indicating that some Cr⁴⁺ may have reduced to Cr³⁺. But no new features appeared, which needs to be investigated further. This Cr⁴⁺ absorption variations with annealing atmospheres are similar to Cr⁴⁺ in forsterite. After annealing, Cr³⁺ ions in forsterite may further reduced to Cr²⁺ to give extra absorption bands as observed.¹⁴

4.2.3 Cr:Ba₂MgGe₂O₇

Fig. 4.13 shows the polarized absorption spectra obtained for 0.5%Cr:Ba₂MgGe₂O₇. Their spectral shape is similar to that of Cr:Ca₂MgSi₂O₇ and Cr:forsterite, although red-shifted several tens of nm. The spectra consist of rather large peaks at 636, 728 and 832nm and a weaker NIR absorption.

When the absorption spectra was measured at liquid helium temperature as shown in Fig. 4.14, several structures showed up. In the NIR region, I observed the zero phonon line with a small triplet splitting at 1282.8nm, 1286.5 and 1287.1nm, possibly due to the spin-orbit interaction. The corresponding phonon sideband shows that at least one phonon energy of 107cm⁻¹ is involved. The same characteristics also appear in the peaks due to the assigned transition ³A₂->³T₁ of Cr⁴⁺ in the Ge site. The average phonon energies were found to be 644cm⁻¹ and 228cm⁻¹ for the transitions with energies 15723cm⁻¹ and 13736cm⁻¹.

With the assumption of linear coupling between electronic states and lattice vibrations, we can use the quantum-mechanical Franck-Condon Principle to calculate the intensities of the zero

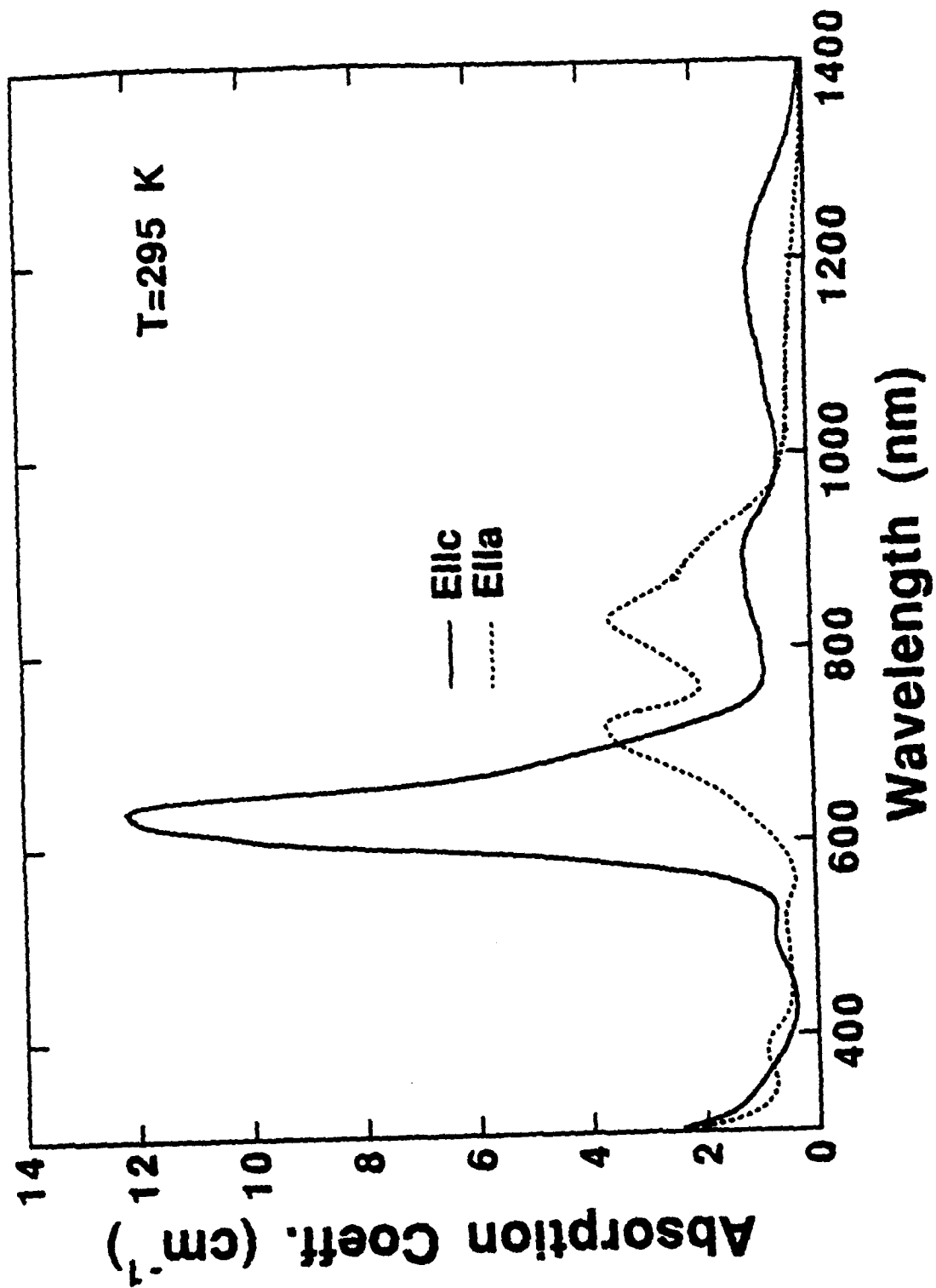


Fig. 4.13 Room temperature polarized absorption spectra of Cr:Ba₂MgGe₂O₇.

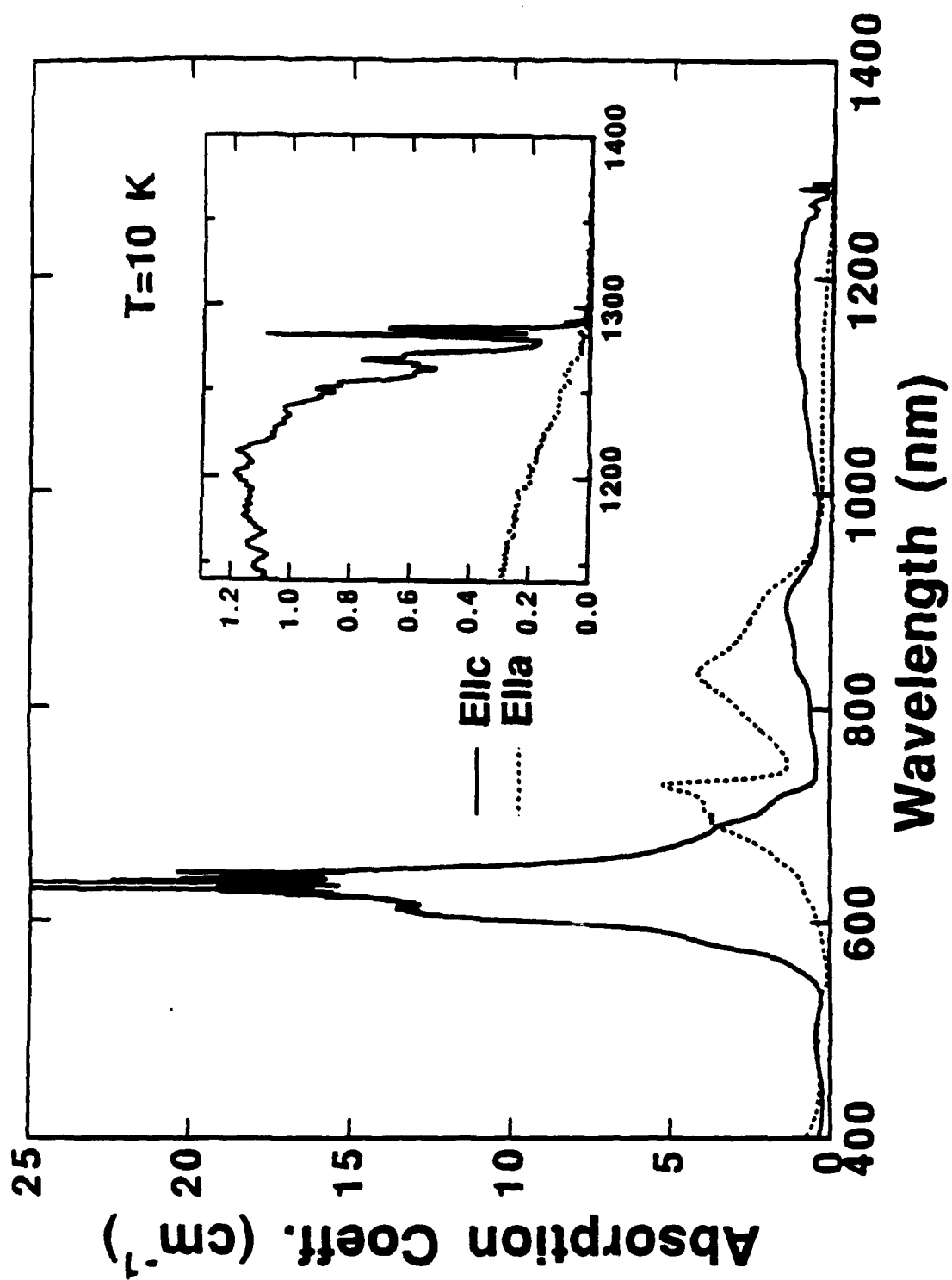


Fig. 4.14 10K polarized absorption spectra of Cr:Ba₂MgGe₂O₇.

phonon line and vibronic transitions.^{15,16,17} According to the Huang-Rhys calculation, the relative integrated intensity of zero phonon line at $T=0$ is expressed by the Huang-Rhys factor S_0

$$(I_{tot}/I_{zpl})_{T=0} = \exp(S_0) \quad (4.1)$$

where, I_{zpl} and I_{tot} are the corresponding integral intensities of zero phonon line and phonon sideband, and $S_0 = \sum_s P_s / \hbar \omega_s$ is the sum of Stokes losses expressed in phonon numbers; P_s is the Stokes shift in energy for the s -th mode; $2P_s = m_s \omega_s^2 q_{s0}^2$, where m_s is mass, ω_s is the frequency and q_{s0} is the shift of the equilibrium position for the oscillator.

As the temperature is raised, the relative integrated intensity of zero phonon line is

$$(I_{tot}/I_{zpl})_T = \exp(S_T) = \exp(\sum_s P_s \coth(\hbar \omega_s / 2kT) / \hbar \omega_s) \quad (4.2)$$

By using the above formula, $(I_{tot}/I_{zpl})_{T=10K}$ for the transition near 1287nm was found to be 58.285. This value corresponds to $S(T=10K) \approx 4$. This big S shows the large Stokes loss between 3A_2 and 3T_2 states. The Huang-Rhys factor of the $^3A_2 \rightarrow ^3T_1$ transition at 636nm was found to be 1.7 at 10K.

By using the low temperature absorption data, the cubic-field approximation parameters are readily obtained by solving the eigenenergy equations in Appendix to be:

$$Dq = -914.5 \text{ cm}^{-1}, B = 498 \text{ cm}^{-1}, C = 4.4B$$

The calculated and observed energy levels are shown in Fig. 4.15. The agreement is reasonably good.

No emission was found in $\text{Cr:Ca}_2\text{MgSi}_2\text{O}_7$ at either room temperature nor liquid helium temperature. Based on the

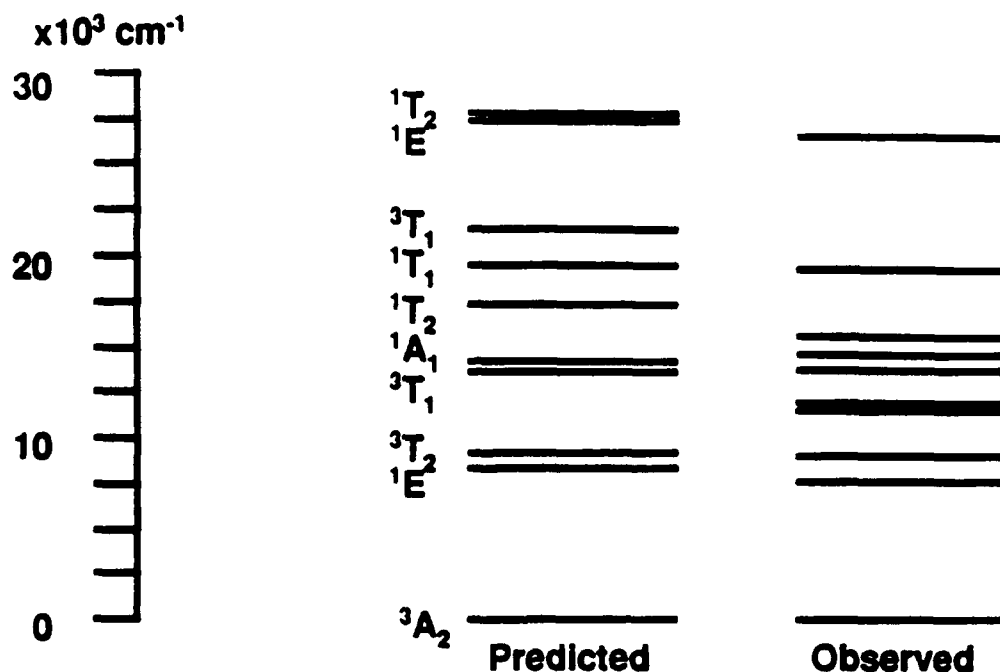


Fig. 4.15 Calculated and observed energy levels of Cr^{4+} ions in $\text{Ba}_2\text{MgGe}_2\text{O}_7$.

sensitivity of the spectrometer, the $\text{Cr}:\text{Ca}_2\text{MgSi}_2\text{O}_7$ emission intensity must be at least a factor of 100 less than that of $\text{Cr}:\text{forsterite}$

4.2.4 Comparison

Here, some results are summarized from section 4.2.1-4.2.3. First, Table 4.1 shows the absorption peaks of three Cr doped crystals.

We notice that all the peaks fall in the same frequency region especially for $\text{Cr}:\text{forsterite}$ and $\text{Cr}:\text{Ca}_2\text{MgSi}_2\text{O}_7$. The

Table 4.1 Absorption peaks of three Cr-doped crystals.

Crystals	Absorption Peaks (nm)
Cr:Mg ₂ SiO ₄	571, 662, 740
Cr:Ca ₂ MgSi ₂ O ₇	579, 660, 767
Cr:Ba ₂ MgGe ₂ O ₇	636, 728, 832

absorption peaks of Cr:Ba₂MgGe₂O₇ are red-shifted relative to the other two crystals. This is due to the smaller energy splitting resulting from the smaller crystal field strength of the larger Ge tetrahedral site of Ba₂MgGe₂O₇. These absorption characteristics must come from having similar species in nearly identical local environments in these crystals. Comparing the crystal structure of forsterite with åkermanite, the only similarity is the Si(Ge) tetrahedral site with symmetry C_s. Also, in the åkermanite crystals, there are no chromium charge compensating species; thus, only Cr⁴⁺ can substitute for the Si⁴⁺ or Ge⁴⁺ sites. Therefore, the assumption that tetrahedrally coordinated Cr⁴⁺ ions are in all three crystals, Mg₂SiO₄:Cr, Ba₂MgGe₂O₇:Cr and Ca₂MgSi₂O₇:Cr is consistent with the room temperature absorption data.

However, considerable differences in the low temperature NIR absorption spectra exist. First, zero-phonon lines are absent in Cr:Ca₂MgSi₂O₇ for the transition ³A₂->³T₂. Second, although zero-phonon lines were observed both in the Cr:Ba₂MgGe₂O₇(1287nm) and Cr:forsterite(1090nm), they occur in different polarizations since the c-axis of åkermanite corresponds to a-axis of forsterite when considering the orientation for the tetrahedra (referring Fig. 2.4). The Cr:forsterite's relative absorption of the zero-phonon line to the vibronics is considerable larger than that of Cr:Ba₂MgGe₂O₇. And most important of all, no emission has been found from either chromium doped åkermanite crystals.

These results did not prove that the transition of Cr^{4+} ions in the Si site of forsterite is the mechanism for the NIR laser action of Cr:forsterite. However, the excitation spectra of Cr:Mg₂SiO₄ at 20 K while monitoring emission in the NIR region traced almost exactly the large absorption peaks in the visible region. But the chances are that even at 20K, the energy transfer between species is not diminished. Then, another evidence by Ref. 14 shows that the absorption coefficients in the NIR and visible region have the same increasing/decreasing trends when the forsterite crystal was annealed or oxidized. This can definitely relate the two spectral regions, or at the very least, we can say that the laser transition of forsterite is related to Cr^{4+} .

Let us compare crystal structures between forsterite and åkermanite. The local environments are so similar in that they both have the C_s symmetry and a Si-O average bond length 1.63Å. But we must also consider the whole structures of the crystals because the d electron wavefunctions have strong interaction with the lattice vibrations. In considering the whole crystal structures, forsterite and åkermanite have some differences.

We can use the simple configuration coordinate model to compare the electron-lattice coupling of the three crystals.

By using Eqs. 4.1 and 4.2, the corresponding Huang-Rhys factors for Cr:forsterite and Cr:Ca₂MgSi₂O₇ can be obtained. For Cr:forsterite, the NIR transition at 1.1µm has $I_{zp1}/I_{tot}=0.2927$ and $S=1.2286$ at 10K as compared to Cr:Ba₂MgGe₂O₇ ($S=4$) and Cr:Ca₂MgSi₂O₇ (~several tens) of some transitions. So for Cr:Ba₂MgGe₂O₇ Cr:Ca₂MgSi₂O₇, the coupling is strong ($S \gg 1$)¹⁵ and the equilibrium position shift (Stokes shift) between ground state and excited state is large. As shown in Fig. 4.16(a), when the Stokes shift is large, the overlapping of the phonon wavefunctions between the ground and excited state is small, as is the zero-phonon line intensity.

If the Stokes shift is so large that one branch of the ground state potential energy parabola intersects the excited state potential parabola, this intersection will allow a non-radiative relaxation path shown in Fig. 4.16(b). Therefore, non-radiative relaxation will dominate and no radiative relaxation can be detected. This may be the reason why Cr:Ca₂MgSi₂O₇ and Cr:Ba₂MgGe₂O₇ have none or very weak emission.

4.3 Results and Analysis of EPR Spectroscopy

4.3.1 Cr:Åkermanite(Ba₂MgGe₂O₇)²

In EPR spectroscopy, 0.5% and 0.01% chromium doped Ba₂MgGe₂O₇ were examined. Three different signals were detected. Two of those signals which do not scale according to the chromium concentration are from Mn²⁺ and Fe³⁺ impurities.

The one that scaled according to the Cr concentration must be due to chromium ions. With the magnetic field in an arbitrary direction, we can observe four EPR signals corresponding to four crystallographically equivalent magnetic sites. These four sites are shown in Fig. 4.17.

When magnetic field points to a specific direction, some of these sites will become magnetically equivalent in a manner that indicates the incorporation of this species at the crystallographic 4e sites of Ba₂MgGe₂O₇. Both barium and germanium lie at 4e sites. But due to the large disparity of barium and chromium ionic radii(0.44Å vs 1.42Å), it is unlikely that chromium ions incorporate into Ba site. So it is inferred that chromium ions occupy the Ge's tetrahedral sites.

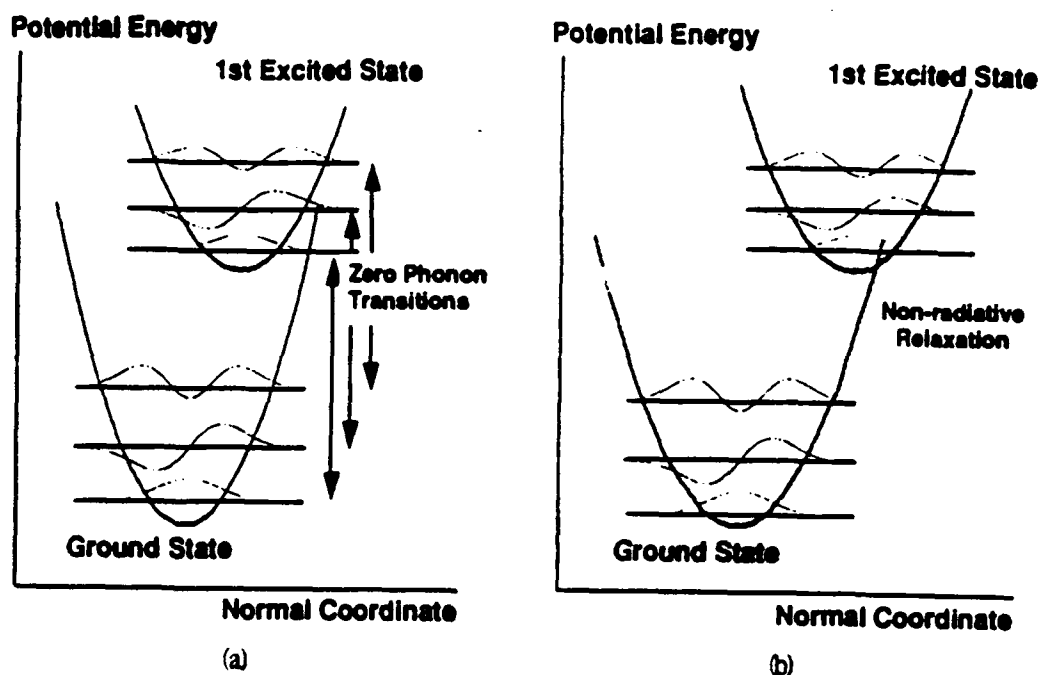


Fig. 4.16 (a) Configuration-coordinate diagram showing the zero-phonon line transition. (b) Configuration-coordinate diagram for non-radiative processes.

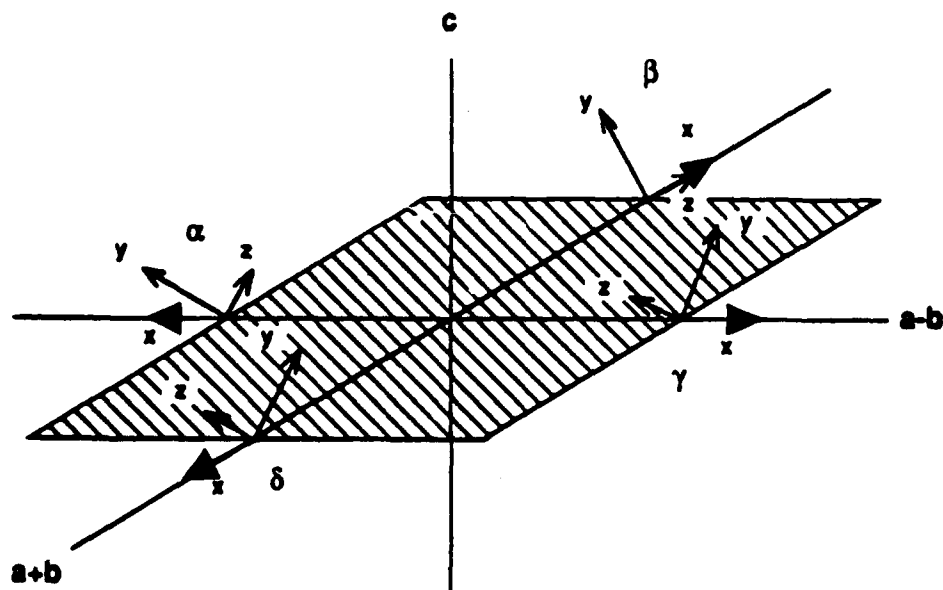


Fig. 4.17 $\text{Ba}_2\text{MgGe}_2\text{O}_7$ $\overline{P}42_1m$ space group symmetry.

The field for resonance curve which is plotted along several directions is shown in Fig. 4.18. This spectral feature is attributed to Cr^{4+} in Ge site.

Only one of three possible microwave transitions was detected indicating large zero-field splitting. The observed transition is the one from the $S_z=-1$ state to the $S_z=1$ state from Fig. 3. 3. The angular variation of the field for resonance curve was well described by the usual spin-hamiltonian for a spin one system described in Section 3.3.1.

$$\mathcal{H} = \beta \mathbf{H} \cdot \mathbf{g} \cdot \mathbf{S} + D[S_z^2 - 1/3 S^2] + E(S_x^2 - S_y^2) \quad (4.3)$$

In Section 3.3.1, the above formula is used for a tetragonal crystal, but it can also be applied to any crystal with lower symmetry (in this case, C_s symmetry for Cr^{4+} in the Si(Ge) sites of forsterite and åkermanite), because we can always diagonalize the spin-hamiltonian by eliminating the $S_x S_y + S_y S_x$, $S_x S_z + S_z S_x$ and $S_y S_z + S_z S_y$ terms. After diagonalization, the axes of the spin-hamiltonian may not be parallel with the crystal axes. For C_s symmetry, the only symmetry operation is a mirror plane. One of the spin-matrix axes must be perpendicular to the mirror plane, and the other two lie on the mirror plane with unknown orientations.

After fitting the spectra to spin hamiltonian Eqs. 4.1 with the least square method, the fine structure parameters values are (standard deviations in parentheses):

$$|D| = 1.1 \times 10^2 (0.3 \times 10^2) \text{ GHz}, \quad |E| = 4.1 (0.1) \text{ GHz}$$

The dominant fine-structure axis (z axis) lies in the mirror plane ($a \pm b$ plane) and makes an angle of approximate $\pi/3$ with the crystallographic c axis, while the minor (x axis) is normal to the mirror plane.

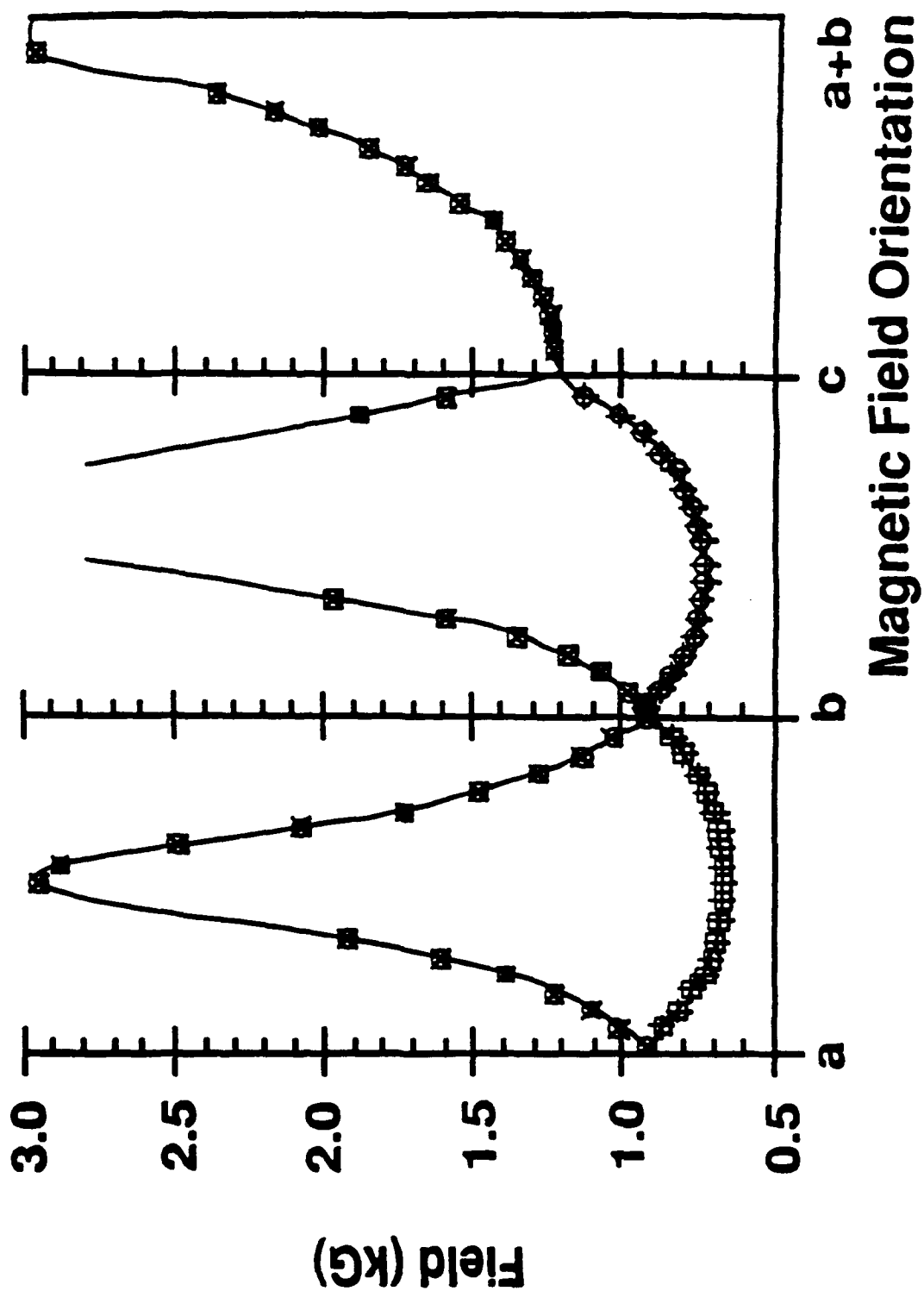


Fig. 4.18 Angular dependence of resonant EPR field in Cr-doped $\text{Ba}_2\text{MgGe}_2\text{O}_7$. (After Ref. 18)

4.3.2 Cr:Forsterite¹⁸

The EPR spectra of Cr:forsterite are more complex than Cr:Ba₂MgGe₂O₇ due to the fact that charge compensated chromium ions of various valences as well as other impurities are present in Cr:forsterite. The dominant signal which is due to Cr³⁺ in Mg site is readily identified¹⁹. With the assistance of the known Cr:Ba₂MgGe₂O₇ system, one signal very similar to the Cr⁴⁺ center in Ba₂MgGe₂O₇ was detected. The field for resonance as a function of magnetic orientation is shown in Fig. 4.19. This signal pattern is consistent with the 4c site in forsterite and is thus consistent with Cr⁴⁺ substitution for silicon (referring the Table 2.1).

After fitting to Eqs. 4.3, the fine structure parameters are obtained:

$$|D|=61(1)\text{GHz and } |E|=4.588(0.003)\text{GHz}$$

The dominant axis (z) lies in the mirror plane and makes an angle of $\pi/4$ with crystallographic a axis and the y axis is normal to the mirror plane.

4.3.3 Comparison

From EPR spectra, Cr⁴⁺ ions in tetrahedral sites are identified in both Cr:Ba₂MgGe₂O₇ and Cr:forsterite. These results are consistent with the results obtained from the optical methods.

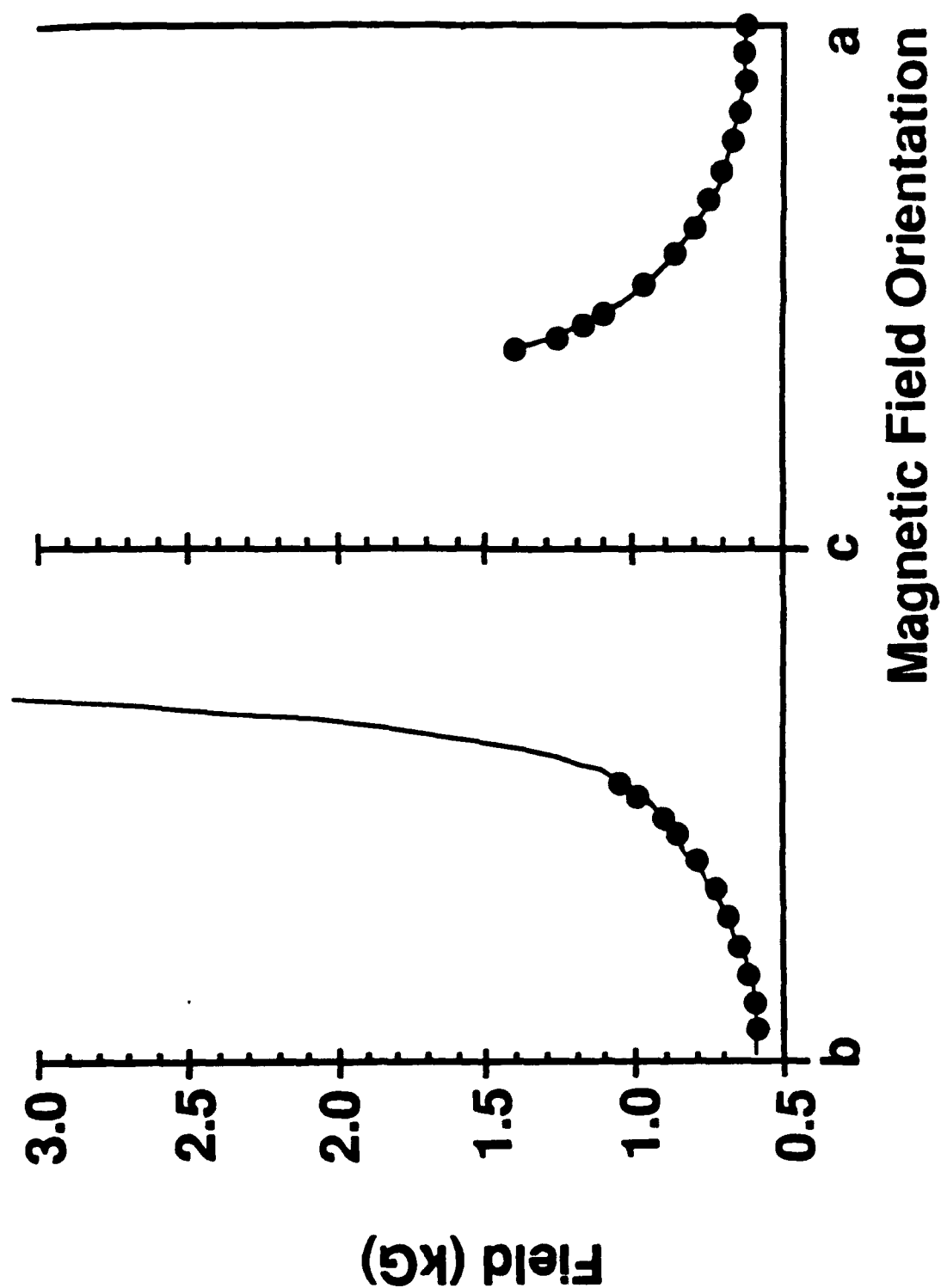


Fig. 4.19 Angular dependence of resonant EPR field in Cr-doped forsterite. (After Ref. 18)

References

- 1 S. A. Al'tshuler, B. M. Kozyrev, "Electron Paramagnetic Resonance in Compounds of Transition Elements", John Wiley and Sons Inc., New York, 1974.
- 2 David J. Singel, "Optical and Magnetic Resonance Investigations of 3d Ions in Single Crystal Hosts: Candidates for Tunable Solid-State Lasers," U.S. Army Research Office, DAAL03-90-01113, Feb. 1991.
- 3 H. M. Assenheim, "Introduction to Electron Spin Resonance," Plenum Press, New York, 1966.
- 4 J. E. Wertz and J. R. Bolton, "Electron Spin Resonance: Elementary Theory and Practical Applications," Chapman and Hall, New York, 1986.
- 5 V. Petricevic, S. K. Gayen, R. R. Alfano, "Chromium-activated Forsterite Laser," OSA Proceedings on Tunable Solid State Laser, V5, p77, 1989.
- 6 H. R. Verdun, L. M. Thomas, and D. M. Andrauskas, "Laser Performance of Chromium-Aluminum Doped Forsterite," OSA Proceedings on Tunable Solid State Laser, V5, p85, 1989.
- 7 V. G. Baryshevski, M. V. Korzhik, M. G. Livshitz, A. A. Tarasov, A. E. Kimaev, I. I. Mishel, M. L. Meilman, B. J. Minkov, A. P. Shkadarevich, "Properties of Forsterite and the Performance of Forsterite Lasers with Lasers and Flashlamp Pumping," OSA Proceeding on Advanced Solid State Laser Conference 91, to be published.
- 8 R. Moncorgé, D. J. Simkin, G. Cormier and J. A. Capobianco, "Spectroscopic Properties and Fluorescence Dynamics in Chromium Doped Forsterite," OSA Proceedings on Tunable Solid State Laser, V5, p93, 1989.
- 9 S. Sugano, Y. Tanabe and H. Kamimura, "Multiplets of Transition-Metal Ions in Crystals," Academic Press, 1970.

- 10 J. Otsuka, "Electrostatic Interaction of d^n Systems in Tetragonal Fields," J. of Phys. Soc. of Japan, V21(4), p596, 1966.
- 11 J. Ferguson, H. J. Guggenheim, H. Kamimura, and Y. Tanabe, "Electronic Structure of Ni^{2+} in MgF_2 and ZnF_2 ," J. of Chemical Physics, V42(2), p775, 1965.
- 12 K. Fujino, S. Sasaki, Y. Takeuchi and R. Sadanaga, "X-ray Determination of Electron Distributions in Forsterite, Fayalite and Tephroite," Acta, Cryst., B7, p513, 1981.
- 13 R. Moncorgé, G. Cormier, D. J. Simkin, and J. A. Capobianco, "Fluorescence Analysis of Chromium-Doped Forsterite (Mg_2SiO_4)," IEEE J. Quantum Electron., QE-27, p114, 1991.
- 14 Y. Yamaguchi, K. Yamagishi, A. Sugimoto and Y. Noke, "The Optical Properties and Crystal Growth Atmosphere of Forsterite," Technical Digest of Advanced Solid State Laser Conference 1991, MB4, p26.
- 15 K. K. Rebane, "Impurity Spectra of Solids," Plenum Press, New York, 1970.
- 16 O. Sild, K. Haller(Eds), "Zero-Phonon Line and Spectral Hole Burning in Spectroscopy and Photochemistry," Springer-Verlag, Berlin, 1988.
- 17 A. M. Stoneham, "Theory of Defects in Solids," Oxford Univ. Press, London, 1975.
- 18 M. H. Garrett, V. H. Chan, H. P. Jenssen, M. H. Whitmore, A. Sacra, D. J. Singel and D. J. Simkin, "Comparison of Chromium-Doped Forsterite and Åkermanite Laser Host Crystals," OSA Proceeding on Advanced Solid State Laser Conference 91, to be published.
- 19 H. Rager, "Electron Spin Resonance of Trivalent Chromium in Forsterite Mg_2SiO_4 ," Phys and Chem. Minerals, V1, p371, 1977.

Chapter 5

Final Discussions

5.1 Summary

(1) Czochralski growth of chromium doped $\text{Ca}_2\text{MgSi}_2\text{O}_7$ and $\text{Ba}_2\text{MgGe}_2\text{O}_7$ were developed. Crystals were grown either by rf induction heated or resistance heated furnaces. The different aspects of three furnaces were explored.

(2) Chromium doped åkermanites ($\text{Ca}_2\text{MgSi}_2\text{O}_7$ and $\text{Ba}_2\text{MgGe}_2\text{O}_7$) were grown to assist the identification of the impurity centers in chromium doped forsterite crystals. Large absorption peaks in the visible frequency regions are easily identified in all the samples. This similarity and the unique environment of the åkermanite crystals which allow only Cr^{4+} going into the Si(Ge) site confirm the assumption of Cr^{4+} ions in forsterite.

(3) Electron paramagnetic resonance spectroscopy directly measure the ground state splitting and site symmetry of the impurity centers. The results are consistent with the assumption of Cr^{4+} substituting for the Si(Ge) tetrahedral sites.

(4) From both optical and magnetic resonance methods, only Cr^{4+} ions in the silicon(germanium) tetrahedral sites have been found in chromium doped åkermanite. Chromium ions in forsterite not only occupy the $\text{Mg}(\text{C}_i)$ and $\text{Mg}(\text{C}_s)$ octahedral sites, but also substitute for the silicon tetrahedral sites.

(5) There exist considerable differences between the low temperature absorption spectra of Cr:forsterite and Cr:åkermanite. Additionally no emission was detected in the chromium doped åkermanite samples. This leads us to the conclusion that the placement of Cr^{4+} in tetrahedral sites does not guarantee a laser transition in the near-infrared region.

(6) A possible explanation why Cr:åkermanite do not have emission is given, although other possibilities are not ruled out. For example, the coupling between Cr^{3+} and Cr^{4+} or interaction between charge compensation ions are also possible. But at least, the laser action in Cr:forsterite is Cr^{4+} related.

5.2 Survey of d^2 Configuration in Tetrahedral Sites

During the period of this work, several other potential solid state laser materials using the d^2 configuration in tetrahedral sites were developed. Those materials, along with Cr:forsterite and Cr:åkermanite are discussed in the following paragraphs:

(1) Cr: Mg_2SiO_4 : Cr:forsterite have both Cr^{3+} in octahedral sites and Cr^{4+} in tetrahedral sites. Cr^{2+} ions may also substitute for Mg^{2+} . Laser tuning ranges from 1170nm to 1330nm. Both continuous and pulse operations have been demonstrated. Mode-locked and Q-switched lasing mode have also been achieved.

(2) Cr doped melilite group: several crystals tested include the åkermanites ($\text{Ca}_2\text{MgSi}_2\text{O}_7$, $\text{Ba}_2\text{MgGe}_2\text{O}_7$) used in this study, gehlenite ($\text{Ca}_2\text{Al}_2\text{SiO}_7$, $\text{Ca}_2\text{Ga}_2\text{SiO}_7$)³, and mixed systems ($\text{Ca}_2(\text{Mg}_x\text{Al}_y\text{Si}_{1-x-y})_3\text{O}_7$). Gehlenites have the same structure as åkermanites with aluminum replacing magnesium and half of the silicon atoms. It was found that the intensity of luminescence of chromium ions in the near IR-region significantly decreased with the change of host composition from aluminium

content melilite to magnesium-content melilite.³ Although the emission spectra observed in Cr:gehlenite are likely due to Cr^{4+} ions, an emission band extending below 1000nm (in Cr: $\text{Ca}_2\text{Ga}_2\text{SiO}_7$) and a nonexponential fluorescence decay (in both Cr: $\text{Ca}_2\text{Al}_2\text{SiO}_7$ and Cr: $\text{Ca}_2\text{Ga}_2\text{SiO}_7$) can not be explained by solely Cr^{4+} ions in tetrahedral sites. No laser action has been reported yet.

(3) Chromium doped garnets^{3,4,5,6,7,8,9}: garnet crystals have space group symmetry $\text{Ia}\bar{3}\text{d}$. When chromium ions were doped into garnets, they are likely to enter into both octahedral and tetrahedral sites. Tetrahedral sites in garnets have the S_4 cubic symmetry which is reflected in the absorption spectra. The same characteristic $^3\text{A}_2 \rightarrow ^3\text{T}_1$ absorption peaks are also found in the absorption spectra. Chromium doped yttrium aluminum garnet (YAG) have been demonstrated to lase between $1.3\mu\text{m}$ - $1.5\mu\text{m}$. The lack of zero-phonon line is due to the forbidden transition between $^3\text{A}_2$ and $^3\text{T}_2$ levels. The fluorescence decay is exponential with a lifetime of $3.6\mu\text{s}$. Similar emission spectra were also found in Cr: $\text{Gd}_3\text{Sc}_2\text{Ga}_3\text{O}_{12}$ and Cr: $\text{Y}_3\text{Sc}_2\text{Ga}_3\text{O}_{12}$, but none of these were demonstrated to lase, probably due to the excited state absorption $^3\text{T}_2 \rightarrow ^3\text{T}_1$.

(4) Mn^{5+} doped $\text{Sr}_5(\text{PO}_4)_3\text{Cl}$ and $\text{Ca}_2\text{PO}_4\text{Cl}$ ¹⁰: $\text{Sr}_5(\text{PO}_4)_3\text{Cl}$ has space group symmetry $\text{P}6_3/\text{m}$, and $\text{Ca}_2\text{PO}_4\text{Cl}$ symmetry Pbcm . The tetrahedral sites have respectively C_2 and C_s symmetry in $\text{Sr}_5(\text{PO}_4)_3\text{Cl}$ and $\text{Ca}_2\text{PO}_4\text{Cl}$. The Mn^{5+} ion is most likely stabilized in the tetraoxo coordination by isomorphous substitution for the P^{5+} ion, giving MnO_4^{3-} tetrahedra. The room temperature absorption spectra show large peaks which indicates that strong coupling between local vibrations and electronic transitions probably exists. The coupling to the local vibrations would be no surprise because the high valence state (5+) of manganese. Fluorescence decay is double exponential and has much longer lifetimes compared to that of Cr: Mg_2SiO_4 and Cr:YAG.

The similar behavior of probable $\text{Mn}^{5+}(\text{d}^2)$ in tetrahedral sites should give us some confidence about the assumption of laser transition of $\text{Cr}^{4+}(\text{d}^2)$ in tetrahedral sites. However a lot of questions still need to be answered. It seems that emission does occur when there are many different substitutional sites available for chromium. So the possibility of cross interaction can not be ignored.

5.3 Future Research

- (1) A possible experiment by combining optical excitation and electronic paramagnetic resonance can be used to directly measure properties of the excited state of the laser transition at 1.1-1.3 μm .
- (2) Observe the shift of the zero phonon line in the near infrared region when applying external magnetic and electric field. This should give us more information about the site symmetry and the energy levels.
- (3) Grow other kinds of crystals with chromium in tetrahedral sites to study the coupling effect between lattice vibrations and electronic transitions in different environments.

References

- 1 T. H. Allik, B. H. T. Chai, L. D. Merkle, "Crystal Growth and Spectroscopic Analysis of Cr^{4+} -doped Melilite Compounds," Technical Digest of Advanced Solid State Laser Conference 1991, MA5, p14.
- 2 A. L. Denisov, E. V. Zharikov, D. A. Zubenko, M. A. Noginov, V. G. Ostroumov, V. A. Smirnov, M. E. Kholodova, I. A. Shcherbakov, "Growth and Spectroscopic Study of Chromium Doped Melilite Crystals- $\text{Ca}_2(\text{Mg}_x\text{Al}_y\text{Si}_{1-x-y})_3\text{O}_7$," Technical Digest of Advanced Solid State Laser Conference 1991, pdp1.
- 3 W. Jia, B. M. Tissue, L. Lu, K. Hoffman and W. M. Yen, "Near-Infrared Luminescence in Cr, Ca-doped Yttrium Aluminum Garnet," Technical Digest of Advanced Solid State Laser Conference 1991, MB7, p35.
- 4 S. Kuch, K. Petermann, G. Huber, "Spectroscopic Investigation of the Cr^{4+} Center in YAG," Technical Digest of Advanced Solid State Laser Conference 1991, MA4, p11.
- 5 N. B. Angert, N. I. Borodin, V. M. Garmash, V. A. Zhitnyuk, A. G. Okhrimchuk, O. G. Siyuchenko and A. V. Shestakov, "Lasing Due to Impurity Color Centers in Yttrium Aluminum Garnet Crystals at Wavelength in the Range 1.35-1.45 μm ," Sov. J. Quantum Electron., V18(1), p73, 1988.
- 6 L. I. Krutova, N. A. Kulagin, V. A. Sandulenko, and A. V. Sandulenko, "Electronic State and Positions of Chromium Ions in Garnet Crystals," Sov. Phys. Solid State, V31(7), p1193, 1989.
- 7 A. P. Shkadarevich, "Recent Advances in Tunable Solid State Lasers," OSA proceedings on Tunable Solid State Laser, V5, p60, 1989.
- 8 G. M. Zverev, A. V. Shestakov, "Tunable Near-Infrared Oxide Crystal Lasers," OSA proceedings on Tunable Solid State Laser, V5, p66, 1989.

- 9 N. A. Kulagin and V. A. Sandulenko, "Ab Initio Theory of Electronic Spectra of Doped Crystals: Chromium Ions in Oxides," Sov. Phys. Solid State, V31(1), p133, 1989.
- 10 J. A. Capabianco, G. Cormier, H. Manaa, R. Moncorge, P. Galarneau, B. Labranche, "Near Infrared Fluorescence and Gain Measurements of the Mn^{5+} ($3d^2$) ion in $\text{Sr}_5(\text{PO}_4)_3\text{Cl}$ and $\text{Ca}_2\text{PO}_4\text{Cl}$," Technical Digest of Advanced Solid State Laser Conference 1991, pdp2.

Appendix

Matrix Elements and Eigenenergies of d^2 and d^3 configurations

The parameters used in the following sections are defined as followed.

Racah parameters:

$$B = F_2 - 5F_4$$
$$C = 35F_4$$

Slater-Condon parameters:

$$F_2 = F^2/49, F_4 = F^4/441$$
$$F^k(dd) = \int r_1^2 dr_1 \int r_2^2 dr_2 R_d^2(r_1) R_d^2(r_2) r_{<}^k / r_{>}^{k+1}$$

where $r_{<}$ is the lesser and $r_{>}$ is the greater of r_1 and r_2 , $R_d(r_1)$ and $R_d(r_2)$ are the radial functions of 3d electrons.

When calculating the eigenenergies, the appropriate Dq values must be added to diagonal terms of the matrices.

A.1 d^2 configurations

A.1.1 Matrix Elements

		T_2^2	E^2
1A_1	T_2^2	$10B+5C$	$\sqrt{6}(2B+C)$
	E^2		$8B+4C$

3A_2		$-8B$	
		T_2^2	E^2
1E	T_2^2	$B+2C$	$-2\sqrt{3}B$
	E^2		$2C$
1T_1	ET_2	$4B+2C$	
		T_2^2	ET_2
3T_1	T_2^2	$-5B$	$6B$
	ET_2		$4B$
		T_2^2	ET_2
1T_2	T_2^2	$B+2C$	$2\sqrt{3}B$
	ET_2		$2C$
3T_2	ET_2	$-8B$	

A.1.2 Eigenenergies(E/B)

$$\begin{aligned}
 ^1A_1 & \quad (1/2) \{18+9 C/B \pm [100+25 (C/B)^2+400 (Dq/B)^2+100 C/B-80Dq/B-40 (C/B) (Dq/B)]^{1/2}\} \\
 ^3A_2 & \quad -8+10 Dq/B \\
 ^1E & \quad (1/2) \{1+4 C/B \pm [49+400 (Dq/B)^2-40 Dq/B]^{1/2}\} \\
 ^1T_1 & \quad 4+2 C/B \\
 ^3T_1 & \quad (1/2) \{-1-10 Dq/B \pm [225+100 (Dq/B)^2+180 Dq/B]^{1/2}\} \\
 ^1T_2 & \quad (1/2) \{1+4 C/B-10 Dq/B \pm [49+100 (Dq/B)^2-20Dq/B]^{1/2}\} \\
 ^3T_2 & \quad -8
 \end{aligned}$$

A.2 d^3 Configuration

A.2.1 Matrix Elements

		T_2^3	$T_2^2(^3T_1)E$	$T_2^2(^1T_2)E$	$T_2E^2(^1A_1)$	$T_2E^2(^1E)$
2T_2	T_2^3	5C	$-3\sqrt{B}$	$-5\sqrt{B}$	4B+2C	2B
	$T_2^2(^3T_1)E$		$-6B+3C$	3B	$-3\sqrt{3}B$	$-3\sqrt{3}B$
	$T_2^2(^1T_2)E$			4B+3C	$-\sqrt{3}B$	$\sqrt{3}B$
	$T_2E^2(^1A_1)$				6B+5C	10B
	$T_2E^2(^1E)$					$-2B+3C$

		T_2^3	$T_2^2(^3T_1)E$	$T_2^2(^1T_2)E$	$T_2E^2(^3A_2)$	$T_2E^2(^1E)$
2T_1	T_2^3	$-6B+3C$	$-3B$	3B	0	$-2\sqrt{3}B$
	$T_2^2(^3T_1)E$		3C	$-3B$	3B	$3\sqrt{3}B$
	$T_2^2(^1T_2)E$			$-6B+3C$	$-3B$	$-3\sqrt{3}B$
	$T_2E^2(^3A_2)$				$-6B+3C$	$2\sqrt{3}B$
	$T_2E^2(^1E)$					$-2B+3C$

		T_2^3	$T_2^2(^1A_1)E$	$T_2^2(^1E)E$	E^3
2E	T_2^3	$-6B+3C$	$-6\sqrt{2}B$	$-3\sqrt{2}B$	0
	$T_2^2(^1A_1)E$		8B+6C	10B	$\sqrt{3}(2B+3C)$
	$T_2^2(^1E)E$			$-B+3C$	$2\sqrt{3}B$
	E^3				$-8B+4C$

		$T_2^2(^3T_1)E$	$T_2E^2(^3A_2)$
4T_1	$T_2^2(^3T_1)E$	$-3B$	6B
	$T_2E^2(^3A_2)$		$-12B$

4A_2	T_2^3	$-15B$
---------	---------	--------

4T_2	$T_2^2(^3T_1)E$	$-15B$
---------	-----------------	--------

2A_1	$T_2^2(^1E)E$	$-11B+3C$
---------	---------------	-----------

2A_2	$T_2^2(^1E)E$	9B+3C
---------	---------------	-------

A.2.2 Some of Eigenenergies(E/B)

$${}^4A_2 \quad -15-12Dq/B$$

$${}^4T_2 \quad -15-2Dq/B$$

$${}^2A_1 \quad -11+3C/B-2Dq/B$$

$${}^2A_2 \quad 9+3C/B-2Dq/B$$

$${}^4T_1 \quad (1/2)\{-15+6Dq/B \pm [225-180Dq/B+100(Dq/B)^2]^{1/2}\}$$